

# **Colloidal fouling in a microfluidic membrane mimic device**

by

**Nandini Debnath**

A thesis submitted in partial fulfillment of the requirements for the degree of

**Doctor of Philosophy**

Department of Mechanical Engineering

University of Alberta

© Nandini Debnath, 2020

# Abstract

With the advancement in microfabrication technology, on-chip membrane fouling study has undergone significant development and improvement for the last two decades. A single-chip microfluidic filtration platform integrates the benefits of both microfluidics and membrane technology. In this regard, a microfluidic membrane mimic (MMM) device can be used as a micron-sized tool to investigate the fouling phenomena at the pore scale. In this dissertation, fouling experiments were performed in an MMM device to investigate colloidal, organic, and combined fouling using synthetic wastewater such as polystyrene particle solution, polyacrylamide polymer solution, and a mixture of these two solutions, respectively. Four major categories of microscopic fouling were observed: (1) cake layer fouling at upstream, (2) pore fouling (inside the pores), (3) colloidal aggregation (downstream) and (4) colloidal streamer fouling (downstream). We discussed the new kind of downstream fouling and the timescales of colloidal streamer formation. We also showed that the streamer formation is the result of flow of polystyrene and polyacrylamide mixture only. Furthermore, experimental analysis revealed that the colloidal streamer formation is likely the result of flocculation of the PS beads. The flow regimes under which colloidal streamer formation was observed was quantified through state diagrams. Our microfluidic experiments showed that downstream colloidal aggregation and streamer fouling have a significant influence on overall membrane fouling, which were not studied before. Streamer formation has led to the maximum flux decline among all.

We have also performed constant-pressure dead-end filtration by varying particle size with silica ( $\text{SiO}_2$ ). Interestingly,  $\text{SiO}_2$  only resulted in cake layer fouling while PS, which caused cake layer fouling along with downstream colloidal aggregation. Fouling experimental results by varying

ionic concentrations suggested that the energy barrier and secondary energy minimum play an essential role in mitigating membrane fouling. Calculating membrane and foulant interaction energies by extended DLVO (XDLVO) approach showed a growing depth of secondary energy minimum with increasing ionic strength. On the other hand, a decrease in the ionic strength resulted in release of foulants from the secondary energy minimum to the bulk, suggesting an increase in the energy barrier. Additionally, back-washing experiments showed that the majority of the PS particles were released from the cake layer by water channel formation while in case of SiO<sub>2</sub>, the creation of water channel was not prominent. At last, a summary of all significant findings, the potential of microfluidic devices to investigate the microfiltration process at pore scale, and the future trends are provided.

**Keywords:** microfluidics, membrane, membrane mimic, membrane filtration, microfiltration, microfluidic filtration, colloidal fouling, membrane fouling.

# Preface

This dissertation is the original work by Nandini Debnath. The majority of the context in chapter 1 has been published in the following review article:

1. Nandini Debnath and Mohtada Sadrzadeh, “Microfluidic mimic for colloid membrane filtration: a review”, Journal of the Indian Institute of Science, Vol. 98, I. 2, p. 137-157, 2018.

Author contributions: Both authors contributed to the writing of the manuscript.

The majority of the context in chapter 2, 3 and 4 are published in/ready for submission to the following journals:

2. Nandini Debnath, Mahtab Hassanpourfard, Ranajay Ghosh, Japan Trivedi, Thomas Thundat, Mohtada Sadrzadeh & Alope Kumar, “Abiotic streamers in a microfluidic system”, Soft Matter, Vol. 13, I. 46, p. 8698- 8705, 2017.

Author contributions: Nandini Debnath conceived the experiments. Nandini Debnath and Alope Kumar designed the experiments. Mahtab Hassanpourfard fabricated the microchip. Nandini Debnath conducted the experiments and collected the data. Nandini Debnath and Alope Kumar analyzed the experimental results. Thomas Thundat and Mohtada Sadrzadeh played an advisory role. All authors contributed to the writing of the manuscript.

3. Nandini Debnath, Alope Kumar, Thomas Thundat and Mohtada Sadrzadeh, “Investigating fouling at the pore- scale using a microfluidic membrane mimic filtration system”, Scientific Reports, Vol. 9, I. 1, p. 10587, 2019.

Author contributions: Nandini Debnath conceived the experiments. Nandini Debnath, Mohtada Sadrzadeh and Alope Kumar designed the experiments. Nandini Debnath conducted the experiments and collected the data. Nandini Debnath, Mohtada Sadrzadeh and Alope Kumar analyzed the experimental results. Thomas Thundat played an advisory role. All authors contributed to the writing of the manuscript.

4. Nandini Debnath, Alope Kumar, Thomas Thundat and Mohtada Sadrzadeh, “Role of secondary energy minimum in microfluidic membrane fouling”, Journal of Colloids and Interface Science, (Ready for Submission).

Author contributions: Nandini Debnath conceived the experiments. Nandini Debnath, Mohtada Sadrzadeh and Alope Kumar designed the experiments. Nandini Debnath conducted the experiments and collected the data. Nandini Debnath, Mohtada Sadrzadeh and Alope Kumar analyzed the experimental results. Thomas Thundat played an advisory role. All authors contributed to the writing of the manuscript.

*Dedicated to my parents,*

*Bhabatosh Debnath & Minu Debnath*

*And my grandparent,*

*Late Jogomaya Debnath*

*For their unconditional love and inspiring support*

# Acknowledgment

I would like to take this opportunity to express my deepest gratitude and respect to heartily thank my supervisors Dr. Mohtada Sadrzadeh, Dr. Alope Kumar and Dr. Thomas Thundat for their continuous guidance, support, and motivation towards my research. Thanks to the numerous hours spent in discussing not only scientific discoveries but also about life and happenings as great life mentors. Working under them, I got the opportunity to present my research to the international conferences and also learned more about professional documentation and presentation of research. I feel indebted to receive continuous long-distance support and supervision from Dr. Thundat and Dr. Kumar even after living in two different countries (USA and India) towards the end of my PhD program.

I would like to thank all fellows in Kumar Biomicrofluidics Group: Dr. Ishita Biswas, Dr. Tanushree Ghosh, Dr. Mahtab Hassanpourfard, Dr. Swayamdipta Bhaduri and Rajorshi Paul. I am also grateful to Advanced Water Research Lab (AWRL) mates, Dr. Behnam Gheshlaghi, Dr. Hadi Nazaripoor, Dr. Parmiss Mojir Shaibani, Dr. Amirreza Sohrabi, Dr. Muhammad Amirul Islam, Dr. Masoud Rastgar Farajzadeh, MD Farhad Ismail, Nusrat Helali, Amin Karkooti, Ali Mohammadtabar, Simin Shabani, Ayda Razi, Laleh Shmaei, Asad Asad, Pooria Karami, Farshad Mohammadtabar, Debanik Bhattacharjee, Kavya Suresh, Adham Riad, Sadaf Noamani, Hassan Hosseini, Mohammad Amin Soleimanzade, for their valuable comments and suggestions. I would also like to extend my thanks to entire colleagues from Dr. Thudat's group. Thanks to all the group meetings where we get to present in turn which provided insight into my research through a different set of eyes and helped me improve my research significantly.

I would also like to thank the Natural Sciences and Engineering Research Council of Canada (NSERC) for their financial assistance through their graduate student scholarship.

It's my pleasure to thank all the fellow researchers, my friends, my students, my teachers for all the support, love, and blessings which helped me directly or indirectly to continue my studies at the University of Alberta.

I would like to express my gratitude and love towards my family, my parents, my husband, my brothers, and relatives; without them, these accomplishments would not have been possible.

At last but not the least, I would also like to thank my passion for singing and my hobby to listen to good music, which kept me motivated throughout my research, provided the medicine for a healthy and happy mind to accomplish my research.

# Contents

<b><i>Chapter 1 Introduction</i></b> .....	1
<b>1.1 Membrane and microfluidic filtration</b> .....	2
1.1.1 Fundamentals of membrane processes .....	4
1.1.2 Fundamentals of microfluidics.....	5
<b>1.2 Microfluidic membrane mimic (MMM) device</b> .....	7
1.2.1 Production of sieves .....	8
1.2.2 Production of an array of pillars or structures .....	15
1.2.3 Membrane-less filtration.....	16
<b>1.3 Microfluidic colloid filtration</b> .....	18
1.3.1 Fundamentals of colloid filtration.....	19
1.3.2 Microfluidic colloidal fouling.....	23
<b>1.4 Challenges to study membrane fouling in ex-situ experiments</b> .....	31
<b>1.5 Research objectives</b> .....	31
<b>1.6 Thesis structure</b> .....	33
<b>1.7 Author's contribution</b> .....	34

***Chapter 2 Abiotic streamers in a microfluidic system†*** ...36

**2.1 Introduction** .....37

**2.2 Materials and Methods** .....38

**2.3 Results** .....42

**2.4 Discussion** .....49

**2.5 Conclusions** .....53

***Chapter 3 Investigating fouling at the pore-scale using a microfluidic membrane mimic (MMM) filtration system***

**§** .....55

**3.1 Introduction** .....56

**3.2 Materials & Methods** .....58

**3.2 Results & Discussion** .....61

    3.2.1 Microscopic membrane fouling .....61

    3.2.2 Constant-pressure filtration.....66

**3.3 Conclusion** .....80

## ***Chapter 4 Role of secondary energy minimum in***

### ***microfluidic membrane fouling***<sup>^</sup> .....82

#### **4.1 Introduction** .....83

#### **4.2 Background** .....85

#### **4.3 Material and methods** .....88

#### **4.4 Result and discussion** .....92

##### 4.4.1 Determination of free energies.....92

##### 4.4.2 Determination of energy minimum .....95

##### 4.4.3 Microfluidic results .....100

#### **4.5 Conclusion** .....107

## ***Chapter 5 Conclusion & future work***<sup>!</sup> .....109

#### **5.1 Conclusion** .....111

#### **5.2 Strengths and limitations** .....112

#### **5.3 Future work** .....115

#### **5.4 List of contributions** .....116

##### 5.4.1 Journal papers .....116

5.4.2	Conference presentations .....	117
<b>References</b>	.....	<b>118</b>

# List of tables

<b>Table 1. 1:</b> Summary of different approaches for microfluidic membrane mimics on-chip .....	7
<b>Table 1. 2:</b> Categorization of colloidal fouling observed in a microfluidic membrane filtration system.....	23
<b>Table 3. 1:</b> Repeatability data fitted to the exponential decay equation and the corresponding values of the parameters at variable constant pressure difference. The table corresponds to fits shown in Figure 3.7 and 3.10.....	75
<b>Table 4. 1:</b> Surface tension parameters and energy components ( $\text{mJ}/\text{m}^2$ ) of probe liquids at $20^\circ\text{C}$ . Data is taken from van Oss <sup>216</sup> .....	93
<b>Table 4. 2:</b> Surface energy parameters of membranes and colloids.....	93
<b>Table 4. 3:</b> Surface free energy parameters of colloids.....	94

# List of Figures

**Figure 1. 1:** Insertion of membrane on-chip. (a) A schematic of the microfluidic device integrated with a PES membrane sandwiched between PDMS layer and Si substrate<sup>40</sup>. Copyright 2017, reproduced with permission from Elsevier. (b) Schematic of layer sequence starting from bottom to top: Bottom fluidic channel layer, an adhesive layer, filtration membrane layer, PDMS layer, a top fluidic channel layer, hydrophobic degassing membrane layer<sup>38</sup>. Copyright 2016, reproduced with permission from Royal Society of Chemistry. (c) Schematic of a double-filtration microfluidic device isolating extracellular vesicles with a size between 30 and 200nm based on particle size exclusion<sup>41</sup>. Copyright 2017, reproduced with permission from Nature Publishing Group. ....10

**Figure 1. 2:** Sieves made of the permeable membrane. (a) (i) A sectional view and (ii) a side view of the microfluidic device integrated with PDMS microfiltration membrane (PMM) with a regular array of holes of diameter 6.9–10.8  $\mu\text{m}$  capturing >90% of circulating tumor cells from peripheral blood<sup>61</sup>. Copyright 2015, reproduced with permission from Elsevier. (b) (i) Cross-sectional SEM image showing a PMM sandwiched between the top and bottom PDMS layers. (ii) A top view of PMM membrane containing a hexagonal array of holes with a pore diameter of 4 $\mu\text{m}$ , a pore center-to-center distance of 12  $\mu\text{m}$  and a thickness of 10  $\mu\text{m}$ <sup>62</sup>. Copyright 2014, reproduced with permission from Royal Society of Chemistry. (c) (i) Cross-sectional SEM image of a microfluidic membrane chip with the channel and active membrane, (ii) SEM images show the uniformity of pores and (iii) SEM image shows the membrane surface<sup>53</sup>. Copyright 2010, reproduced with permission from Elsevier.....12

**Figure 1. 3:** Sieves made of impermeable membrane. (i) Microfabrication steps for the isopore membrane: (1) deposition of the seed layer (Cr/Cu) on a Si substrate, (2) spin-coating of a thick layer on the Si wafer and UV exposure through a mask, (3) development of the exposed film inside a developer, (4) electroplating of the Ni between photoresist pillars, and (5) releasing the isopore membrane by dissolving the photoresist and seed layer in acetone and Cu etchant, respectively. (ii) SEM image of the circular pore membrane with 3 $\mu$ m diameter and (iii) SEM image of the slotted pore membrane with 3 $\mu$ m slit width <sup>63</sup>. Copyright 2015, reproduced with permission from Springer Berlin Heidelberg. ....14

**Figure 1. 4:** Pillars or structures made of the impermeable membrane. (a) (i) SEM image of a microchannel containing a diagonally aligned single row of pillars (30  $\mu$ m thick pillars) with pillar gap (ii) 12  $\mu$ m for sieving PS particles, and (iii) 7 $\mu$ m for sieving cancer cells from whole blood <sup>65</sup>. Copyright 2016, reproduced with permission from Nature Publishing Group. (b) Schematic representation of the microfluidic channel working in a dead-end mode with dimensions as shown. The inset details the filtration zone with different micro-channel geometries: straight rectangular, straight squared and staggered squared pillars (from left to right) with 10 $\mu$ m gap <sup>67</sup>. Copyright 2014, reproduced with permission from AIP Publishing. (c) A microchannel system fabricated in a basket weave pattern. (i) Schematic of the top and bottom masters resulting in a membrane sandwich. Features in photoresist oriented in the y-direction are marked darker than those in the x-direction. (ii) The optical image (looking down the z-axis) of the PDMS membrane containing 8 $\times$ 8 channel system. The channels are 100 $\mu$ m wide (x- or y-direction), and each of the three levels used in the fabrication is 70  $\mu$ m high (z-direction) but is not enclosed. (iii) SEM image of the basket weave. It was obtained by filling the microchannel with the epoxy prepolymer, curing under ultraviolet light for 10 min, and dissolving the PDMS

casing in tetrabutylammonium fluoride <sup>43</sup>. Copyright 2000, reproduced with permission from American Chemical Society.....17

**Figure 1. 5:** (a) Colloid-surface interaction: a schematic of the representation of a single particle interacting with the membrane surface, and the corresponding critical condition is given for a deposited state. (b) Colloid-colloid interactions: a schematic of the representation of many-body colloid-colloid interactions, and the corresponding critical operating condition is given for a transition from dispersed state to solid state <sup>91</sup>. Copyright 2011, reproduced with permission from Elsevier.....21

**Figure 1. 6:** (a) Microfluidic observation of cake layer formation: microfluidic images showing stable cake layer formation with time for 20 $\mu$ m pillar gap for (i) ultrapure water conditioning and (ii) KCl solution conditioning of PDMS surface <sup>91</sup>. Copyright 2011, reproduced with permission from Elsevier. (b) (i) The build-up of the cake layer during filtration of microgel suspension and (ii) increasing pressure increases crystallinity <sup>90</sup>. Copyright 2016, reproduced with permission from Nature Publishing Group. (c) Effects of ionic strength: fouling rates calculated from the flow stepping experiments at different solution ionic strengths: 0.01mM, 10mM and 100mM of KCl. The inset images are the observations for 10 mM suspensions before and after deposit formation, and (d) Effect of entrance geometry on flow rate and fouling with square entrance (DS10) and tilted funnel entrance (DT10). Filtration results were at constant pressure (200mbar) for low (0.01mM) and high ionic strength (100mM) of KCl demonstrating higher flux decline for DT10. D denotes dead-end flow, S and T denote square and tilted pillars, respectively, and 10 is the channel width <sup>110</sup>. Copyright 2016, reproduced with permission from American Chemical Society.....26

**Figure 1. 7:** (a) Observation of pore fouling for 10mM KCl solution at the downstream of pillars. (b) Demonstration of the link between DLVO theories, the experimental results, and the fouling scenarios. Copyright 2016, reproduced with permission from American Chemical Society.....29

**Figure 1. 8:** (a) Bacterial streamer formation and breaking with time (*P. fluorescens*) under fluorescence imaging with Green filter cube at  $U = 8.92 \times 10^{-4}$  m/s. (i–iv) Show the stretching of one streamer with time, and the final breaking point shows in (iv). The arrow is showing the flow direction <sup>106</sup>. Copyright 2016, reproduced with permission from Nature Publishing Group. ....30

**Figure 2. 1:** Schematic of the preparation of polymer solution at room temperature. 2g of polymer were mixed with 500ml of normal tap water (0.2% w/w PAM solution) and mixed at 600 rpm for at least 3 hours to ensure homogenization. ....39

**Figure 2. 2:** (a) A schematic of the microfluidic device having two inlets and one outlet. The blow-out section shows the entry Y-channel where mixing process occurs. Polymer solution (PAM) and polystyrene solution (PS) were injected with a constant volume flow rate  $Q_{PAM}$  and  $Q_{PS}$ . Total width of the channel is  $w$ . (b) SEM image of the microchannel clearly shows the uniformity of micropillars. (c) Top-view of the microfluidic device. The diameter ( $d$ ) and out of plane height ( $h$ ) of the pillars both are  $50\mu\text{m}$  and width ( $w$ ) of the device is  $625\mu\text{m}$ . The distance between the center of the pillars ( $s$ ) and two rows of the consecutive pillars ( $s$ ) is  $75\mu\text{m}$ . (d) A schematic of the total experimental set up. PAM (green) and PS (pink) solutions were transported through two inlets of the microfluidic device with a dual syringe pump which generates a constant volume flow rate  $Q_{PAM}$  and  $Q_{PS}$ . ....41

**Figure 2. 3:** Complex moduli for PAM (0.2%) as a function of angular frequency at low shear. Relaxation time ( $\lambda$ ) for PAM (0.2%) solution is  $\sim 13$ s. ....43

**Figure 2. 4:** Streamer formation imaged using the Texas Red filter cube. ((a)-(e)) Time-lapse imaging of the streamer formation and maturation at for flow rate  $Q_{PAM}=10\mu\text{L/h}$  and  $Q_{PS}=40\mu\text{L/h}$ . (f) SEM imaging of streamer remnant in the microfluidic device.....44

**Figure 2. 5:** (a) Two-color confocal imaging of a streamer after 1 hour of experimentation. White-dashed line indicates the  $y$ -location at which the corresponding  $z$ - $x$  plane is depicted. Image of the same location using (b) FITC Green filter cube and (c) Texas Red filter cube. ....46

**Figure 2. 6:** Control experiments for the investigation of streamer formation confirms that streamer forms for the combined flow of PAM (0.2% w/w) and PS (0.8%w/w) solution only. ..47

**Figure 2. 7:** (a) Formation state diagram of streamer formation over different flow rates  $Q_{PAM}$ ,  $Q_{PS}$  and concentration  $C_{PAM}$ ,  $C_{PS}$ . Red triangle represents true streamer formation and blue circle indicates no streamer formation. The side-bars depict the optical microscope observations at the three located delineated in the formation plot: (i) Streamer formation after one hour for  $C_{PAM}\times Q_{PAM}=2\mu\text{L/h}$ ,  $C_{PS}\times Q_{PS}=3\mu\text{L/h}$ ; (ii) Streamer formation at phase boundary for  $C_{PAM}\times Q_{PAM}=3\mu\text{L/h}$ ,  $C_{PS}\times Q_{PS}=2\mu\text{L/h}$ ; (iii) No streamer formation after one hour for  $C_{PAM}\times Q_{PAM}=3\mu\text{L/h}$ ,  $C_{PS}\times Q_{PS}=1.5\mu\text{L/h}$ . (b) State diagram of streamer formation at various pH values and ratios of  $(C_{PS}Q_{PS})/(C_{PAM}Q_{PAM})$ .....48

**Figure 2. 8:** Repeat experiments for the phase diagram of streamer formation by varying flow rates when the concentration is fixed for  $Q_{PAM}$  and  $Q_{PS}$ . Red triangle represents true streamer formation and blue circle indicates no streamer formation. Each number represents repeatability.

(a) Streamer formation after 1h for  $Q_{PAM}=10\mu\text{L/h}$ ,  $Q_{PS}=30\mu\text{L/h}$ . (b) Transition phase for  $Q_{PAM}=Q_{PS}=30\mu\text{L/h}$ . (c) No streamer formation after 1h for  $Q_{PAM}=30\mu\text{L/h}$ ,  $Q_{PS}=25\mu\text{L/h}$ . (d) Streamer formation (different morphology) after 1h for  $Q_{PAM}=5\mu\text{L/h}$ ,  $Q_{PS}=20\mu\text{L/h}$ . (e) Transition phase for  $Q_{PAM}=Q_{PS}=15\mu\text{L/h}$ . (f) No streamer formation after 1h for  $Q_{PAM}=30\mu\text{L/h}$ ,  $Q_{PS}=5\mu\text{L/h}$ .  
 .....49

**Figure 2. 9:** Time lapse imaging of a bacterial floc attaching to a pillar wall and undergoing a large elastic deformation by fluidic loading to form a bacterial streamer. Figure is adapted from Hassanpourfard et al.<sup>22</sup>. .....50

**Figure 2. 10:** (a) SEM image of a floc formed under quiescent conditions. The SEM imaging was done for a volume ratio (PAM:PS) of 1:4 at pH 5. (b) Normalized frequency histogram of the equivalent diameter ( $d_e$ ) of flocs. For a volume ratio (PAM: PS) of 1:4 the mean is approximately 16  $\mu\text{m}$  (of 61 data points) and for a volume ratio of 1:1, the mean is approximately 7  $\mu\text{m}$  (of 47 data points). The inset shows the optical microscope image of flocs. (c) The average equivalent diameter of flocs ( $\langle d_e \rangle$ ) as a function of pH for two different mixing ratios of PAM and PS solutions. (d) Zeta potential as a function of pH for PS bead solutions (0.2% w/w). .....51

**Figure 3. 1:** (a) A schematic of the experimental setup. A pressure controller and flow-board unit controls the pressure and the flow rate of the membrane mimic microfluidic device, respectively. The pressure difference causes the feed to enter one inlet of the device via the flow unit and the waste is collected from the outlet/permeates side. (b) SEM image of the microfluidic membrane mimic device with dimensions (membrane thickness,  $t=102\mu\text{m}$  and membrane width  $w = 504\mu\text{m}$ ). The blown-out sections show a gap,  $p = 2\mu\text{m}$ , between any two pillars with

diameter  $d = 50\mu\text{m}$  (top view mode) and a height of  $h = 5\mu\text{m}$  (side view mode). (c) Control experiments with ultrapure water shows almost constant flux at various pressures for the microfluidic membrane mimic device.....59

**Figure 3. 2:** Pure water flux as a function of pressure. ....62

**Figure 3. 3:** Constant pressure repeatability experiments for water at different pressure.....63

**Figure 3. 4:** Microscopic colloidal fouling phenomena at different locations with their corresponding schematics. (a) cake filtration for PS 0.2% at 345mbar at upstream, (b) pore blocking for PAM 0.2% at 345 mbar at the pillar pores, (c) colloidal aggregation for PS 0.2% at 689mbar and (d) colloidal streamer formation for the combined fouling (PAM (0.2%):PS(0.2%)=1:4) at 689mbar at downstream. All images are taken at 120 min of filtration and the scale bars are  $50\mu\text{m}$ . Schematics are not to scale. ....64

**Figure 3. 5:** (a) Filtration experiments at constant pressure shows decreasing flux for PS 0.2% as fouling progresses with filtration time. (b) Corresponding microfluidic images show end-result of fouling (120 min). At low pressures, fouling is more like cake filtration at upstream (i)-(ii). At higher pressures more colloidal aggregation are observed at downstream with simultaneous pore blocking and cake filtration (iii)-(iv). (c) Schematic of fouling at low pressure ( $<345\text{mbar}$ ) and high pressure ( $>345\text{mbar}$ ) showing the fouling evolution in 60 min.....67

**Figure 3. 6:** Constant pressure experiments at 1378 mbar pressure for the PS 0.2% solution show sharp decline in flux compared to lower pressure. (i) Microfluidic fouling started with colloidal aggregation at downstream. (ii)-(iii) Downstream colloidal aggregation fouling continued with

partial pore fouling and filter cake till 40 min of filtration. (iv) A significant increase in cake layer thickness is observed till 120min of filtration.....69

**Figure 3. 7:** Repeatability experiments at different constant pressure with PS 0.2% solution. The repeatability curves are fitted to the same exponential decay equation shown in table 3.1.....70

**Figure 3. 8:** Constant pressure fouling scenarios of PS at 689mbar pressure for different concentrations (i) PS 0.02% (ii) PS 0.4% and (iii) PS 1% after 60 min of filtration.....72

**Figure 3. 9:** Comparison of the constant-pressure fouling behaviour for three types of foulants at the same pressure (689 mbar). (a) Flux vs. time plot showing more severe flux decline for the case of combined fouling (PAM (0.2%):PS (0.2%) =1:4) than individual organic and colloidal fouling (PAM 0.2% & PS 0.2%), (b) corresponding microfluidic images at the end of the filtration process showing (i) Colloidal aggregation at downstream with partial pore blocking and cake filtration for PS filtration, (ii) pore blocking for PAM filtration, and (iii) streamer formation at downstream for the case of combined fouling.....74

**Figure 3. 10:** Repeatability experiments at constant pressure (689 mbar) for (a) PAM 0.2% solution and (b) downstream colloidal streamer formation with PAM (0.2%):PS (0.2%)=1:4, combined solution filtration.....74

**Figure 3. 11:** (a) Water channel formation observed by Lohaus et al. in numerical simulation for the square connected (i) and staggered (ii) arrangement of pillars<sup>200</sup>. Scale bars are 50µm. (Copyright 2018, reproduced with permission from Journal of Membrane Science). Water channel formation for (b) colloidal aggregation (PS 0.2%) at 1378mbar pressure and (c) colloidal streamer (PAM (0.2%):PS (0.2%) =1:4) at 689mbar pressure after 180 min of filtration. Primary

water channels (marked with white dash line) and secondary water channels are shown with arrows. Scale bars are 50 $\mu$ m.....76

**Figure 3. 12:** Flux vs time plot for the three foulants using Hermia model at constant pressure (689mbar). Curves are fitted using regression analysis where  $R^2$  value represents regression coefficient. The flux trends are compared to Hermia’s model for (a) cake filtration, (b) standard pore blocking, (c) intermediate pore blocking, (d) complete pore blocking. From the regression analysis, the maximum value of  $R^2$  indicates that the fouling is complete pore blocking for the three foulants. ....78

**Figure 3. 13:** Fouling percentage evaluation for colloidal aggregation and streamer fouling at the same pressure 689 mbar. At first, the dead-end filtration is performed for the clean system with pure water for 30 min, next the fouling experiments are performed for another 30 min. After that, a hydraulic cleaning is performed to clean the chip for another 30 min at higher pressure. Then, pure water filtration is performed again for 30 min. Figure (a) and (b) show the corresponding flux for PS 0.2% and PAM(0.2%):PS(0.2%)=1:4, respectively. (c) Represents the corresponding fouling percentage contributions for the same. Reversible flux decline ratio ( $DR_r$ ) is decreased by ~24% than irreversible flux decline ratio ( $DR_{ir}$ ) for colloidal aggregation and irreversible flux decline ratio ( $DR_{ir}$ ) is increased by ~72% than reversible flux decline ratio ( $DR_r$ ) for streamer fouling. ....80

**Figure 4. 1:** (a) PDMS microfluidic chip bonded to cover glass with inlet for feed and outlet for permeate. SEM image shows the top view and side view of the microchip with dimensions (b) Zeta potential as a function of mM of NaCl for PDMS, SiO<sub>2</sub> (0.2% w/w) & PS (0.2% w/w) surfaces at room temperature.....89

**Figure 4. 2:** SEM images of the coated PDMS surfaces with deposited foulants. Deposition of foulants on PDMS surface is increased with molar strength.....90

**Figure 4. 3:** Contact angle of diiodomethane, formamide and water with increasing NaCl molar concentrations for (a) PDMS, (b) PS-PDMS and (c) SiO<sub>2</sub>-PDMS.....91

**Figure 4. 4:** Cohesion energy ( $\Delta G_{123Coh}$ ) for SiO<sub>2</sub>-SiO<sub>2</sub> and PS-PS and adhesion energy ( $\Delta G_{123Adh}$ ) for SiO<sub>2</sub>-PDMS and PS-PDMS as a function of NaCl molar concentrations. ....95

**Figure 4. 5:** DLVO and XDLVO interaction energy profile for foulant-membrane (a) PS-PDMS, (b) SiO<sub>2</sub>-PDMS and foulant-foulant (c) PS-PS, (d) SiO<sub>2</sub>-SiO<sub>2</sub> interactions at 100mM NaCl. The enlarge version shows the existence of the secondary energy minimum for (c) and (d). ....97

**Figure 4. 6:** XDLVO interaction energy profile for (a) PS-PDMS, (b) SiO<sub>2</sub>-PDMS, (c) PS-PS and (d) SiO<sub>2</sub>-SiO<sub>2</sub> with varying molar concentrations as a function of separation distance. ....98

**Figure 4. 7:** Secondary energy minimum depth for (a) PS-PS interactions were twice the depth of secondary energy minimum for (b) SiO<sub>2</sub>-SiO<sub>2</sub> for 50mM, 100Mm and 200mM NaCl molar concentrations. ....99

**Figure 4. 8:** Flux vs time plot for microfluidic constant pressure filtration (689mbar) showing severe flux decline with increasing molar concentrations for SiO<sub>2</sub> 0.2% w/w foulant compared to PS 0.2% w/w foulant..... 100

**Figure 4. 9:** Constant pressure repeatability experiments for 1mM (a) and (d), 50mM (b) and (e) and 100mM (c) and (f) of NaCl at 689mbar pressure..... 101

**Figure 4. 10:** Microfluidic fouling images showed cake layer fouling for SiO<sub>2</sub> and cake layer with downstream fouling for PS for different ionic concentrations of NaCl (a) 1mM, (b) 50mM, (c) 100mM at 689mbar pressure. All scale bars are 50μm. .... 102

**Figure 4. 11:** Microfluidic back-flashing experiments for PS and SiO<sub>2</sub> fouling in MMM device showed (a) particle release by water channel formation from cake layer for PS at 689mbar and (b) cake layer release by water film formation around pillar surface for SiO<sub>2</sub> at >689mbar pressure..... 104

**Figure 4. 12:** Microfluidic back-flashing results at 689mbar pressure for PS before back-flashing (a)(i),(b)(i),(c)(i) and after back-flashing (a)(ii),(b)(ii),(c)(ii) showed particle release from secondary energy minimum..... 105

**Figure 4. 13:** Microfluidic back-flashing results at 689mbar pressure for SiO<sub>2</sub> showed very few particle release from the outer surface of the cake layer at (a) 1mM NaCl (b) 50mM NaCl and (c) 100mM NaCl. .... 106

# Chapter 1

## Introduction\*

---

\*The materials of this chapter is published in “N. Debnath and M. Sadrzadeh, “Microfluidic mimic for colloid membrane filtration: a review”, Journal of the Indian Institute of Science, Vol. 98, I. 2, p. 137-157, 2018.”

## **1.1 Membrane and microfluidic filtration**

Water is one of the most important substances in our life. The majority of the available water today is either salty or polluted which is a growing global issue. The major sources of water contaminants can be industrial waste, pharmaceuticals, residential waste and fertilizers which are reducing the water quality day by day and rendering toxicity to human and to the environment. A globally sustainable supply of clean, freshwater is necessary to human life and food supply, industrial processes, and energy production <sup>1</sup>. Traditional clean water sources are limited, and their pollution due to the rapid urbanization and industrialization calls for a more effective, lower-cost, robust water treatment processes <sup>2</sup>.

Filtration systems play a remarkable role in maintaining water quality. Among all filtration processes, membrane filtration is a breakthrough technology widely used in wastewater treatment. Membrane separation processes have become one of the fastest emerging technologies for water treatment due to their distinct advantages over traditional methods, primarily lower operating costs, compact design, and high product quality <sup>3</sup>. Advanced membranes provide a potential solution for water and energy sustainability <sup>4,5</sup>. The main advantage of membranes is that they can be used for recovery and purification of a huge variety of materials across broad range industries <sup>6,7</sup>. There are various types of pressure-driven liquid-based membrane processes applicable for water treatment including microfiltration (MF), ultrafiltration (UF), nanofiltration (NF), and reverse osmosis (RO). They can be categorized by their pore sizes: MF is the most porous and RO is the densest one. NF and RO membrane are used for water desalination and softening while MF and UF are mainly utilized for removing suspended solids, colloids, pathogens, emulsions from contaminated water sources <sup>7</sup>.

A major challenge for the sustainable use of membrane filtration processes is fouling of membranes by the attachment of water contaminants (colloidal particles, organic matter, and biomaterials) onto their surfaces. Fouling has several negative impacts on filtration such as reducing water flux and salt rejection, increasing the cleaning demand, and decreasing the life cycle of membranes and subsequently increasing the operating cost of the water treatment process. The reduction of membrane performance due to the adsorption of colloidal particles on the surface or within the membrane pores is the most common challenge in MF/UF processes<sup>8,9</sup>. Colloidal particles reduce the membrane performance by the development of a concentration polarization layer and formation of a cake fouling layer on the membrane surface<sup>10</sup>. To analyze the transport phenomena inside the pores and the mechanism of colloidal fouling, a membrane module is typically considered as an opaque system, where only the input and the output can be measured and analyzed. To overcome these challenges microfluidic devices can be utilized to visualize and understand the fluid flow at pore scale and investigate the nature, properties, and evolution of colloidal fouling.

A microfluidic chip is a pattern of the engraved microchannel through which fluids are directed, mixed and separated. Advancement in the microfabrication technology has enabled the development of microfluidics for diverse applications like lab-on-a-chip<sup>11, 12</sup>, nanoparticle separation<sup>13-15</sup>, chemical sensors<sup>16, 17</sup>, detection of pathogens<sup>17</sup>, electrophoresis<sup>18, 19</sup>, micro-nozzles<sup>20</sup>, microvalves<sup>21, 22</sup>, and DNA analysis<sup>23,24</sup>. A microfluidic filtration system can provide a legitimate strategy to simulate the fluid flow in conventional membrane filtration processes<sup>25, 26</sup>. Microfluidic chips can be designed to mimic the pore sizes of various membranes (0.1-10 $\mu$ m for MF) filtration operating modes (dead-end or cross-flow). A microfluidic system where inertia ( $Re \ll 1$  or Stokes number  $\ll 1$ ) and Brownian motion are negligible, can be reasonable to

simulate an MF process <sup>27</sup>. For microfluidic membranes, transport is mostly governed by membrane pore size and is not an intrinsic material property, although interaction with the internal membrane surface can play a crucial role. The primary advantage of a microfluidic filtration system is the real-time observation of transport phenomena and the evolution of the fouling inside the system through microscopy. Connecting the membrane to a microfluidic chip also allows for the optimization of separation process and mitigation of fouling at the pore scale. However, there are critical gaps between traditional filtration systems and microfluidic filtration systems. As modern technology evolves, these gaps can be bridged with microfluidic membrane mimic systems.

In the next section, first, the theoretical basis of membranes and microfluidics is presented. Next, the fabrication methods for microfluidic membrane mimics are discussed. Then, the literature of microfluidic colloid filtration in microfluidic membrane mimic filtration systems is presented. Finally, the challenges and limitations of microfluidic membranes mimic for colloid filtration are discussed.

### **1.1.1 Fundamentals of membrane processes**

A membrane is a semi-permeable barrier that allows the selective removal of particles, molecules, or ions from a solution <sup>7</sup>. The transport of molecules through the membrane occurs due to the chemical potential difference between the two phases. In general, the membrane performance is characterized by permeate flux and salt rejection. In a pressure-driven porous membrane, the permeate flux ( $J$ ) is governed by the pore flow model and is typically expressed by the Hagen-Poiseuille equation as follows,

$$J = \frac{\epsilon r^2}{8\mu\tau} \frac{\Delta P}{\Delta t} \tag{1.1}$$

where  $J$  is the flux per unit area,  $\Delta P$  is the pressure difference and  $\Delta t$  is the membrane thickness,  $\varepsilon$  is the porosity,  $\tau$  is the tortuosity,  $\mu$  is the viscosity, and  $r$  is the radius of a pore. For a dense membrane, however, the transport phenomenon is governed by the solution-diffusion mechanism and is an intrinsic property of the membrane material. The relationship between the diffusion coefficient,  $D$ , the permeability,  $P$ , and solubility coefficient,  $S$ , can be given by

$$P = D.S \quad (1.2)$$

In a porous membrane, the transport is controlled by the membrane morphology, not the intrinsic material property. Membrane morphology is characterized by the porosity ( $\varepsilon$ ) and tortuosity ( $\tau$ ). The porosity ( $\varepsilon$ ) is a measure of the fraction of the empty spaces to the total volume, or surface, which ranges  $<0.02$  for nanometer-sized pore and  $>0.82$  for micrometer-sized pores (considering pore size range from 1nm to 10 $\mu$ m). The tortuosity ( $\tau$ ) is a measure of the average path length through a pore across the thickness of the membrane. Retention,  $R$ , is defined as an alternative to selectivity. Retention ranges from 0%, indicating no contaminant rejection by the membrane, to 100%, indicating complete restriction to pass through membrane pores. Retention depends on the ratio of contaminant size to pore size and is expressed as,

$$R = 1 - \frac{c_p}{c_f} \quad (1.3)$$

where,  $c_p$  and  $c_f$  are the concentrations of contaminants in the permeate and feed, respectively. A combination of water recovery (permeability  $P$ ) and water quality (retention) provides an idea of a membrane separation performance.

### 1.1.2 Fundamentals of microfluidics

Microfluidics refers to the precise control, manipulation, and multiplexing of fluid at the micron scale in at least one dimension. With this miniaturization, microfluidics enables analyzing fluid flow for conventional laboratory processes on a single chip. The main advantage of microfluidics is the increased ratio of surface-to-volume with improved performance, including rapid sample processing, high integrity, low reagent consumption, and precise fluid control.

However, the microfluidic devices suffer from several limitations<sup>28, 29</sup>. It is important to note that these devices are sensitive to surface physical and chemical properties<sup>12, 29</sup>. At the micro-level, the microfluidic fluid behavior can be affected by several factors such as surface tension, laminar flow effect, capillary, energy dissipation, and fluidic resistance<sup>12, 30</sup>. More about fabrication techniques of microfluidic devices can be found in several reviews<sup>11, 14, 31, 32</sup>. The common materials used for the fabrication of microfluidics are silicon, silica, metal, glass, polymer (PDMS) and paper<sup>33</sup>.

Modeling fluid flow in microfluidics is generally performed using continuum theory<sup>34</sup>. This is because the smallest feature size that can be patterned using microfabrication is limited by the diffraction of light to 0.5 $\mu\text{m}$  for contact photolithography<sup>35</sup>, which is much larger than the mean free path of molecules. Hence, for an incompressible Newtonian fluid, the flow is defined by the Navier-Stokes and continuity equations as follows,

$$\rho \frac{\partial u}{\partial t} + \rho(u \cdot \nabla)u = f_b - \nabla P + \mu \nabla^2 u \quad (1.4)$$

$$\nabla \cdot u = 0 \quad (1.5)$$

where  $u$  is the velocity vector,  $\rho$  is the density of the fluid,  $P$  is the pressure,  $t$  is time,  $\mu$  is dynamic viscosity, and  $f_b$  is the body force. Here, the inertial acceleration term appears on the

left and forces are on the right. For a concentration distribution, the convection-diffusion equation is applied as follows,

$$\frac{\partial c}{\partial t} + (u \cdot \nabla)c = D \nabla^2 c \quad (1.6)$$

where  $c$  is the concentration, and  $D$  is the diffusion coefficient. In a microfluidic device, often the magnitude of inertial and viscous forces are compared with non-dimensional Reynolds number ( $Re = \rho ul / \mu$ , where  $l$  is the characteristic length). Another non-dimensional number, the Peclet number ( $Pe = lu / D$ ), is used to determine the ratio of convective and diffusive transport.

## 1.2 Microfluidic membrane mimic (MMM) device

In this section, a particular focus is placed on the methodology to bridge membrane technology and microfluidics. Different fabrication techniques, e.g., photolithography, soft lithography, hot embossing, micromachining, wet etching, dry etching, deep reactive ion etching (DRIE), injection molding, and E-beam lithography have been used so far. A broader discussion about the fabrication of microfluidic membrane devices can be found in several reviews<sup>25–27</sup>. These methods can be divided into three major categories: (1) production of sieves; (2) production of an array of pillars or structures; and (3) membrane-less filtration. Table 1.1 summarises some of the different approaches within these three categories.

**Table 1. 1:** Summary of different approaches for microfluidic membrane mimics on-chip

Methods	Approaches	Filtration mode	Materials
Production of sieves	Insertion of membrane/sieve on chip-sandwiched method <sup>36–41</sup>	Dead-end & cross flow filtration	PDMS chip <sup>14, 15, 42–45</sup>
	Direct casting of sieves made of permeable membrane <sup>53, 61, 62</sup>		Other polymeric chip <sup>38, 46–50</sup>
			Hydrogel based chip

	Direct casting of sieves made of impermeable membrane <sup>50, 63, 64</sup>		<sup>51, 52</sup> Silicon and silica <sup>53-55</sup> Zeolite <sup>10, 56, 57</sup> , Alumina <sup>58, 59</sup> , paper <sup>60</sup> etc.
<b>Production of an array of pillars or structures</b>	Pillars or structures made of impermeable membrane materials <sup>22, 42, 43, 65-68</sup>	Dead-end filtration	PDMS chip <sup>42, 43, 65-68</sup> Teflon chip <sup>22</sup>
<b>Membrane-less filtration</b>	Inertial transport and solute gradient <sup>69, 70</sup>	Dead-end & Cross flow filtration	PDMS chip <sup>70-72</sup>
	Liquid membrane formation <sup>73-75</sup>		PDMS chip <sup>74</sup> Glass <sup>73, 76, 77</sup>
	Lipid membrane formation <sup>78-81</sup>		PDMS chip <sup>79, 80, 82</sup> Other polymeric chip <sup>81, 83</sup> Mica and SiO <sub>2</sub> <sup>78</sup> Si <sub>3</sub> N <sub>4</sub> <sup>84</sup>

### 1.2.1 Production of sieves

To produce sieves, the first, simple, easy and sophisticated way of fabricating microfluidic membrane mimic devices is to insert a membrane with the required pore size on to a chip. Second approach is the direct casting of sieves made of a permeable membrane where transverse and lateral filtrations take place as the particle can pass through the membrane pores and fabricated sieves. The third approach is the direct casting of sieves made of an impermeable membrane where transverse filtration takes place as the particles can pass through sieves only. For these three kinds, different materials, such as PDMS <sup>14, 15, 42-45</sup> and other polymeric materials <sup>38, 46-50</sup>, hydrogel <sup>51, 52</sup>, paper <sup>60</sup>, Si <sup>53-55</sup>, zeolite <sup>56, 57, 85</sup>, and alumina <sup>58, 59</sup>, can be used. In a pressure-driven membrane filtration device, the dead-end or cross-flow MF membrane can be

fabricated with various sieve sizes (0.1 $\mu$ m-10 $\mu$ m) through which the feed solution can pass while components larger than the sieve size are retained. It is important to note that, to explore membrane properties, only the membrane mimic pore size area can be treated as a membrane surface area (excluding microfluidic channel). The fabricated microfluidic membrane filtration devices by sieve method have been broadly used for biological and medical applications<sup>36, 46, 86–88</sup>, fouling investigations<sup>37, 63, 67, 89–91</sup>, chemical reagent detection<sup>92</sup>, sample pre-treatment<sup>47</sup>, oil-water separation<sup>93, 94</sup>, removal of macromolecules and aggregates<sup>13, 15, 65, 66, 95</sup>, removal of solutes such as protein<sup>63, 96</sup>, micro-reactor research<sup>56, 97</sup>, DNA separation<sup>59, 63, 98</sup>, controlled drug delivery<sup>50, 59, 88</sup>, and pervaporation and gas separation<sup>39, 42, 44, 99</sup>.

### ***Insertion of membrane/sieve on-chip***

The most straightforward method of creating an effective and low-cost microfluidic membrane mimic is to integrate a membrane on-chip to a traditional membrane by clamping or gluing<sup>25</sup>. In the most common approach, an initial pattern is defined on a Si/glass wafer by lithography. After that, wet etching (using KOH or tetra-methyl-ammonium hydroxide solution) or dry etching (using RIE or DRIE) is performed following a proper recipe to etch the small features and micro-channels. Lastly, a micro-patterned layer is bonded to a flat surface (glass) by using either an adhesive or a plasma bonding method to complete the microfluidic membrane assembly. This is best known as the sandwiched method. The assembled device allows having a “top view” of the pores for microscopic visualization. Di et al.<sup>40</sup> studied a microfluidic system for particle deposition during UF of KCl solutions containing 0.4 $\mu$ m (mean diameter) latex suspensions. Direct visualization of the deposition of particles onto the membrane surface was possible when they sandwiched PES membrane between a PDMS layer and a Si substrate (Figure 1.1(a)).

Cheng et al.<sup>38</sup> innovated a multilayer-filtration method by incorporating Cyclopore polycarbonate (PC) membranes (with a pore size of 3  $\mu\text{m}$ ) on an adhesive layer, which was fixed on a bottom fluidic channel layer made of polymethyl methacrylate (PMMA). Next, a 120 $\mu\text{m}$  thick PDMS layer and porous polytetrafluoroethylene (PTFE) membranes (with a pore size of 0.2  $\mu\text{m}$ ) were assembled with top fluidic channels in a sequence, as shown in Figure 1.1(b).

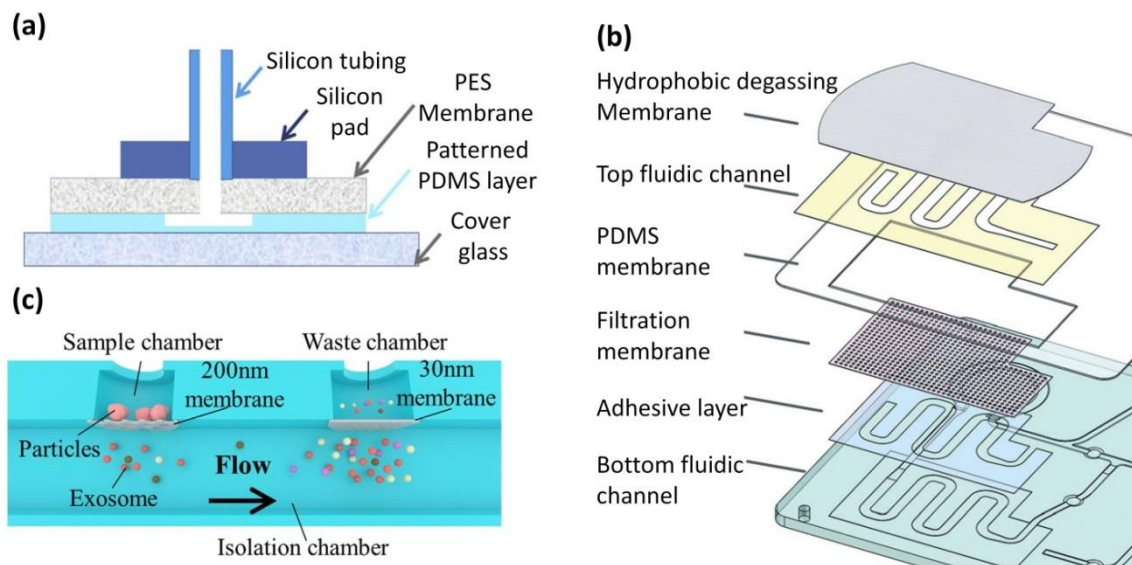


**Figure 1. 1** Insertion of membrane on-chip. (a) A schematic of the microfluidic device integrated with a PES membrane sandwiched between PDMS layer and Si substrate<sup>40</sup>. Copyright 2017, reproduced with permission from Elsevier. (b) Schematic of layer sequence starting from bottom to top: Bottom fluidic channel layer, an adhesive layer, filtration membrane layer, PDMS layer, a top fluidic channel layer, hydrophobic degassing membrane layer<sup>38</sup>. Copyright 2016, reproduced with permission from Royal Society of Chemistry. (c) Schematic of a double-filtration microfluidic device isolating extracellular vesicles with a size between 30 and 200nm based on particle size exclusion<sup>41</sup>. Copyright 2017, reproduced with permission from Nature Publishing Group.

Liang et al.<sup>41</sup> developed an integrated double-filtration microfluidic device for the separation, enrichment, and quantification of urinary extracellular vesicles for the detection of bladder cancer. The primary and secondary filtration processes consisted of 200nm and 30nm pore size

membranes integrated along the cross-section of a microfluidic channel (Figure 1.1(c)). Insertion of porous membrane on-chip was not only limited to liquid flow but also used for pervaporation and gas separation <sup>39</sup>.

### ***Direct casting of sieves made of a permeable membrane***

Another common approach for the production of sieves is to directly fabricate sieves inside a microchip. Fan et al. <sup>61</sup> reported a novel PDMS membrane filtration mimic (holes with diameter 6.9-10.8 $\mu$ m) for fast and effective separation of circulating tumor cells from peripheral blood. As can be seen in Figure 1.2(a), the PDMS membrane is inserted between the top and bottom chambers with a sacrificial transferring film on top chamber by using a sandwich molding method. They achieved >90% recovery when separating lung cancer cells from peripheral blood. In another device, Li et al. <sup>62</sup> sandwiched a surface-micromachined PDMS MF membrane with high porosity between a top and a bottom PDMS layers (Figure 1.2(b)) and reported an enhanced permeation performance for the separation of white blood cells (WBCs) from whole blood. With a sample throughput of 1 mL/h, this cross-flow microfluidic filtration assembly recovered  $27.4 \pm 4.9\%$  of WBCs with a purity of  $93.5 \pm 0.5\%$ . Ngene et al. <sup>53</sup> observed a local deposition of a cake layer during filtration of polystyrene particles (6 $\mu$ m) and described a new method for non-invasive in-situ fouling characterization. To prepare the embedded channel membrane, first, square silica capillaries were glued to a glass plate with double-sided tape. Next, a solution of PEI/PVP/NMP (19/11/70, w/w/w) was cast on a glass plate at room temperature and phase separation technique was used to release the membrane from the glass plate. Next, the membrane was left in the water bath and sodium oxochlorate (4000 ppm) to completely remove solvent. When the structured membrane was ready, they fused silica capillary in the channels and the

membrane with capillary was placed in between lamination sheet for sealing. SEM image of the embedded membrane channel is shown in figure 1.2 (c).

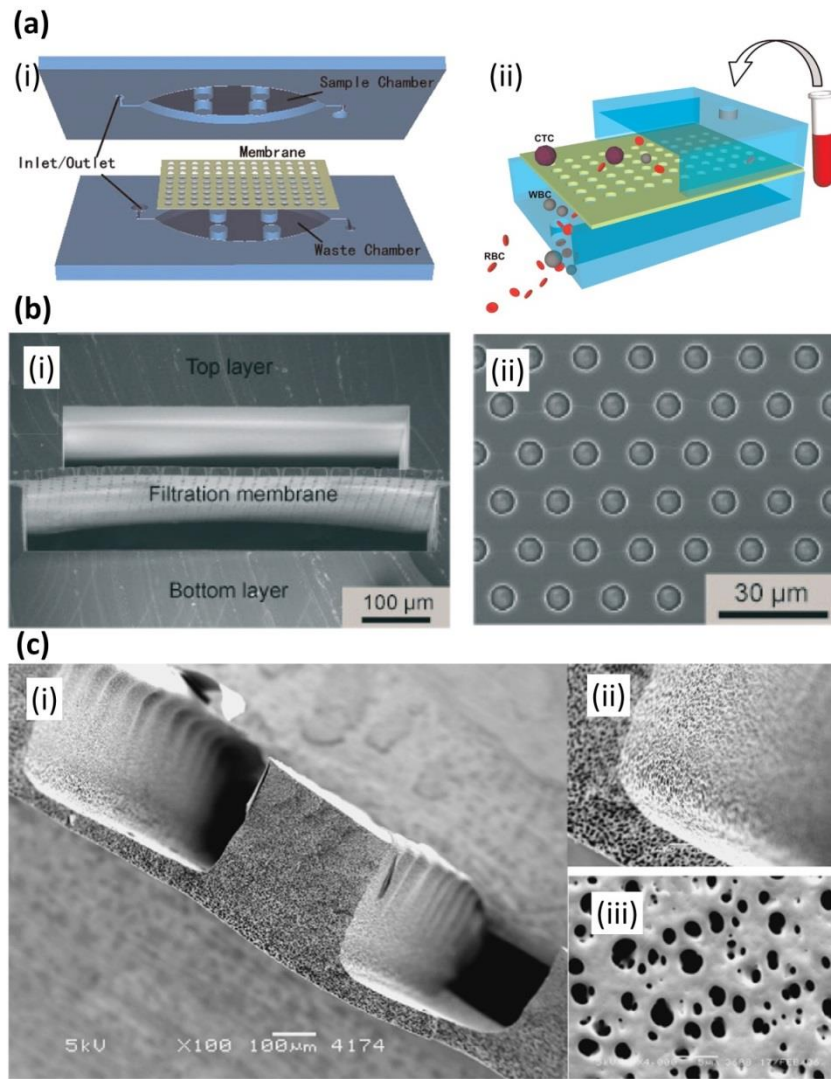


**Figure 1. 2:** Sieves made of the permeable membrane. (a) (i) A sectional view and (ii) a side view of the microfluidic device integrated with PDMS microfiltration membrane (PMM) with a regular array of holes of diameter 6.9–10.8  $\mu\text{m}$  capturing >90% of circulating tumor cells from peripheral blood <sup>61</sup>. Copyright 2015, reproduced with permission from Elsevier. (b) (i) Cross-sectional SEM image showing a PMM sandwiched between the top and bottom PDMS layers. (ii) A top view of PMM membrane containing a hexagonal array of holes with a pore diameter of 4 $\mu\text{m}$ , a pore center-to-center distance of 12  $\mu\text{m}$  and a thickness of 10  $\mu\text{m}$  <sup>62</sup>. Copyright 2014, reproduced with permission from Royal Society of Chemistry. (c) (i) Cross-sectional SEM image of a microfluidic

membrane chip with the channel and active membrane, (ii) SEM images show the uniformity of pores and (iii) SEM image shows the membrane surface <sup>53</sup>. Copyright 2010, reproduced with permission from Elsevier.

Leichle et al. <sup>55</sup> discussed a fabrication method to incorporate a Si membrane inside a microchannel and demonstrated a dead-end MF at micron-scale by retaining 300nm diameter polymer microspheres. de Jong et al. <sup>100</sup> reported Phase Separation Micro Molding method to generate thin polymeric microfluidic devices with tunable porosity. The tunable porosity of the chip materials was achieved using micro-molding phase separation technique offering a specific transport system for gasses, liquids, and solutes.

#### ***Direct casting of sieves made of impermeable membrane***

Chen et al. <sup>64</sup> described a novel fabrication technique to generate a wide range of pore sizes in PDMS MF membranes. They created sieves (4 $\mu$ m diameter) by photolithography micromachining with PDMS material, where particles passed through the sieves only. Also, they added more layers with plasma bonding between PDMS-PDMS layers. Warkiani et al. <sup>63</sup>, fabricated slotted and circular isoporous microfluidic membranes (Figure 1.3) by photolithography and electroplating. They found that membrane pore geometry played a significant role in flux decline without a sacrifice in selectivity. In another study, Metz et al. <sup>50</sup> developed a polyamide microfluidic device with nanoporous filtration areas by micromachining and ion track technology to generate microfluidic channels and sieves, respectively. The cross-sectional SEM images of the channel with sieves revealed perforation of only the top layer when the microfluidic channel was irradiated with ions of low energy and both layers when it was irradiated with ions of high energy.

The general advantage for the sieve method includes the flexible choice of membrane materials with the required pore size for specific applications. For example, these devices can be used for selective separation and sensitive detection of an element from a mixture. Another advantage is that during filtration, sometimes, unwanted air bubbles are trapped inside a microfluidic device. Cheng et al.<sup>101</sup> reported a bubble and clogging free microfluidic device by incorporating a degassing membrane at the top of the membrane micro-chip assembly as shown in Figure 1.1(b). Liu et al.<sup>99</sup> discovered a novel, simple, nozzle-type, membrane-based debubbler that can be readily integrated with a microfluidic channel for complete degassing and to avoid the formation of air bubbles inside a microchannel.

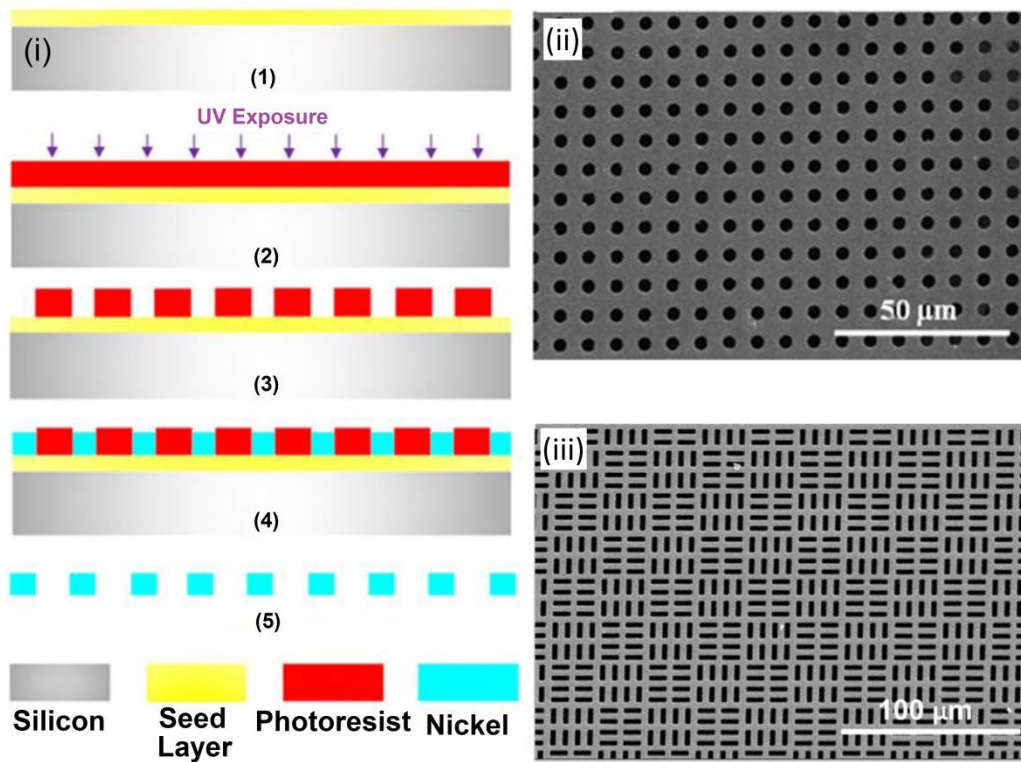


**Figure 1. 3:** Sieves made of impermeable membrane. (i) Microfabrication steps for the isopore membrane: (1) deposition of the seed layer (Cr/Cu) on a Si substrate, (2) spin-coating of a thick layer on the Si wafer and UV exposure through a mask, (3) development of the exposed film inside a developer, (4) electroplating of the Ni

between photoresist pillars, and (5) releasing the isopore membrane by dissolving the photoresist and seed layer in acetone and Cu etchant, respectively. (ii) SEM image of the circular pore membrane with 3 $\mu$ m diameter and (iii) SEM image of the slotted pore membrane with 3 $\mu$ m slit width <sup>63</sup>. Copyright 2015, reproduced with permission from Springer Berlin Heidelberg.

The most prominent challenge for the robust application of this method is the problem with sealing. To ensure sealing in a microfluidic membrane system clamping or stamping <sup>52, 102</sup>, lamination sheets <sup>53</sup> and crosslinking agents <sup>38, 103</sup> have been used so far.

### **1.2.2 Production of an array of pillars or structures**

In this section, the production of an array of pillars or structures used as on-chip membrane pores is reviewed. Microfluidic PDMS microchips are fabricated with an array of narrow parallel pillars or micro-posts, enabling a “side view” of the pores, which is complementary to the top view obtained in the membrane filtration studies using micro-sieves discussed earlier <sup>15, 41, 56, 58, 60–62, 66</sup>. The side view is important to observe the developing thickness of a fouling layer on a membrane surface.

Peterson <sup>104</sup> critically reviewed solid supports for micro-analytical systems including microchips with beads, incorporating membranes into chips, creating supports using microfabrication, fabricating gels and polymer monoliths within microfluidic channels. Gossett et al. <sup>95</sup> reviewed and designed weir-type, pillar type, and cross-flow type microscale filters. Yoon et al. <sup>65</sup> and Devendra et al. <sup>105</sup> developed a clog-free microfluidic filtration device by creating a single pillar row for micro-particle separation in a continuous operation. The SEM image of a single row of pillars is shown in Figure 1.4(a) <sup>65</sup>. A similar study was done by Chen et al. <sup>66</sup> with two consecutive PDMS pillar rows that was utilized for blood cell separation application. Chen et al. <sup>42</sup> used a dissolving mold technique to fabricate dissolvable polymeric pillar membranes. Marty

et al. <sup>67</sup> studied the impact of tortuosity on bacterial streamer formation by fabricating straight and staggered square arrays of pillars, as shown in Figure 1.4(b). A similar study was done by Biswas et al. <sup>106</sup> with a circular pillar arrangement to investigate the dynamics of bacterial streamer in a microfluidic system. Figure 1.4(c) shows a complex microfluidic system with asymmetric PDMS microchannel <sup>43</sup>.

Chen et al. <sup>66, 107</sup> designed cross-flow micro-separators for the separation of plasma and blood cells from human blood based on size-exclusion mechanism. The most significant advantage of this kind of device is that it enables the use of specific channel geometries. Also, as mentioned before, the side view of the pore adds significant value to the fouling investigations, which is not possible in sieve method.

### **1.2.3 Membrane-less filtration**

Here we refer to the filtration methods where separation is based on inertial flow, solute gradient, liquid membrane formation by two-phase or multi-phase flow, and the production of the lipid bilayer in a microfluidic device. For example, Seo et al. <sup>69</sup> and Warkiani et al. <sup>70</sup> reported inertial migration in a microfluidic device resulting in membrane-free MF, thus eliminating the need for filter replacement and external force. They introduced curvilinearity to the channel design where the equilibrium position of the particles depends on the balance between shear-induced and wall induced lift force and drag force. Thus, two-counter rotating vortices in the top and bottom half of the channel (i.e., Dean vortices) were generated and majority of the particles were trapped on the outer wall, facilitating the filtration. Shin et al. <sup>71</sup> developed membrane-less water filtration techniques by exposing negatively charged suspended particles (polystyrene, diameter  $\sim 0.5$   $\mu\text{m}$ , zeta potential  $\sim -70$  mV) to  $\text{CO}_2$ . Due to the dissolution of  $\text{CO}_2$  into the suspension, large

diffusion potential was generated by the dissociation of carbonic acid. Thus, a solute gradient was generated which drove the phoretic motion of the suspension either away from or towards the gas-liquid interface depending on the surface charge.

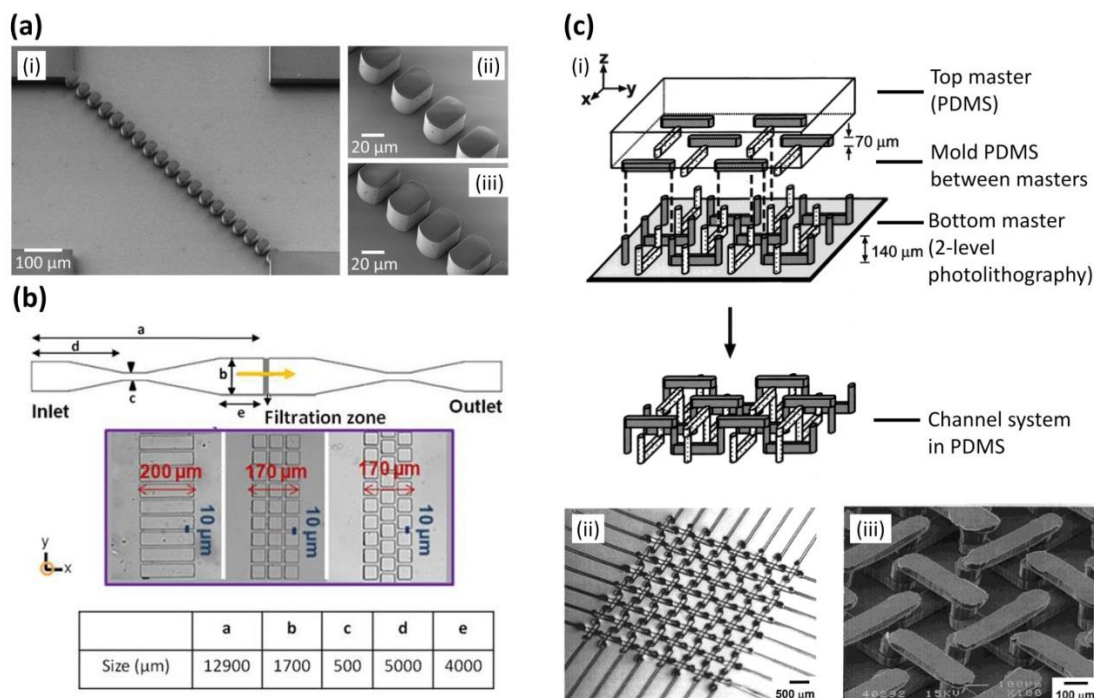


**Figure 1. 4:** Pillars or structures made of the impermeable membrane. (a) (i) SEM image of a microchannel containing a diagonally aligned single row of pillars (30  $\mu\text{m}$  thick pillars) with pillar gap (ii) 12  $\mu\text{m}$  for sieving PS particles, and (iii) 7  $\mu\text{m}$  for sieving cancer cells from whole blood <sup>65</sup>. Copyright 2016, reproduced with permission from Nature Publishing Group. (b) Schematic representation of the microfluidic channel working in a dead-end mode with dimensions as shown. The inset details the filtration zone with different micro-channel geometries: straight rectangular, straight squared and staggered squared pillars (from left to right) with 10  $\mu\text{m}$  gap <sup>67</sup>. Copyright 2014, reproduced with permission from AIP Publishing. (c) A microchannel system fabricated in a basket weave pattern. (i) Schematic of the top and bottom masters resulting in a membrane sandwich. Features in photoresist oriented in the y-direction are marked darker than those in the x-direction. (ii) The optical image (looking down the z-axis) of the PDMS membrane containing 8 $\times$ 8 channel system. The channels are 100  $\mu\text{m}$  wide (x- or y-direction), and each of the three levels used in the fabrication is 70  $\mu\text{m}$  high (z-direction) but is not enclosed. (iii) SEM image

of the basket weave. It was obtained by filling the microchannel with the epoxy prepolymer, curing under ultraviolet light for 10 min, and dissolving the PDMS casing in tetrabutylammonium fluoride <sup>43</sup>. Copyright 2000, reproduced with permission from American Chemical Society.

Another membrane-less filtration is the generation of a liquid membrane inside a microchip by two-phase, three-phase or multiphase flow. By two-phase flow, SooHoo and Walker <sup>74</sup>, separated leukocytes when whole blood cells were simultaneously exposed to polyethylene glycol and dextran phase streams. The cells were separated based on their differential affinity for the streams <sup>74</sup>. Maruyama et al. and Surmeian et al. <sup>73,77</sup>, created liquid membrane by three-phase flow through a micro-chip to isolate metal ions and to investigate molecular transport, respectively. Sato et al. <sup>76</sup> reviewed chemical and biochemical analysis systems using microfluidic devices for multi-phase flow liquid membrane production.

Lastly, the membrane-less microfiltration can be explored for the production of lipid bilayers. A model lipid bilayer comprised of single or multiple component lipids <sup>78</sup>. A lipid bilayer formation can last for 2-3 days allowing the robust characterization of the same lipid membrane <sup>78, 84</sup>. Malmstadt et al. <sup>79</sup> developed a self-assembled lipid bilayer structure driven by a solvent extraction process in a microfluidic device. Watanabe et al. <sup>81</sup> reported the formation of more than 10,000 asymmetric on-chip lipid bilayer membranes for pharmacological applications. While a thorough review is beyond the scope of this chapter, many studies can be found on artificial lipid membrane technology <sup>80, 82</sup>.

### **1.3 Microfluidic colloid filtration**

Colloids have a strong tendency to foul the membrane, considerably decreasing permeate flux and the quality of the filtrate. Numerous efforts have been made to understand the colloidal

fouling of membranes by ex-situ methods<sup>108, 109</sup>. However, challenges remain for the in-situ experimental technique to understand hydrodynamic effects, locate particle capture and quantify the physicochemical interactions occurring during colloid membrane filtration at the pore scale. Microfluidic membrane filtration is a breakthrough technology in understanding these fouling phenomena. Microfluidic membrane devices provide a large internal surface area to volume ratio that facilitates studying, analyzing and controlling membrane-colloid, and colloid-colloid physiochemical interactions. Microfluidic membrane mimics are handy tools to conduct a real-time visualization of complex colloidal suspension which causes fouling at the pore scale<sup>67, 80, 110–112</sup>. Moreover, using a microfluidic device, it is possible to generate a uniform array of pores to start with a simple flow and thus to perform a systematic analysis.

### **1.3.1 Fundamentals of colloid filtration**

Colloids are microscopically-dispersed, insoluble, suspended particles whose characteristic size, in at least one spatial direction, is between 1 nm and 1  $\mu\text{m}$ <sup>113</sup>. Colloids include a broad range of materials including particles, surfactants, and polymers and can be of three distinct phases (solid, liquid and gas), depending on the dispersed phase and dispersion media. In colloid membrane filtration, critical flux is defined as the permeate flux above which irreversible colloidal fouling occurs. At the beginning of filtration, critical flux is governed by a balance between drag force and colloid-surface interactions. Over time, colloid-colloid interactions also come to play. However, the dispersion stability and the fouling scenario may vary at the pore scale. Besides these two types of interactions (colloid-surface and colloid-colloid), at the pore scale, critical flux can be influenced by hydrodynamic effects, the local morphologies, and the topography of the membrane surface<sup>91</sup>.

To understand the process of particle capture on the membrane surface in colloid membrane filtration, surface interactions must be understood. Experimental observations with various colloidal dispersions have shown that colloidal stability due to colloid-surface interaction varies the permeate flux. Yao et al.<sup>114</sup> suggested a classical colloid filtration theory (CFT) to describe the filtration of colloidal particles. In this model, the removal of colloidal particles by a membrane is considered to follow the first-order kinetics, causing an exponential decline of colloidal concentration from the surface to the bulk. Tufenkji et al.<sup>115</sup> showed the deviation from the CFT in the light of DLVO theory. Their experimental study suggested that secondary energy minimum and surface charge heterogeneities played critical roles in significant deviation from CFT. Observation of these phenomena is very important to understand fouling behavior and the formation mechanism of a cake layer. A growing body of experimental research suggests that the deposition behavior of microbial particles (e.g., bacteria and virus) is inconsistent with the classical CFT. These results have important implications for the prediction of colloidal and microbial transport and their interactions in natural and engineered systems<sup>115, 116</sup>.

Theoretically, the surface interaction for colloid filtration is generalized into two categories: colloid-surface interaction and colloid-colloid interaction<sup>91</sup>. Colloid-surface interaction can be expressed by a net flux ( $J_{cs}$ ), which is a balance between the convective term and a diffusive term for a single particle-surface interaction and is given by

$$J_{cs} = J\phi - D \frac{d\phi}{dz} - \frac{D}{kT} \phi \frac{dV}{dz} \quad (1.7)$$

Here, the first term on the right-hand side is convective transport; the second term indicates diffusive transport and the third term shows the relocation of colloids to the membrane surface, due to surface interactions. The third term can be positive or negative respectively, depending on

the attractive or repulsive surface interaction potential. A schematic representation of a single particle interacting with surface and corresponding critical operating conditions for the deposited state is given in Figure 1.5(a) <sup>91</sup>.

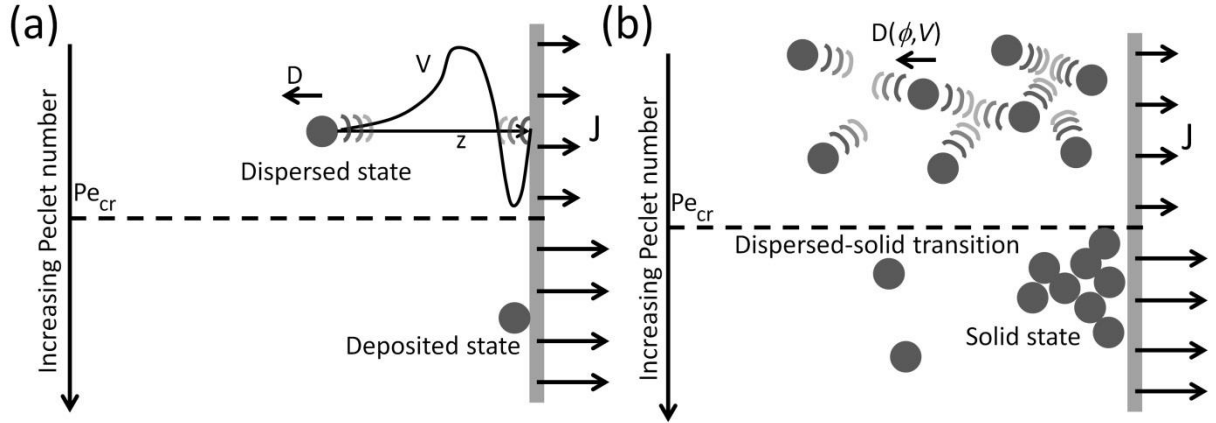


**Figure 1. 5:** (a) Colloid-surface interaction: a schematic of the representation of a single particle interacting with the membrane surface, and the corresponding critical condition is given for a deposited state. (b) Colloid-colloid interactions: a schematic of the representation of many-body colloid-colloid interactions, and the corresponding critical operating condition is given for a transition from dispersed state to solid state <sup>91</sup>. Copyright 2011, reproduced with permission from Elsevier.

A critical permeation flux ( $J_{cr}$ ) can be defined by obtaining a balance between the convective term (drag force) and the repulsive interaction between the colloid and the surface. The critical flux ( $J_{cr}$ ) can be calculated from the continuity equation and the DLVO potential interaction and can be linked to the critical Peclet number ( $Pe_{cr}$ ) as follows <sup>117</sup>

$$J_{cr} = \frac{D}{\delta} P_{cr} \quad (1.8)$$

$$P_{cr} = \ln\left(\frac{V_{cs}}{\delta}\right) \quad (1.9)$$

where  $\delta$  is the mass boundary layer thickness which depends on the fluid velocity,  $u$ .  $V_{cs}$  is the colloid-surface interactions expressed in terms of the colloid-surface interaction potential,  $V(z)$ , as,

$$V_{cs} = \int_0^{\infty} \left( e^{\frac{V_z}{kT}} - 1 \right) dz \quad (1.10)$$

A critical Peclet number ( $Pe_{cr}$ ) can be defined above which a solid phase transition occurs. For many-body colloid-colloid interactions, the net flux towards the membrane surface can be expressed as,

$$J_{cc} = J\phi - D(\phi, V_{cc}) \frac{d\phi}{dz} = J\phi - \frac{K(\phi)}{6\pi\mu a} V_{cc} \frac{d\Pi}{dz} \quad (1.11)$$

where the second term on the right-hand side represents the many-body colloid-colloid interactions. The modified diffusion coefficient  $D(\phi, V_{cc})$  can further be expressed in terms of the gradient of osmotic pressure via Stokes-Einstein relationship<sup>91, 117, 118</sup>. In this case, a transition to a solid-state occurs when the concentration is high enough that the attraction between colloid-surface overcomes the dispersive force. A schematic representation of the many-body colloid-colloid interactions with membrane surface, and critical condition for solid-state, is shown in Figure 1.5(b)<sup>91</sup>. In a cross-flow filtration, the  $Pe_{cr}$  can be expressed as<sup>91</sup>

$$P_{cr(cf)} = \frac{J\delta}{D_0} = \frac{V_{cc}}{kT} \int_{\Pi_b}^{\Pi_{cr}} \frac{K(\phi)}{\phi} d\Pi \quad (1.12)$$

which depends on the permeate flux, as well as, the thickness of the boundary layer,  $\delta$ . In dead-end filtration, the  $Pe_{cr}$  depends on both the permeate flux and the accumulated mass of colloids ( $V_a$  is proportional to filtered volume), which is expressed as<sup>91</sup>

$$P_{cr(de)} = \frac{JV_a}{D_0} = \frac{V_{cc}}{kT} \int_{\Pi_b}^{\Pi_{cr}} K(\phi) d\Pi \quad (1.13)$$

In summary, when analyzing the critical flux, one can decipher the formation of a fouling layer on the membrane surface by considering the influence of the hydrodynamics and the colloid-surface, and colloid-colloid interactions at the pore scale. Thus, developing an experimental method with the in-situ device would improve our understanding of colloidal fouling.

### 1.3.2 Microfluidic colloidal fouling

Several factors can affect the fouling behavior in a membrane<sup>8, 9, 108</sup>. A number of studies in the literature have shown that membrane fouling is influenced by the local structure of the membrane, as well as the interplay between the hydrodynamic and complex behavior of feed components and the membrane surface<sup>8, 9, 108, 109, 119</sup>. Based on earlier observations of on-chip microfluidic membrane fouling<sup>40, 90, 110</sup>, colloidal fouling mechanisms are classified as: (1) cake layer formation at the upstream (membrane surface); (2) pore fouling of membrane pores; and (3) streamer fouling at the downstream (permeate side). Table 1.2 summarises fouling phenomena observed in microfluidic filtration devices.

**Table 1. 2:** Categorization of colloidal fouling observed in a microfluidic membrane filtration system.

<b>Mechanism</b>	<b>Colloids</b>	<b>Location</b>	<b>Factors affecting this phenomenon</b>
<b>Cake layer fouling</b>	Dilute or stable suspensions	Upstream of membrane	<b><i>Hydrodynamic conditions</i></b> Flux, crossflow velocity, pressure
<b>Pore fouling</b>	Aggregates and flocs	Membrane pore	<b><i>Feed solution properties</i></b>
<b>Streamer fouling</b>	Concentrated or unstable solution, viscoelastic solution	Downstream of membrane	Foulant type, concentration, pH, ionic strength, the presence of coagulants and flocculants <b><i>Surface interaction</i></b> Surface charge, surface functional group

			<p><i>Effect of pore geometry</i></p> <p>Microchannel entrance geometry</p> <p>Sieve size</p> <p>Gap between pillars</p>
--	--	--	--

### ***Cake layer fouling***

At the beginning of filtration experiments, suspension stability plays an essential role in the deposition of particles on the membrane surface. Over time, stable arches are formed at the entrance pore, from which valuable information about a balance between hydrodynamic force and interfacial forces can be obtained <sup>120</sup>. Agbangla et al. <sup>121</sup> identified the critical conditions for the formation of arches, leading to deposit formation, in terms of particle concentration, solution velocity, and critical flux. As filtration continues, deposit formation eventually leads to stable cake layer formation. Ngene et al. <sup>53</sup> described a new method for obtaining a side view of the formation of a homogeneous cake layer at the channel entrance by the dead-end filtration of 6µm polystyrene particles.

During filtration, hydrodynamic effects, particle suspension properties (ionic strength and pH), surface interaction potential, and channel geometry play significant roles in particle capture as listed in Table 1.2. An experimental study by Bacchin et al. <sup>89, 91, 122</sup> showed two types of fouling phenomena occurring in PDMS MF microfluidic membrane mimics. Latex particles (4.9±0.21µm) with a negatively charged functional sulfate group were used as suspensions in two surface conditioning of PDMS surface: more hydrophilic surface conditioning by 10<sup>-1</sup>M KCl and more hydrophobic surface conditioning by ultra-pure water <sup>91</sup>. For ultrapure water conditioning, they observed cake layer formation (Figure 1.6(a) (i)). On the contrary, for a more

hydrophilic surface, they observed dendrites formation (Figure 1.6(a) (ii)) after 90 min of filtration. They explained that more hydrophilic KCl conditioning caused lower collision efficiency of particles with the PDMS wall at the microchannel entrance. On the contrary, the formation of arches could be promoted by an efficient lateral collision between the particles and the wall, eventually forming a cake layer for a less hydrophilic surface <sup>91</sup>. From their experimental findings, Derekx et al. <sup>123</sup> claimed that the PDMS microfluidic mimic membrane with a 20 $\mu$ m pillar gap was prone to fouling by latex particles of 1 $\mu$ m to 1.25 $\mu$ m diameter. A similar cake layer formation was observed by Linkhorst et al. <sup>90</sup>. They observed a colloidal cake layer formation when they infused microgels (2.2 $\mu$ m diameter) through 20 $\mu$ m pillar gap under constant flux (Figure 1.6(b)(i)) <sup>90</sup>. A longer constant flux filtration resulted in the growth of the cake layer and an increase in the trans-cake pressure drop over time. Eventually, the microgels escaped stress by reorganising into energetically favourable structures such as larger crystalline regions (Figure 1.6(b) (ii)).

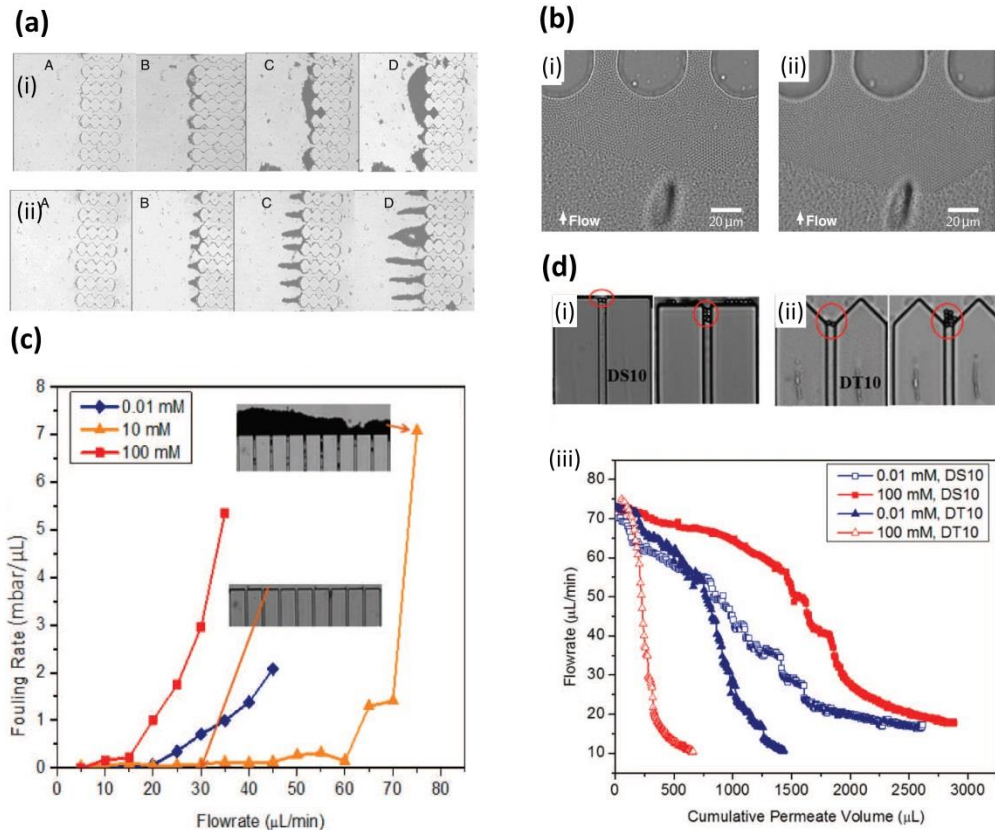


**Figure 1. 6:** (a) Microfluidic observation of cake layer formation: microfluidic images showing stable cake layer formation with time for 20μm pillar gap for (i) ultrapure water conditioning and (ii) KCl solution conditioning of PDMS surface <sup>91</sup>. Copyright 2011, reproduced with permission from Elsevier. (b) (i) The build-up of the cake layer during filtration of microgel suspension and (ii) increasing pressure increases crystallinity <sup>90</sup>. Copyright 2016, reproduced with permission from Nature Publishing Group. (c) Effects of ionic strength: fouling rates calculated from the flow stepping experiments at different solution ionic strengths: 0.01mM, 10mM and 100mM of KCl. The inset images are the observations for 10 mM suspensions before and after deposit formation, and (d) Effect of entrance geometry on flow rate and fouling with square entrance (DS10) and tilted funnel entrance (DT10). Filtration results were at constant pressure (200mbar) for low (0.01mM) and high ionic strength (100mM) of KCl demonstrating higher flux decline for DT10. D denotes dead-end flow, S and T denote square and tilted pillars, respectively, and 10 is the channel width <sup>110</sup>. Copyright 2016, reproduced with permission from American Chemical Society.

Sendekie et al.<sup>110</sup> showed colloidal surface interactions played a significant role in the permeability at the pore scale. At first, critical flux was determined by a flux stepping experiment. Sulfate-modified polystyrene particles (5 $\mu$ m) were used under KCl conditioning (0.01mM, 10mM, and 100Mm) as fouling material (Figure 1.6(c)). They found that particle capture (fouling rate) was more significant for low flow rates and high ionic strengths. This was because increasing ionic strength reduced electric double layer (EDL) repulsion and lowered the energy barrier for particle-surface interaction (Figure 1.6(c)). Therefore, critical flux increased when repulsive forces were more dominant for colloid-surface interactions of 10mM KCl solution (Figure 1.6(c)). Bacchin et al.<sup>89</sup> experimentally demonstrated the effects of channel connectivity and tortuosity on the particle capture by using a straight rectangular microchannel, and a straight and staggered array of square pillars in PDMS microchip. They concluded that the progressive capture of particles occurs on the internal layers as tortuosity increases. Later on, the pore plugging progressed toward the upstream, blocked the channel entrance, and led to the formation of a cake layer. In addition, greater particle deposition on the surface of the square pillars was observed when the pillars were staggered. The increase in fouling by increasing the tortuosity was attributed to the presence of more flow stagnation zones<sup>110</sup>. Sendekie et al.<sup>110</sup> investigated the effect of microchannel entrance geometry on permeation and fouling properties (Figure 1.6(d)). Permeability loss was more severe for tilted funneling entrance (DT10) compared to the square entrance (DS10) though greater particle deposition was observed for DS10. This was because the square geometry resulted in a larger flow stagnation area<sup>110</sup>, which was in good agreement with the classical CFT<sup>124</sup>. From Figure 1.6 (d) (iii), they attributed the higher flux decline for DT10 to pore fouling phenomenon and less flux decline for DS 10 to more cake layer formation.

### *Pore fouling*

Cake layer formation and pore-clogging can be reversible through collapse and expulsion of deposited particles or aggregates. When the flow velocity over adhered particles, or the hydrodynamic forces exceed the repulsive surface interaction force (due to particle-particle and particle-surface interaction), the aggregate begins to collapse or sliding off the walls to the pore<sup>110</sup>. As a consequence, it can substantially affect the permeation flow rate. A similar collapse of the cake layer was observed in membrane filtration by other researchers<sup>125, 126</sup>.

During colloidal fouling, colloidal particles aggregate, coagulate, flocculate and begin to plug the membrane pores. Pore fouling results from progressive particle accumulation, as the pores begin to narrow with the formation of more robust flocs or stable arches. Fouling can be a result of all the factors listed in Table 1.2, and hydrodynamic effects can be altered due to pore fouling. The process of pore fouling continues until all pores are blocked, resulting in a significant drop in permeability for constant pressure filtration, and pressure build-up for constant-flux filtration. Sendekie et al.<sup>110</sup> made a significant observation of these phenomena from a microfluidic experiment. Figure 1.7(a) shows pore fouling downstream of pillars for a 10mM KCl solution. They reported the presence of a secondary energy minimum for a 10mM KCl solution along with the moderate colloid-surface repulsion at the channel gap. As a result, fluid drag force and shear, dragged particles along the pore wall until they reach the stagnation point in the downstream of pillars (Figure 1.7(b)).

Sendekie and Bacchin<sup>110</sup> also successfully demonstrated the dynamics of pore-clogging with a reasonable relation to an energy barrier. Based on their study, three pore-clogging scenarios can be observed: the panic; the herding instinct; and the sacrifice. Figure 1.7(b) summarises clogging dynamics based on variations in the ionic concentration of KCl. Considering colloid-colloid and

colloid-surface interactions, as well as the deposit structure, specific resistance, and relaxation property, they explained the scenarios mentioned above. First, high repulsive barriers for 0.01 mM KCl caused force chains that sustained the clogs and thus has led to the formation of dense arches (the panic). Second, a significant secondary minimum at 10 mM KCl caused coordinated transport where a pulling effect caused by attraction forces between particles enabled the transfer of the clusters through the bottleneck and delayed the clog formation (the hardening instinct). Third, the low repulsive barrier at 100 mM KCl caused a high collision frequency, leading to the attachment of particles to the walls and the formation of fragile clogs (the sacrifice)<sup>110</sup>.

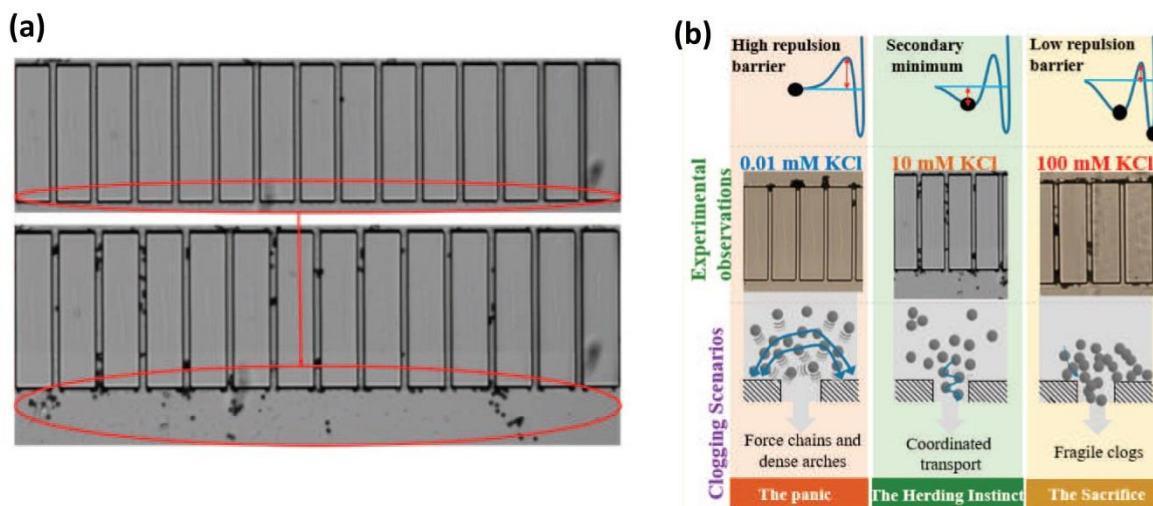


**Figure 1. 7:** (a) Observation of pore fouling for 10mM KCl solution at the downstream of pillars. (b) Demonstration of the link between DLVO theories, the experimental results, and the fouling scenarios. Copyright 2016, reproduced with permission from American Chemical Society.

### ***Streamer fouling***

Colloidal fouling in a porous media can lead to streamer formation at the downstream pores<sup>127</sup>,<sup>128</sup>. Streamers are a filamentous structure containing bacterial cells encapsulated in a biopolymer matrix called extra-cellular polymeric substances (EPS)<sup>129</sup>, usually formed in hydrodynamic

flow condition<sup>130, 131</sup>. The formation of bacterial streamers can significantly affect fouling of the filtration unit and lower its performance<sup>67, 106, 132</sup>. What's more, medical devices are prone to fouling due to streamer formation<sup>130, 133</sup>. Biswas et al.<sup>106</sup> studied the deformation mechanism of bacterial streamer occurring at the downstream location of micro-pillars arranged in a staggered pattern (pillar gap 10 $\mu$ m) (Figure 1.8(a)). Marty et al.<sup>67, 127</sup> fabricated microfluidic membrane mimic with dead-end and cross-flow filtration modes to observe physical processes governing biofouling. Direct observation of bacterial streamer formation was conducted downstream of the pillars (pillar gap 10 $\mu$ m or 20 $\mu$ m) using *E. coli*, *P. aeruginosa*, and *S. aureus* bacterial suspensions. 200 $\mu$ m long streamer grew after an hour, filtration experiment. Streamer growth and morphology were found to be influenced by the geometry of the device. Streamers were longest for the staggered arrangement of square pillars<sup>127</sup>.

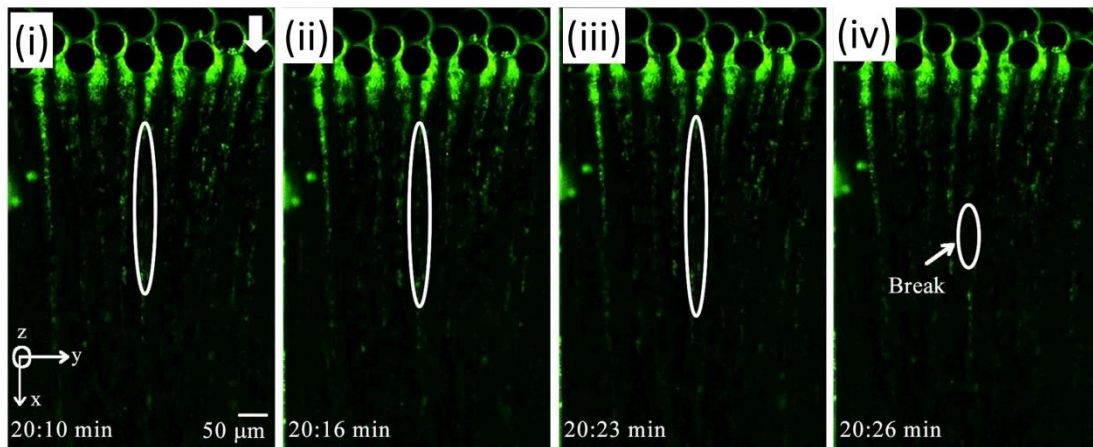


**Figure 1. 8:** (a) Bacterial streamer formation and breaking with time (*P. fluorescens*) under fluorescence imaging with Green filter cube at  $U = 8.92 \times 10^{-4}$  m/s. (i–iv) Show the stretching of one streamer with time, and the final breaking point shows in (iv). The arrow is showing the flow direction<sup>106</sup>. Copyright 2016, reproduced with permission from Nature Publishing Group.

## **1.4 Challenges to study membrane fouling in ex-situ experiments**

The major challenge in all membrane processes is the fouling, and a systematic understanding of the fouling mechanisms remains unexplored<sup>134, 135</sup>. For many decades, cake layer/gel formation<sup>136, 137</sup>, concentration polarization<sup>138</sup>, and pore-clogging<sup>139, 140</sup> were known as the primary mechanism for flux decline through the membrane<sup>141</sup>. However, we encountered a new kind of fouling called streamer fouling, which occurred on the permeate side. A particular interest of fouling was the irreversible combined fouling (colloidal and organic), which showed more severe flux decline than the individual fouling phenomena<sup>142-144</sup>.

In general, a membrane is considered an opaque system in which post-filtration analysis of the fouling layer and permeate stream is conducted to evaluate the filtration process. However, capturing the real morphology of the fouling layer might be challenging in common ex-situ experiments as the soft foulant materials might collapse during drying and in high vacuum conditions. This challenge can be overcome using a microfluidic system, mimicking a membrane module. The in-situ microfluidic system can be used for analyzing real-time fouling at pore-scale under optical microscopy.

## **1.5 Research objectives**

In summary, based on the above literature, we can conclude that the microfluidic filtration system can serve as an important tool to study the colloidal fouling. Cake layer formation and pore-clogging have been studied vigorously, but streamer formation is yet to be explored. Also, among all kinds of membrane fouling (colloidal, organic, and biofouling), we found limited studies that examined the severe effect of combined colloidal and organic fouling on membrane

performance<sup>142, 144–148</sup>. In this regard, a microfluidic device has become an essential tool to explore more about fouling at pore scale.

The interesting questions which remained unanswered are: (1) what are the microscopic events of membrane fouling? (2) Do parameters like flow rate, pH, pressure, and geometry play a crucial role in combined fouling in a microfluidic device? (3) How the colloidal fouling dynamics can be correlated to the membrane performance?

Given that, the main objectives of this research are the real-time investigations of colloidal fouling in a microfluidic device and correlating the fouling phenomena with membrane performance. In pursuit of these objectives we have divided the research plan into three parts. We first investigated real-time combined fouling in microfluidic porous media mimics with a pillar gap 25 $\mu$ m. Then, we studied the combined and individual fouling phenomena in an MMM device with pillar gap 2 $\mu$ m. Finally, we calculated the interaction energies of components (foulants and membranes) and investigated the role of secondary energy minimum on fouling phenomena in MMM device. In summary, the main objectives of this research are as follows:

1. Real-time investigation of combined colloidal & organic fouling in a microfluidic system (pillar gap 25 $\mu$ m).
2. Real-time investigation of combined colloidal & organic fouling in a microfluidic membrane mimic (MMM) device (pillar gap 2 $\mu$ m).
3. Correlation of fouling at pore-scale with the interaction energies of microfluidic membrane material and foulants.

## 1.6 Thesis structure

The present dissertation is organized in a paper-based format. Chapter 1 provides a review of the microfluidic mimic for colloidal membrane filtration and several methodologies for fabricating microfluidic membrane on-chip.

Chapter 2 reports the phenomenon of formation of colloidal aggregates in the form of thin slender strings called abiotic streamers/colloidal streamers when a polyacrylamide (PAM) solution, laden with polystyrene (PS) beads is introduced into a microfluidic device containing an array of micropillars. This phenomenon was observed only when PAM and dilute solutions of PS beads are introduced into the microfluidic channel through two separate inlets. The particle aggregates initially had a string-like morphology that were tethered at their ends to the micropillar walls, while the structure remained suspended in the fluid medium. Such morphology inspired us to name these structures as colloidal streamers. The flow regime under which colloidal streamer formation was observed is quantified through state diagrams. We discussed the streamer formation timescales and also showed that the streamer formation is likely the result of flocculation of PS beads. Streamer formation has implications in investigating downstream fouling phenomena in microfluidic membrane fouling.

Chapter 3 presents the summary of fouling phenomena observed in an MMM device and correlates the fouling phenomena with the membrane performance parameters like flux, pressure and fouling percentage. The fouling study was performed with foulants such as polystyrene particles and large polymeric molecules in an MMM device consists of a staggered arrangement of pillars with a pillar gap  $2\mu\text{m}$ , mimicking a microfiltration membrane pore size for the first time. This device enabled real-time visualization and analysis of fouling at pore-scale. Different

fouling scenarios were investigated by conducting constant-pressure experiments and considering three different types of foulants: polystyrene particle solution (colloidal fouling), polyacrylamide polymer solution (organic fouling) and a mixture of these two solutions (combined fouling).

Chapter 4 investigates the fouling of polystyrene (PS) and silica (SiO<sub>2</sub>) in a microfluidic membrane mimic (MMM) device. The MMM device consists of an array of micro-pillars, mimicking the pore size (hydraulic diameter,  $d_h \sim 3\mu\text{m}$ ) of a microfiltration membrane. The MMM device enabled real-time visualization and analysis of the fouling phenomena at pore-scale. The constant-pressure dead-end filtration resulted in cake layer with no downstream fouling for SiO<sub>2</sub> and cake layer with downstream fouling for PS at different ionic concentrations. The fouling trends were confirmed by the measured interaction energies among foulant particles and between foulant and clean membrane by contact angle method. Experimental results suggest that the presence of higher energy barrier and secondary energy minimum plays an important role in mitigating membrane fouling. Additionally, microfluidic back-washing experiments showed that the majority of the PS particles were released from the cake layer by water channel formation while in case of SiO<sub>2</sub> formation of water channel was not prominent.

Chapter 5 summarizes the significant findings and provides concluding remarks and possible future directions of research.

## **1.7 Author's contribution**

In this dissertation, a novel fouling phenomenon called colloidal streamer fouling has been observed, identified and quantified. The author established a microfluidic membrane mimic

device (MMM) (hydraulic diameter  $\sim 2.86\mu\text{m}$ ) that can mimic a microfiltration membrane pore size (0.1-10 $\mu\text{m}$ ). The author directly contributed to the design and fabrication of the MMM device. The author performed a parametric study on the effect of influential parameters on fouling at pore scale and visualized colloidal streamer fouling using fluorescence and confocal microscopy. All the data analysis and the experimental uncertainty analysis were performed by the author. The author designed the photomask, performed photolithography, silicon wafer etching, PDMS casting on silicon mold by using cleanroom facilities available at nanoFAB at the University of Alberta. The author prepared the foulant samples, conducted all fouling experiments, identified, analyzed and quantified several fouling phenomena. Image and video analysis software like NIS element AR interface software, ADOBE FIREWORKS CS6, ADOBE PREMIERE PRO, ADOBE PREMIERE RO AFTER EFFECTS CC, Origin, MATLAB are used for data processing. The author performed the SEM, zeta potential analysis, rheological measurements. The author would like to thank Dr. Ishita Biswas, Dr. Mahtab Hassanpourfard, Dr. Tanushree Ghosh and Md. Farhad Ismail for their valuable insights to this research.

# Chapter 2

## Abiotic streamers in a microfluidic system†

---

†The materials of this chapter has been published in “N. Debnath, M. Hassanpourfard, R. Ghosh, J. Trivedi, T. Thundat, M. Sadrzadeh & A. Kumar, “Abiotic streamers in a microfluidic system”, *Soft Matter*, Vol. 13, I. 46, p. 8698- 8705, 2017.”

## 2.1 Introduction

Flow of colloidal dispersions through porous media is a topic of substantial contemporary interest due to its applications to both natural<sup>149, 150</sup> and artificial systems<sup>151, 152</sup>. Even in this category, suspensions of particles dispersed in viscoelastic media are increasingly relevant due to their applications in enhanced oil recovery<sup>153, 154</sup>, drug delivery and diagnostics<sup>155, 156</sup> and also to manufacture polymer nanocomposites<sup>157</sup>. A popular set up to investigating such flows through porous media are their microfluidic devices<sup>132, 158, 159</sup>. These are not only geometrically similar but can also capture several aspects of the complexities of flow in porous media such as the presence of both shear and elongation flow<sup>160</sup>, while amenable to optical microscopy and other analytical techniques.

For instance, Campo-Deano<sup>160</sup> reported gelation when Boger fluids made from polyacrylamide (PAM) and NaCl was flown through a microfluidic device with micropillar array. Interestingly, it is well known that when colloidal suspensions experience flow, distinct structural aggregation states can be observed<sup>161–163</sup>. But in non-Newtonian fluids, flow-induced alignment and/or particle aggregations are observed for even dilute flows<sup>163, 164</sup>; a phenomenon not seen for particles dispersed in Newtonian fluids. In another study Babayekhorasani et al.<sup>165</sup> used numerical studies to study the flow of dispersion of particles through ordered and disordered two-dimensional porous media analogs. They found that the confining effects of geometry at the microscale coupled with solution rheology dictate particle dispersion. Despite these studies, understanding of flow of colloidal suspensions in non-Newtonian media in porous media analogs remains poorly understood<sup>161, 162, 165</sup>. In particular, flow induced aggregations in dilute colloidal suspensions in porous architecture need to further investigated.

Here we investigate the flow of a dilute solution polystyrene beads (PS) suspended in PAM using a micro fabricated porous media analog consisting of an array of micropillars arranged in a staggered grid pattern. Our device exhibits pore-sizes that are  $O(10^{-5})$  m, a range that is often found in artificial and natural porous structures such as microfiltration membranes and soil<sup>159, 166, 167</sup>. We employed a two-inlet microfluidic channel which then leads to an array of micropillars as our porous media analog. In this work, we investigated the combined flow of PAM (0.2% w/w) and polystyrene bead solutions (0.1% w/w) through this device. The concentrations of PAM and PS are denoted by  $C_{PAM}$  and  $C_{PS}$  respectively. The two solutions were introduced into the microchannel through the separate inlets (PAM at volume flow rate  $Q_{PAM}$  and PS bead solution at  $Q_{PS}$ ) resulting in a flow exhibiting very low Reynolds number (i.e.  $Re \ll 1$ ). It was found that for flow neutral pH PS solutions, when the mass flow rate of PS beads exceeded PAM solution, i.e.  $C_{PS}Q_{PS} \geq 0.6C_{PAM}Q_{PAM}$  PS beads aggregated to form thin slender string-like structures, We named this string-like structures ‘streamers’; this name is inspired by similar structures found in microbial flows through porous media and microchannels<sup>132, 168</sup>. Streamer formation was also observed for different pH PS solutions although the relative mass flow rates necessary varied considerably. The myriad results are condensed into state diagrams to succinctly quantify the phenomena. We hypothesized a flocculation-based route to streamer formation and find that ex situ aggregation of PS beads in the presence of PAM is able to qualitatively explain the results of in situ experiments.

## 2.2 Materials and Methods

### ***PAM and PS solution preparation***

The Polymer solution was prepared by dissolving 1g of polyacrylamide powder (PAM: A-8354, Kemira, AB, Canada) into 500mL of normal tap water. Then, the PAM solution (0.2% w/w) was agitated at 600 rpm with an overhead stirrer (Caframo, ON, Canada) for about three hours to ensure proper mixing (Figure 2.1). Further, Fluorescein sodium salt (Excitation at 460nm & Emission at 515nm) (Sigma-Aldrich, ON, Canada) was also added to the PAM solution to make it green fluorescent. The particle solution was prepared by diluting 200nm amine-coated PS beads (Excitation at 580nm, Emission at 605nm) (Life Technologies, ON, Canada) with deionized water till a 0.1% w/w suspension of PS beads was attained. Under fluorescence microscopy the PAM and PS beads appeared green and red, respectively. PAM and PS solutions were separately injected into the two inlets of microfluidic channel by using a dual-syringe pump (Harvard Apparatus, MA, USA). The flow rate was controlled by the pump to maintain a constant volume flow rate for both syringes. The syringes (3 mL each) were connected to the microchip by Tygon tubing (ID 0.01mm, Fisher Scientific, AB, Canada).

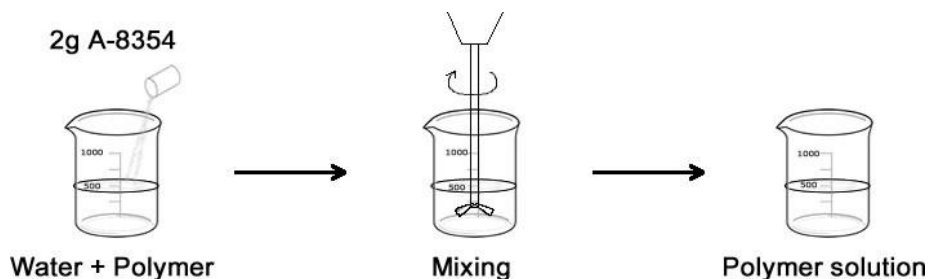


**Figure 2. 1:** Schematic of the preparation of polymer solution at room temperature. 2g of polymer were mixed with 500ml of normal tap water (0.2% w/w PAM solution) and mixed at 600 rpm for at least 3 hours to ensure homogenization.

## Microfluidic chip fabrication

The polydimethylsiloxane (PDMS, Sylgard 184, Dow Corning, NY, USA) chip with the required microchannel design was prepared by conventional photolithography from a 4" silicon master mold. Our microfluidic device contained two inlets (Figure 2.2(a)) and a central channel containing an array of micropillars with an out-of-plane height  $h$  and diameter  $d$  of  $50\mu\text{m}$  each (Figure 2.2(b),(c)). The distance between center of pillars and gap between two consecutive rows,  $s$ , was  $75\mu\text{m}$ . Width,  $w$ , of the microchannel was  $625\mu\text{m}$ . The array consisted of 8 (across breadth)  $\times$  50 (across length) micropillars (Figure 2.2(b),(c)). The PDMS stamps and cover slip were bonded together by using oxygen plasma-activated bonding for 30 seconds. Further, they were annealed at  $70^\circ\text{C}$  to ensure proper sealing as described in our previous study<sup>168</sup>.

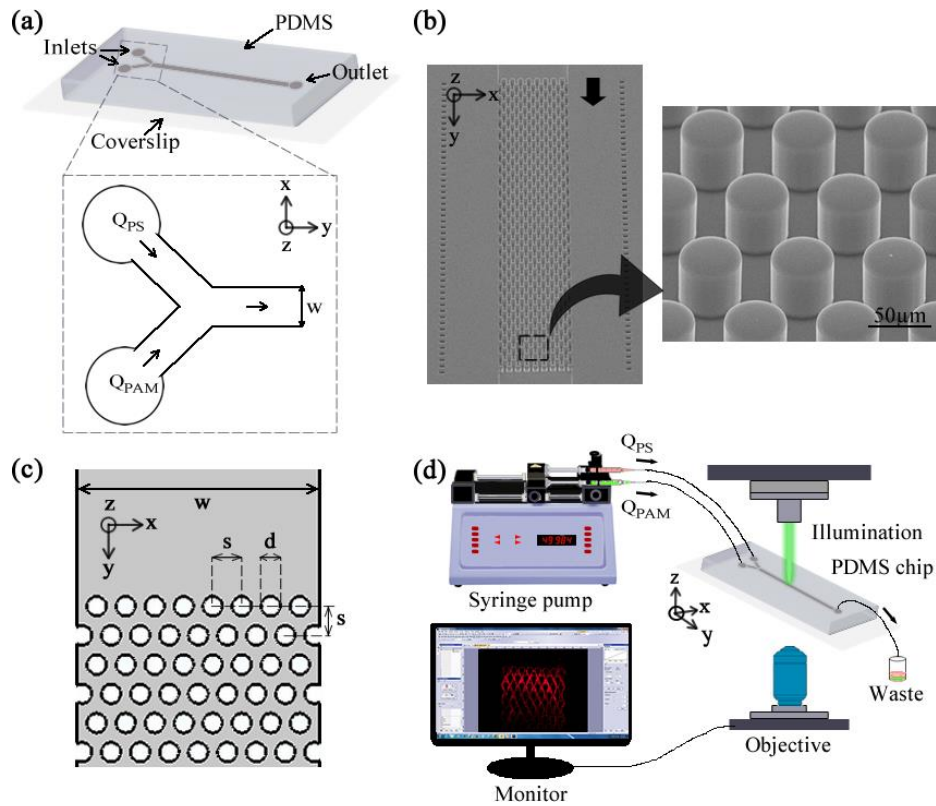


**Figure 2. 2:** (a) A schematic of the microfluidic device having two inlets and one outlet. The blow-out section shows the entry Y-channel where mixing process occurs. Polymer solution (PAM) and polystyrene solution (PS) were injected with a constant volume flow rate  $Q_{PAM}$  and  $Q_{PS}$ . Total width of the channel is  $w$ . (b) SEM image of the microchannel clearly shows the uniformity of micropillars. (c) Top-view of the microfluidic device. The diameter ( $d$ ) and out of plane height ( $h$ ) of the pillars both are  $50\mu\text{m}$  and width ( $w$ ) of the device is  $625\mu\text{m}$ . The distance between the center of the pillars ( $s$ ) and two rows of the consecutive pillars ( $s$ ) is  $75\mu\text{m}$ . (d) A schematic of the total experimental set up. PAM (green) and PS (pink) solutions were transported through two inlets of the microfluidic device with a dual syringe pump which generates a constant volume flow rate  $Q_{PAM}$  and  $Q_{PS}$ .

### ***Microscopy***

The entire microchip was placed on a stage of an inverted optical (Nikon Eclipse Ti) microscope and a confocal microscope (Olympus IX83) (Figure 2.2(d)). Fluorescent microscopy directly probe imaging and videography by using either a GFP Long-pass Green filter cube or Texas Red filter cube (Nikon & Olympus). Equivalent diameter calculations were performed using the image-processing module in the Nikon NIS-Element AR software interface. Scanning electron microscopy (SEM) images were taken using a Field Emission-Scanning Electron Microscope (Zeiss, Oberkochen, Germany). Each sample was air-dried and gold sputtered (Denton Vacuum, Desk II, Moorestown, New Jersey) before SEM imaging. Images were taken at 20kV with In-lense secondary electron detector.

### ***Rheological measurements***

A standard cone and plate rheometer (C-VOR 150 Peltier Bohlin Rheometer, Malvern instruments, USA) was used to investigate the rheological properties of the polymer solution. The distance between the plate and the cone, at the center, was  $150\mu\text{m}$ . The diameter of the

stationary plate at the bottom was 60 mm, and the rotating upper cone had a diameter of 40mm with a 4° angle. All experiments were performed at 20°C.

### ***Zeta potential measurements***

Zeta potential measurement for 50 mL 0.1% PS dispersions were obtained with a Zetasizer Nano ZS (Malvern, USA) to assess the surface charge as a function of solution pH. PS bead solution pH was adjusted between 3-10 by addition of HCl or NaOH solution and the solution pH was measured using pH test strips. Experiments were performed at 20°C and were repeated three times.

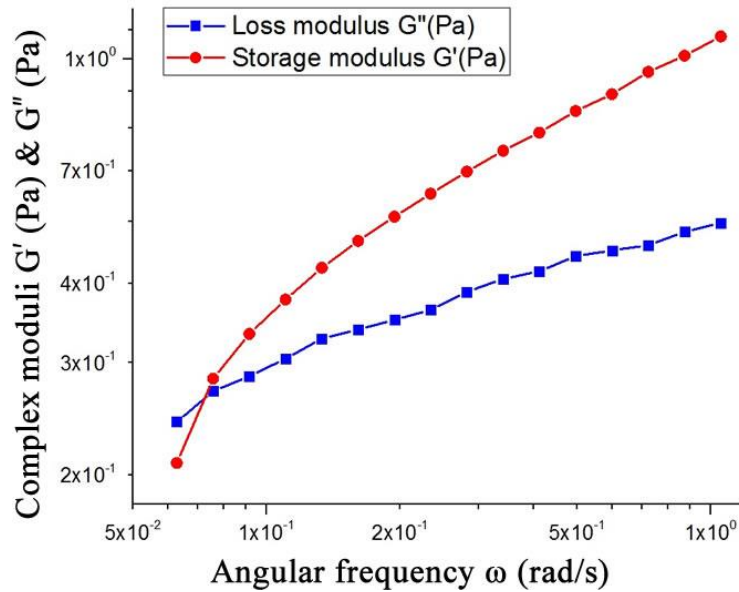
### ***Molecular weight measurement***

The molar mass of the PAM solution was measured by using an Assymetric Flow Field Flow Fractionation (AF4) system (AF2000 MF Separation System-Aqueous Solvents, Postnova Analytics, USA). A solution of 0.2% PAM was prepared in 0.5% NaCl brine water. The same brine solution was used to calibrate the AF4 system as described elsewhere<sup>169</sup>. Experiments were performed at 20°C and were repeated three times.

## **2.3 Results**

Our microfluidic device had two inlets. PAM solution was injected from the first port at a (volumetric) flow rate of  $Q_{PAM}$  and a concentration of  $C_{PAM}$ . Amine coated PS bead suspension in deionized (DI) water at neutral pH was pumped from the second port at a flow rate of  $Q_{PS}$  and a concentration of  $C_{PS}$  (Figure 2.2). The two streams merged at a Y-shaped intersection before entering the central section of the microfluidic channel (Figure 2.2(a)). The central section of the device consisted of an array of PDMS micropillars in a staggered grid pattern. The micropillars

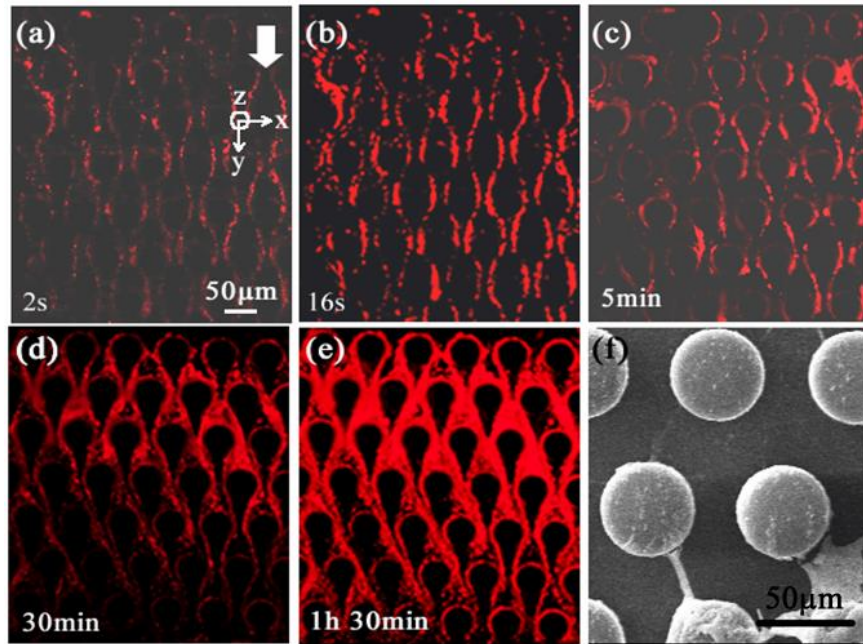
had a diameter ( $d$ ) of 50 microns and were spaced 75 microns apart ( $s$ ) (Figure 2.2(b),(c)). The average velocity scale ( $\bar{U}$ ) in the device is defined by the relationship  $\bar{U} = (Q_{PAM} + Q_{PS})/(w \times h)$ , and the flow rates  $Q_{PAM}$  and  $Q_{PS}$  used in this study ensured that the resultant flow in the device was in the creeping flow regime ( $Re \ll 1$ ). The PAM solution is strongly viscoelastic with a relaxation time scale,  $\lambda$ , of approximately 13 s (Figure 2.3).



**Figure 2. 3:** Complex moduli for PAM (0.2%) as a function of angular frequency at low shear. Relaxation time ( $\lambda$ ) for PAM (0.2%) solution is  $\sim 13$ s.

Initially, the concentrations of PAM and PS beads, i.e.  $C_{PAM}$  and  $C_{PS}$ , were both kept constant at 0.2 % w/w and 0.1% w/w respectively. At this fixed concentration, when PAM and PS beads solutions were flown through the microfluidic device at flow rates of  $10 \mu\text{L/h}$  and  $40 \mu\text{L/h}$  respectively, we observed that there was an immediate localization of PS beads near micro-pillar walls in the form of string-like filamentous structures (Figure 2.4(a)). The structures are tethered to the micropillar walls, while the rest of the structure extends with the background flow. We named these structures “streamers” motivated by morphologically similar structures seen in

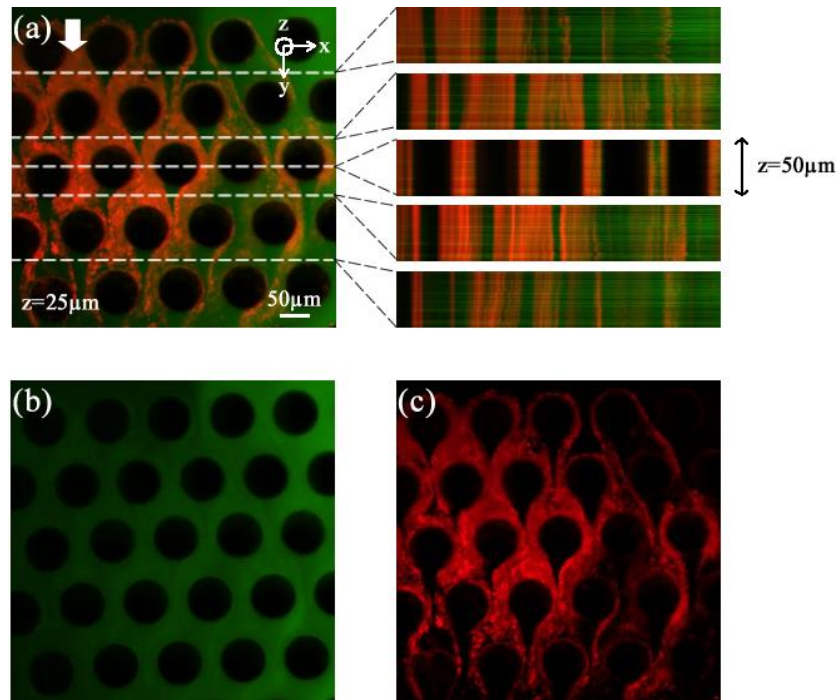
bacterial aggregations subjected to continuous hydrodynamic flow<sup>132, 166, 168, 170–173</sup>. Streamer formation represents an irreversible aggregation; when the flow is stopped the structure remains undisrupted and shows no appreciable diffusive disintegration in the time scale of experiments.



**Figure 2. 4:** Streamer formation imaged using the Texas Red filter cube. ((a)-(e)) Time-lapse imaging of the streamer formation and maturation at for flow rate  $Q_{PAM}=10\mu\text{L/h}$  and  $Q_{PS}=40\mu\text{L/h}$ . (f) SEM imaging of streamer remnant in the microfluidic device.

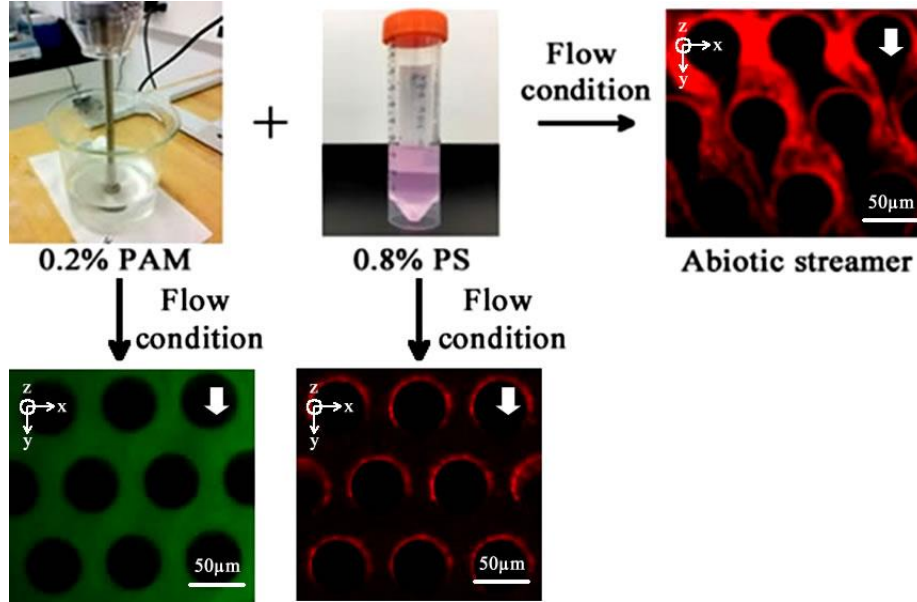
For the streamers shown in Figure 2.4, the particular dilutions for PAM and PS were carefully chosen through a series of optimization experiments (discussed later) that resulted in stable and observable streamer formation. These experiments also revealed that streamers were not observed below a certain cutoff PS concentration. However, when they successful form, these structures tend to be pervasive throughout the microfluidic device i.e. they occurred between a majority of the first 10 rows of micropillars. Two distinct time-scales were observed for the abiotic streamer under present experimental conditions (i) Streamer formation time-scale

( $\tau_{form}$ ), which was of the order of the a few seconds i.e.  $\tau_{form} \sim O(10^0s)$ . At these short time-scales the streamers achieve and maintain a high aspect ratio (length/radius  $\sim O(10)$ ). (Figure 2.4(a)-(c)) and, (ii) Clogging time-scales ( $\tau_{clog}$ ), which was of the order of several minutes i.e.  $\tau_{clog} \sim O(10^3s)$  (Figure 2.4(d),(e)). As the initial structures mature by mass accretion, they become increasingly thicker and after approximately 60 minutes streamers engulf the entire pore-space of the device and the length to radius ratio approaches unity. In order to gain more insight into the morphology of a streamer, their imaging at an even higher resolution was attempted using SEM. However, observing these inherently soft, in-situ and fragile systems under SEM presents a tremendous challenge. In spite of these difficulties, a few streamers could be salvaged from the device and successfully imaged using SEM to reveal their microstructure in greater detail. Figure 2.4(f) shows an SEM image of an intact streamer after the microfluidic device was disassembled and allowed to dry. The image sheds light on the structure of the streamer at this resolution for the first time to the best of the author knowledge. It reveals the intimate role of PAM material in holding the structure together through a network of mechanical bonds connecting the PS beads.



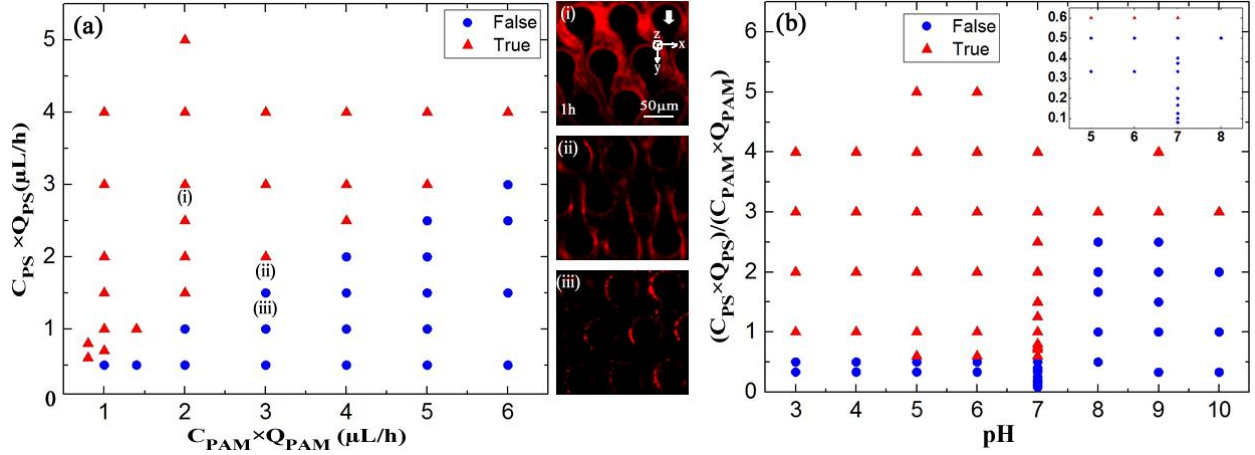
**Figure 2. 5:** (a) Two-color confocal imaging of a streamer after 1 hour of experimentation. White-dashed line indicates the  $y$ -location at which the corresponding  $z$ - $x$  plane is depicted. Image of the same location using (b) FITC Green filter cube and (c) Texas Red filter cube.

Figure 2.5(a) shows a two-color superimposed confocal image of the streamer after approximately 60 mins of experimentation. The fluorescein mixed PAM appears green, while the PS beads appear red. It can be seen that the PAM solution is well mixed everywhere, but PS beads localize around the pillars (Figure 2.5(b),(c)). These experiments were complemented by two control experiments. In the first case only PAM solution was flown through the device and in the second only PS solution was flown through the device. In neither case streamer formation was observed, thus confirming that the combined flow of both PAM and PS was required for streamer formation (Figure 2.6).



**Figure 2. 6:** Control experiments for the investigation of streamer formation confirms that streamer forms for the combined flow of PAM (0.2% w/w) and PS (0.8%w/w) solution only.

Streamer formation can be expected to dependent on the mass fluxes of both PS and PAM solution. In order to probe this dependence, we carried out extensive experiments by varying the mass fluxes of both PS and PAM to draw a streamer formation state diagram, first at pH neutral conditions Figure 2.7(a). The experiments were evaluated in a binary fashion, where outcomes were divided into two bins – one where streamers formed and another where they did not form. In the state diagram Figure 2.7(a), red triangle and blue circle are used as binary markers for streamer formation and its lack of respectively. We find that streamer formation event occurs only when the mass flux of PS is approximately equal to or greater than mass flux of PAM. Stating this more quantitatively, streamer formation occurs when  $C_{PS}Q_{PS} \geq 0.6C_{PAM}Q_{PAM}$ .



**Figure 2. 7:** (a) Formation state diagram of streamer formation over different flow rates  $Q_{PAM}$ ,  $Q_{PS}$  and concentration  $C_{PAM}$ ,  $C_{PS}$ . Red triangle represents true streamer formation and blue circle indicates no streamer formation. The side-bars depict the optical microscope observations at the three located delineated in the formation plot: (i) Streamer formation after one hour for  $C_{PAM} \times Q_{PAM} = 2 \mu\text{L/h}$ ,  $C_{PS} \times Q_{PS} = 3 \mu\text{L/h}$ ; (ii) Streamer formation at phase boundary for  $C_{PAM} \times Q_{PAM} = 3 \mu\text{L/h}$ ,  $C_{PS} \times Q_{PS} = 2 \mu\text{L/h}$ ; (iii) No streamer formation after one hour for  $C_{PAM} \times Q_{PAM} = 3 \mu\text{L/h}$ ,  $C_{PS} \times Q_{PS} = 1.5 \mu\text{L/h}$ . (b) State diagram of streamer formation at various pH values and ratios of  $(C_{PS} Q_{PS}) / (C_{PAM} Q_{PAM})$ .

These streamers are remarkably stable and eventually form mature streamers. On the contrary, the system is marked by absence of streamers for  $C_{PS} Q_{PS} < 0.6 C_{PAM} Q_{PAM}$ , even after a maximum observation time-scale of 60 minutes. The condition  $C_{PS} Q_{PS} \approx 0.6 C_{PAM} Q_{PAM}$  represents the state boundary. Thus sufficient amount of PS bead supply must be maintained for stable streamers. Up until now, our experiments were in pH neutral solutions. We expanded our investigation to create another streamer formation state diagram where the ratio of mass flow rate of PS beads and PAM solution with pH maps the streamer formation. For this formation state plot (Figure 2.7(b); Figure 2.8), we find that acidic and neutral pH of PS bead solution (PAM solution pH not altered), streamer formation always occurs for  $(C_{PS} Q_{PS}) / (C_{PAM} Q_{PAM}) \geq 0.6$ . However, for basic pH solution, streamer formation only occurs for  $(C_{PS} Q_{PS}) / (C_{PAM} Q_{PAM}) \geq 3$ .

Thus, it appears that for basic PS bead solutions a higher concentration of PS beads is required for a successful streamer formation.

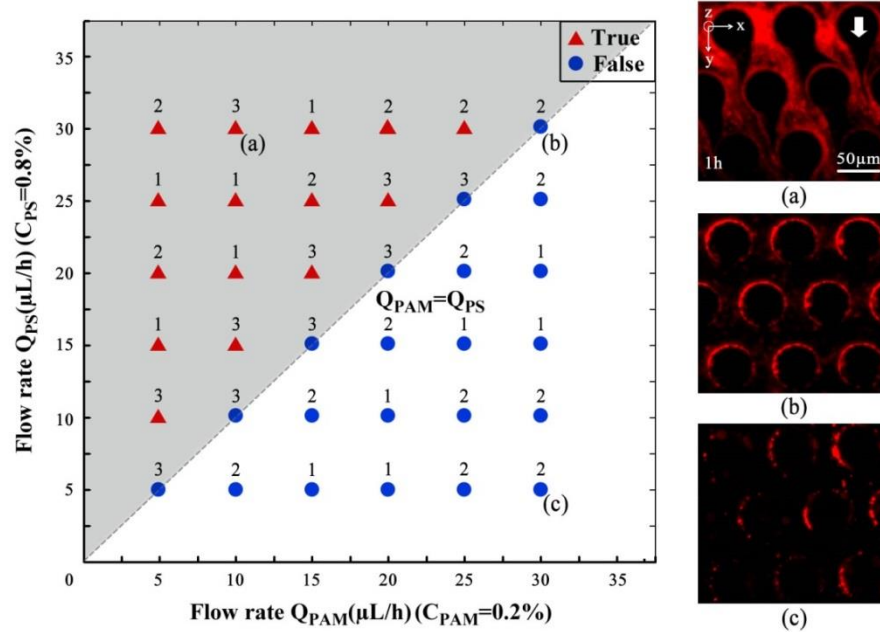


**Figure 2. 8:** Repeat experiments for the phase diagram of streamer formation by varying flow rates when the concentration is fixed for  $Q_{PAM}$  and  $Q_{PS}$ . Red triangle represents true streamer formation and blue circle indicates no streamer formation. Each number represents repeatability. (a) Streamer formation after 1h for  $Q_{PAM}=10\mu\text{L/h}$ ,  $Q_{PS}=30\mu\text{L/h}$ . (b) Transition phase for  $Q_{PAM}=Q_{PS}=30\mu\text{L/h}$ . (c) No streamer formation after 1h for  $Q_{PAM}=30\mu\text{L/h}$ ,  $Q_{PS}=25\mu\text{L/h}$ . (d) Streamer formation (different morphology) after 1h for  $Q_{PAM}=5\mu\text{L/h}$ ,  $Q_{PS}=20\mu\text{L/h}$ . (e) Transition phase for  $Q_{PAM}=Q_{PS}=15\mu\text{L/h}$ . (f) No streamer formation after 1h for  $Q_{PAM}=30\mu\text{L/h}$ ,  $Q_{PS}=5\mu\text{L/h}$ .

## 2.4 Discussion

The experiments conducted in this study reveal distinct slender structure formation in colloidal flows through microfluidic channels. This process critically depends on three intersecting physical phenomena – the viscoelasticity of the fluid, bead induced aggregation and finally the flow itself. We have found that the absence any of these for this system prevents streamer

formation. There exists an interesting parallel of this phenomenon: in bacterial suspensions subject to hydrodynamic flow, slender filamentous aggregates primarily comprising of bacterial cells encased in matrix of self-secreted extra-cellular polymeric substances (EPS) have been observed<sup>166</sup>. Experiments from our own research group have shown that EPS viscoelasticity is critical for bacterial streamer formation as it allows the bacterial cells to aggregate<sup>130, 166, 168</sup>.

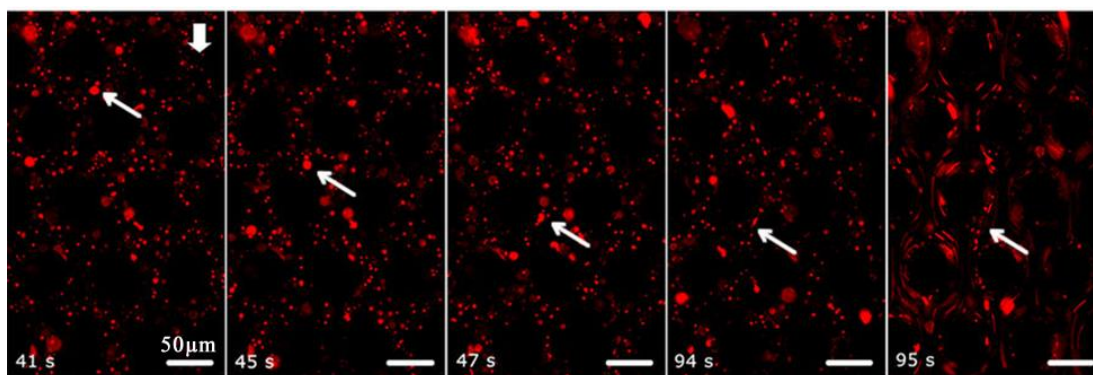


**Figure 2. 9:** Time lapse imaging of a bacterial floc attaching to a pillar wall and undergoing a large elastic deformation by fluidic loading to form a bacterial streamer. Figure is adapted from Hassanpourfard et al.<sup>72</sup>.

In order to pin down the mechanism of abiotic streamer formation, we take cues from imaging reports as well as our previous experiments on biological analog. In these biological experiments, flocculation has been shown to be one route to rapid bacterial streamer formation<sup>130</sup>. In those experiments, we observed that the flocs which are soft aggregates of EPS covered bacteria adhere quickly to the micro pillars once flown inside the device and thereafter undergo severe shearing by the background flow (Figure 2.9). Thus the EPS served the dual role of aiding the formation of a soft composite structure made up of EPS covered bacteria as well as providing the compliance necessary for shearing action. In our current experiments, an SEM image of the streamer clearly shows evidence of viscoelastic filaments connecting PS beads acting as compliant mechanical bonds, Figure 2.4(f). Since original PS beads were only in water

where no flocculation was observed, we hypothesize that an intermediate floc like state exists before the combined flow enters pillar array consisting of PAM covered beads. Then the viscoelastic PAM serves the dual purpose of floc formation and compliance. This assertion is supported by Otsubo and Watanabe<sup>174</sup> who reported bridging and subsequent flocculation by PAM in silica suspensions and found that the resulting flocs had a pseudo-plastic rheology. Bridging flocculation occurs when the polymer chain is long enough to be adsorbed to multiple beads<sup>175</sup>.

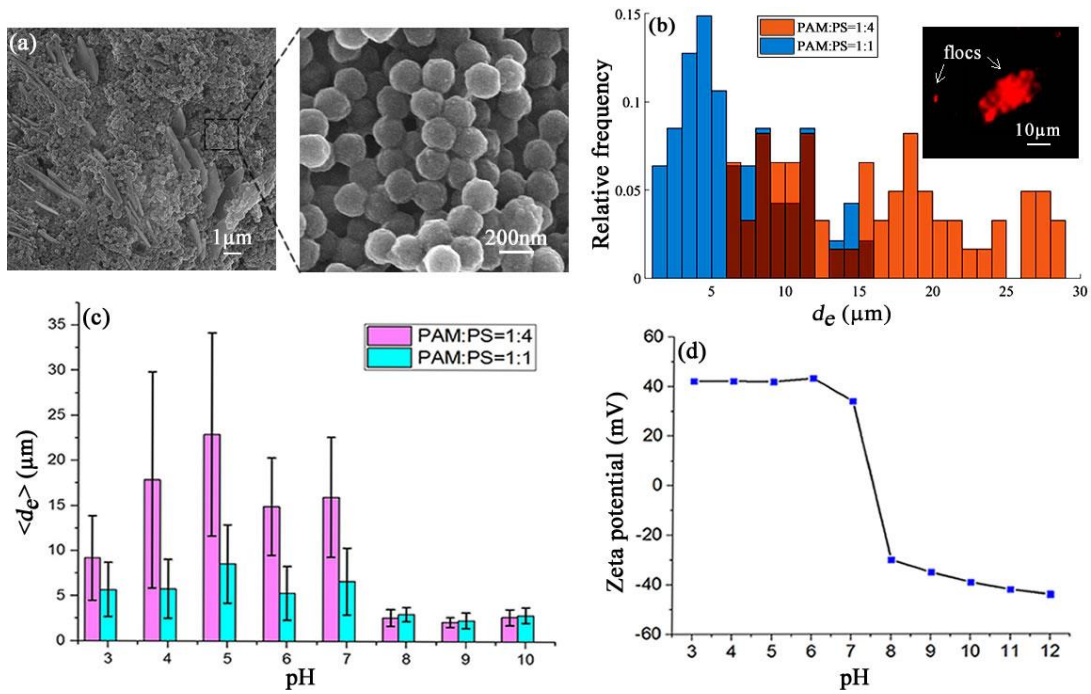


**Figure 2. 10:** (a) SEM image of a floc formed under quiescent conditions. The SEM imaging was done for a volume ratio (PAM:PS) of 1:4 at pH 5. (b) Normalized frequency histogram of the equivalent diameter ( $d_e$ ) of flocs. For a volume ratio (PAM: PS) of 1:4 the mean is approximately 16  $\mu\text{m}$  (of 61 data points) and for a volume ratio of 1:1, the mean is approximately 7  $\mu\text{m}$  (of 47 data points). The inset shows the optical microscope image of flocs. (c) The average equivalent diameter of flocs ( $\langle d_e \rangle$ ) as a function of pH for two different mixing ratios of PAM and PS solutions. (d) Zeta potential as a function of pH for PS bead solutions (0.2% w/w).

In order to assess our hypothesis, we investigated PS bead flocculation under quiescent conditions. We found that indeed PS beads flocculated and Figure 2.10(a) shows an SEM image of such a floc. In the blown out section, we can observe that PS beads, which are otherwise smooth and spherical, appear to be laced with PAM (roughened surfaces). These flocs were also observed through optical microscopy and using image analysis an equivalent diameter of these flocs ( $d_e$ ) was determined. The distributions of floc size are presented in Figure 2.10(b) with accompanying optical image of flocs. These experiments were repeated for two different volume ratios of PAM and PS beads (neutral pH) – PAM:PS=1:4,1:1. These experiments showed that higher relative concentration of PS beads favor larger flocs. The equivalent mean diameters of flocs  $d_e$ , for these concentrations were approximately 16  $\mu\text{m}$  and 6.65  $\mu\text{m}$  respectively. Furthering this line of enquiry, we calculated the floc size distribution for different pH values of PS bead solution and the mean values of the equivalent floc diameter  $\langle d_e \rangle$  is presented as a bar plot in Figure 2.10(c). We see that for  $\text{pH} < 7$ , the floc size distribution remains fairly similar to the floc size distribution at  $\text{pH}=7$ . However, for basic PS solutions the floc size decreases significantly for both lower and higher concentration of PS beads. This severe contrast may have electrostatic origins. To probe deeper, we carry out zeta potential measurements of the PS beads as a function of the pH of suspending media, Figure 2.10(d). This figure shows that the isoelectric point of the PS bead solution is approximately at  $\text{pH} 7.5$  and around the isoelectric point the zeta potential abruptly changes sign, although the magnitude remains more or less constant for acidic and basic solutions. Thus the change in polarity of the electrical double layer (EDL) seems to reduce the attractive forces contributing to the flocculation phenomena. Aggregation in ex situ (flocculation in quiescent conditions) and in situ (microfluidic study) experiments can be expected to be different (Figure 2.10). However, we see that there exists a

strong correlation between the floc size in quiescent conditions and the predicted outcomes of a floc-mediated model for the current experiments. For instance, Figure 2.10(b) suggests that PS bead concentration is a significant factor on flocculation characteristics so that higher concentration favors larger flocs. Hence, a floc-mediated mechanism would imply the necessity of relatively higher mass flow rate of PS beads with respect to PAM solution for successful formation of streamers. This is confirmed by our streamer-formation state plot, Figure 2.7(a), where successful streamer formation events are mapped for PAM and PS mass flow rates at neutral pH conditions. More interestingly, our flocculation characterizations (Figure 2.10(c)) also indicate that in basic solutions, the floc sizes are much smaller than for their acidic counterparts. Hence, a floc-mediated mechanism would predict that the successful formation of streamers in the basic regime would require a higher flow rate of PS beads. It would also imply that the threshold for streamer formation would show a strong saturating characteristic with pH reflecting the underlying flocculation trends. These predictions are borne out in our second state-plot (Figure 2.7b). We clearly see that a transition to basic pH certainly increases the necessary mass flow rate of PS beads but it does not continue to increase with an increase in pH, saturating immediately as predicted in our floc-mediated hypothesis. It is also worth pointing out that the Weissenberg numbers ( $Wi$ ) at which successful streamer formation was observed are typically greater than unity. This shows that flows in our device are strongly extensional in nature<sup>176</sup>.

## 2.5 Conclusions

In this chapter, we have carried out experiments on flow-induced aggregation of PS beads in a microfluidic device. We observed flow-induced localization of PS beads in the form of string-like slender structures called streamers. For neutral pH conditions, we found that streamers

formed when the mass flow rate of the PS solution was equal to or greater than 0.6 times that of the PAM solution. The detailed flow regimes under which streamer formation is observed were quantified through state diagrams. We proposed a floc-mediated streamer formation mechanism inspired topically by similar structures in bacteria laden flow in microporous media. Our premise is well supported by inferences from our experiments. Although the exact mechanism for floc formation itself has not been revealed by the study, our zeta potential measurements strongly underline the significance of electrostatic effects in governing this phenomenon. Further quantification is challenging due to a number of intricate and often interacting transport phenomena characteristic of particle-laden complex colloidal flows<sup>177</sup>. Although beyond the scope of the current chapter, this would be a natural step towards further investigation of this system.

# Chapter 3

## Investigating fouling at the pore-scale using a microfluidic membrane mimic (MMM) filtration system §

---

§ The materials of this chapter has been published in “N. Debnath, A. Kumar, T. Thundat and M. Sadrzadeh, “Investigating fouling at the pore-scale using a microfluidic membrane mimic filtration system”, Scientific reports, Vol. 9, I. 1, p. 10587, 2019.”

### 3.1 Introduction

Membrane filtration processes, such as microfiltration (MF) and ultrafiltration (UF), have been widely used across a broad range of industries including wastewater treatment<sup>178</sup>, effluent treatment<sup>179</sup>, removal of pharmaceuticals<sup>180</sup>, food processing<sup>181</sup>, and production of reusable and potable water<sup>182,183,184</sup>. Fouling of membranes represents a singular issue and limiting condition in the deployment of membrane-based filtration systems<sup>135</sup>. Fouling generally occurs by the attachment of the water constituents on the surface or within the pores of the membrane, resulting in dramatic reduction in flux over time<sup>9</sup>. The fouling propensity depends on the hydrodynamics (flux, pressure and flow velocity), feed solution properties (foulant types, concentration, pH, and ionic strength), surface interactions (surface charge and polarity) and membrane morphology (pore size and shape)<sup>108, 185</sup>.

Membrane fouling has been intensely studied<sup>9, 186, 187</sup> and various mechanisms of membrane fouling have been identified. Amongst the various mechanisms, cake layer/gel formation<sup>136, 137, 188</sup> and pore blocking<sup>139, 189</sup> are usually regarded as the major fouling mechanisms; cake-layer formation occurs at the upstream end of the membrane, while pore blocking occurs at the pore-scale of the membrane<sup>140, 190, 191</sup>. A common method to investigate the fouling mechanism is to evaluate the flux decline over filtration time. The various mechanisms of membrane fouling exhibit a signature decline of flux with time<sup>22,193</sup>. *Ex-situ* fouling tests provide valuable insight into the effect of different parameters on fouling; however, the evolution of fouling on the surface and within the pores cannot be studied.

Recently, a large number of studies has been devoted to elucidating the transport of particle-laden flow in a porous media<sup>89, 119, 185, 186, 194</sup>. In this regard, microfluidic mimics of membranes have become an important experimental platform for investigating fouling at the pore-

scale<sup>185,119,89</sup>. Specifically, photolithography can be easily adapted to designing microfluidic membrane mimic (MMM) systems with a pore length-scale comparable to the pore size of MF membranes<sup>26, 185, 195</sup>. MMM systems have a significant advantage in that they allow for an easy integration with various sensing platforms, such as optical microscopy. This allows for an *in-situ* and real-time visualization of various fouling processes operative at the pore-scale. This alleviates the challenge faced with a large-scale membrane filtration system, where typically only end-point visualization is possible. Thus, MMM system enables investigating the effect of hydrodynamic conditions (initial flux and pressure) on fouling and analyzing the physiochemical interactions responsible for fouling phenomena at pore scale<sup>90,111</sup>. Debnath and Sadrzadeh<sup>185</sup> reviewed the use of MMM devices in the context of membrane fouling. The use of MMM devices has shed light on downstream fouling, which refers to the fouling when foulants can pass through the skin layer of denser structure and accumulate at the downstream stagnation corners of the skin layer pores<sup>185</sup>. Sendekie et al. observed accumulation of the polystyrene particles (0.5 $\mu$ m) at the downstream corners of the micro-pillars<sup>110</sup>. Bacchin et al. interpreted this downstream deposition with cluster growth kinetics, where the constructive and destructive cluster-cluster interactions play an important role on the aggregation process in a microchannel<sup>91</sup>. Despite these advantages, the use of MMM devices to understand fouling at the pore-scale has been limited and specifically the issue of downstream fouling needs to be investigated in greater detail.

In this work, a systematic fouling study was conducted using three types of foulants colloidal particles, polymer and a mixture of these two to investigate combined fouling in an MMM system. Our MMM device consists of a staggered arrangement of micro-pillars mimicking an MF membrane pore size. The pore length-scale employed was 2  $\mu$ m, which is one of the smallest

gaps that can be reliably fabricated using the photolithography process. We examine the interplay between hydrodynamics and physiochemical interactions with a direct visualization of the MF process using optical microscopy. Constant-pressure experiments are performed in the dead-end mode using a Microfluidic Flow Control System (MFCS).

## 3.2 Materials & Methods

### *Experimental*

The schematic of the experimental setup is shown in Figure 1(a). For the microfluidic dead-end filtration, a pressure-driven flow was created in the microchannel by using microfluidic flow control system (MFCS) (Fluigent, MA, USA). The feed was connected to the inlet via a flow unit (Fluigent, MA, USA) and permeate was collected from the outlet of the MMM system (Figure 3.1 (a)). The MMM filtration experiments were performed at a constant-pressure difference ( $\Delta P$ ), maintained by the microfluidic pressure controller (MFCS-EZ) (Fluigent, MA, USA). The corresponding volumetric flow rate ( $Q$ ) was measured directly from the flow-rate-control-module software (Fluigent, MA, USA). All experiments were conducted at creeping flow condition ( $Re < 1$ ) with maximum fluid velocity  $v_{max} \sim 6.84 \times 10^{-4}$  m/s, considering the channel hydraulic diameter  $d_h \sim 2.86 \mu\text{m}$ . Three different foulants (polymer, particles and a mixture of polymer and particles) were tested at neutral pH condition. All experiments were performed at room temperature and repeated thrice. The MFCS (Flow unit) was never let to dry & cleaned thrice with ethanol solution before changing any feed sample.

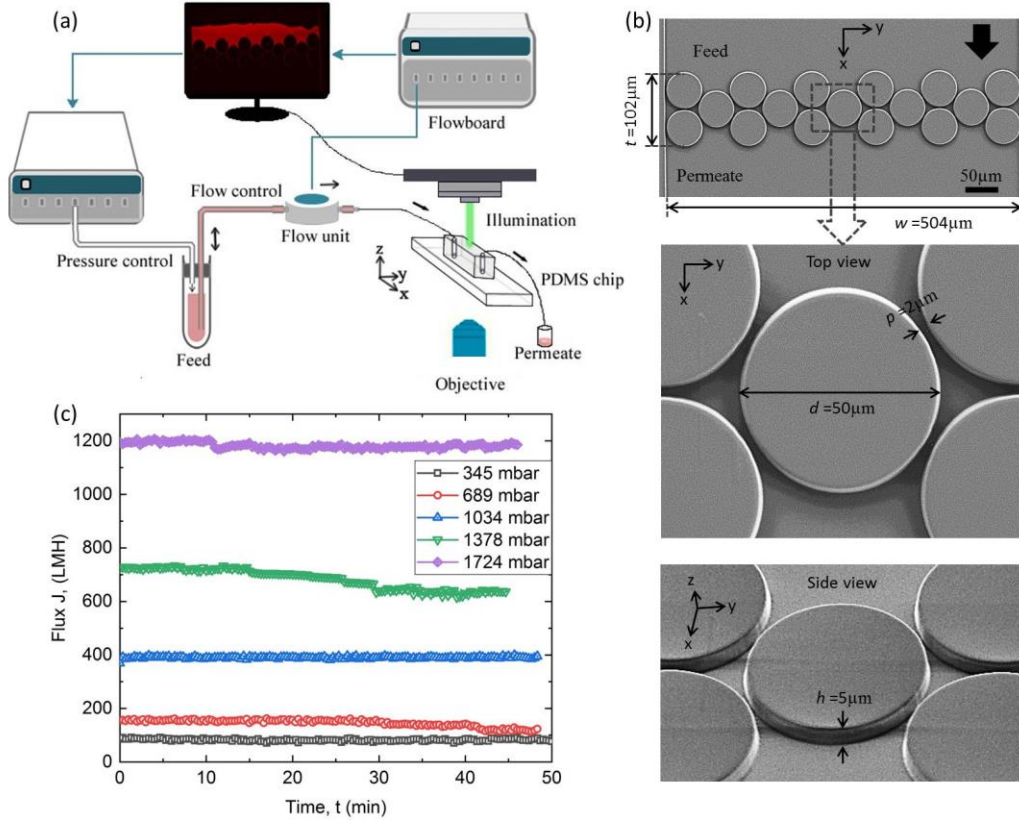


**Figure 3. 1:** (a) A schematic of the experimental setup. A pressure controller and flow-board unit controls the pressure and the flow rate of the membrane mimic microfluidic device, respectively. The pressure difference causes the feed to enter one inlet of the device via the flow unit and the waste is collected from the outlet/permeates side. (b) SEM image of the microfluidic membrane mimic device with dimensions (membrane thickness,  $t = 102 \mu\text{m}$  and membrane width  $w = 504 \mu\text{m}$ ). The blown-out sections show a gap,  $p = 2 \mu\text{m}$ , between any two pillars with diameter  $d = 50 \mu\text{m}$  (top view mode) and a height of  $h = 5 \mu\text{m}$  (side view mode). (c) Control experiments with ultrapure water shows almost constant flux at various pressures for the microfluidic membrane mimic device.

### ***Microfabrication***

The microfluidic device was fabricated by conventional photolithography technique using polydimethylsiloxane (PDMS, Sylgard 184, Dow Corning, NY, USA) with the membrane mimic design. The required membrane design was replicated from a 4" silicon master mold. The

microfluidic design consists of a straight channel with a set of staggered array of pillars near the mid-section (Figure 3.1(b)), which acts as a MF membrane mimic. The staggered arrangement of pillars has a height  $h = 5\mu\text{m}$  and diameter  $d = 50\mu\text{m}$ , and the gap between pillars  $p = 2\mu\text{m}$  (Figure 3.1(b)). Hence, the device provides a pore size which is comparable to an MF membrane pore (0.1-10 $\mu\text{m}$ ). The thickness,  $t$ , of the membrane is 102  $\mu\text{m}$  and the width,  $w$ , of the microchannel is 504 $\mu\text{m}$ , as shown in Figure 3.1(b). The inlet and outlet pores were drilled carefully and the PDMS stamps and coverslip were bonded together by using oxygen plasma-activated bonding at 500mTor pressure for 30 seconds. Next, they were annealed at 80°C for 1 hour to ensure proper bonding. Additional details about the fabrication process is provided elsewhere<sup>196</sup>. The zeta potential of the PDMS surface ( $\xi_{PDMS}$ ) was measured to be  $\sim -45$  mV at pH 7 after plasma treatment (SurPASS<sup>TM</sup> 3, Anton Paar, Graz, Austria).

### ***Microscopy***

The membrane mimic microfluidic device was placed on a stage of an inverted optical (Nikon Eclipse Ti) microscope and fluorescent imaging was performed by using a Texas Red filter cube (Nikon) (Figure 3.1(a)). Fluorescence microscopy technique enabled processing the real-time imaging and videography by using the image-processing module in the Nikon NIS-Element AR software interface. Scanning electron microscopy (SEM) images were taken using a field emission scanning electron microscope (Zeiss, Oberkochen, Germany). Each sample was carbon coated (Denton Vacuum, Desk II, Moorestown, New Jersey) before SEM imaging. Images were taken at 20 kV with an in-lens secondary electron detector (Figure 3.1(b)).

### ***Foulant materials***

Three types of synthetic wastewater solutions were prepared. (1) Polymer solution (PAM 0.2% w/w): polymer solution was prepared by dissolving 1g of anionic polyacrylamide (PAM: A-8354, 22 MDa, Kemira, AB, Canada) into 500mL of DI water. Then the solution was stirred at 600rpm for more than 3hr using a magnet stirrer (Caframo, ON, Canada) to ensure homogeneous mixing. The zeta potential of PAM solution ( $\xi_{PAM}$ ) was measured to be  $\sim -30\text{mV}$  at pH 7 (Malvern Zetasizer). (2) Particle solution (PS 0.2% w/w) was prepared by dissolving 200 nm amine-modified polystyrene beads (excitation at 580 nm, emission at 605nm, Life Technologies, ON, Canada) into Millipore water. Zeta potential measurement showed that PS solution ( $\xi_{PS}$ ) was  $\sim +30\text{mV}$  at pH 7 (Malvern Zetasizer). Red fluorescent PS particles appeared red under fluorescence microscopy. (3) A mixture of polymer and particle solution (PAM+PS (0.2%)=1:4 v/v). Based on our previous study<sup>197</sup>, the optimum ratio of PAM (0.2% w/w) and PS (0.2% w/w) solutions to observe colloidal streamer formation was found to be 1:4 (v/v). This ratio was selected in the present work to investigate the combined colloidal and organic fouling on fouling propensity in the MMM device.

## **3.2 Results & Discussion**

### **3.2.1 Microscopic membrane fouling**

Constant-pressure and constant-flow rate filtration experiments were conducted using the MMM device shown in Figure 3.1(a). All experiments were performed at room temperature and neutral pH. As discussed earlier, our MMM device consists of an array of pillars with height,  $h=5\mu\text{m}$  and pillar gap,  $p=2\mu\text{m}$ , which provides hydraulic diameter of  $2.8\mu\text{m}$  and provides a pore

diameter comparable with the pore size of typical MF membranes (0.1-10 $\mu\text{m}$ ) (Figure 1(b)). Before using the microchips as an MF membrane mimic, control experiments were performed at constant pressure using Millipore water to ensure the integrity of the microfluidic device. Figure 3.1(c) shows that, in the absence of fouling, the water flux was almost constant at different pressures over time. In an MF process, pure water flux varies linearly with pressure. However, from our experimental data, water flux increased non-linearly with increasing pressure (Figure 3.2).

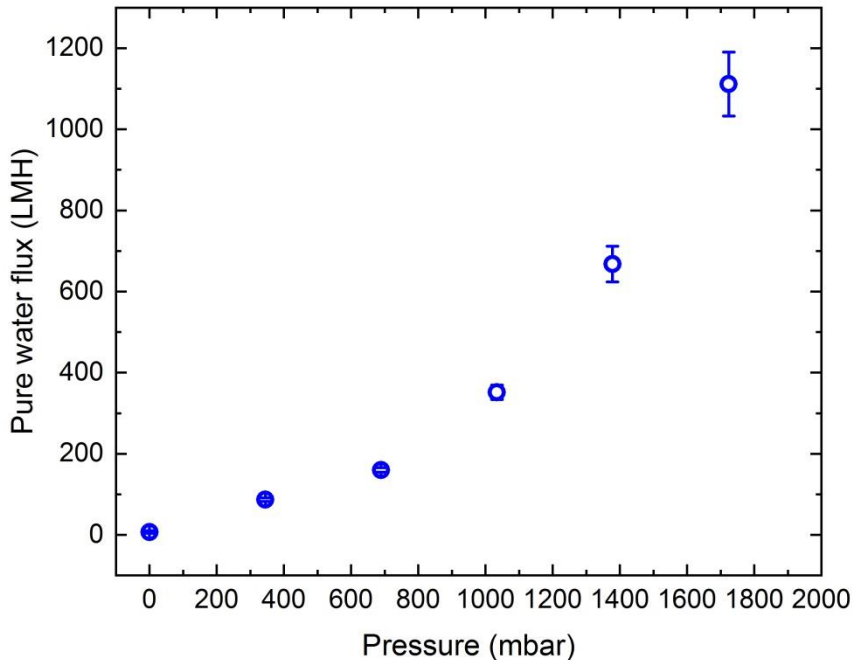


**Figure 3. 2:** Pure water flux as a function of pressure.

Given the pore size of our MMM device ( $\sim 2 \mu\text{m}$ ), we might have exceeded the pressure threshold for filtration. As can be observed in Figure 3.2, our MMM device showed more non-linear behavior at pressures greater than 689 mbar (10 psi). In addition, our MMM device may

not be perfectly sealed at higher pressures. Hence, a constant pure water flux test is performed before starting any experiment. Constant pressure water flux results were repeated and the plot is shown in Figure 3.3.

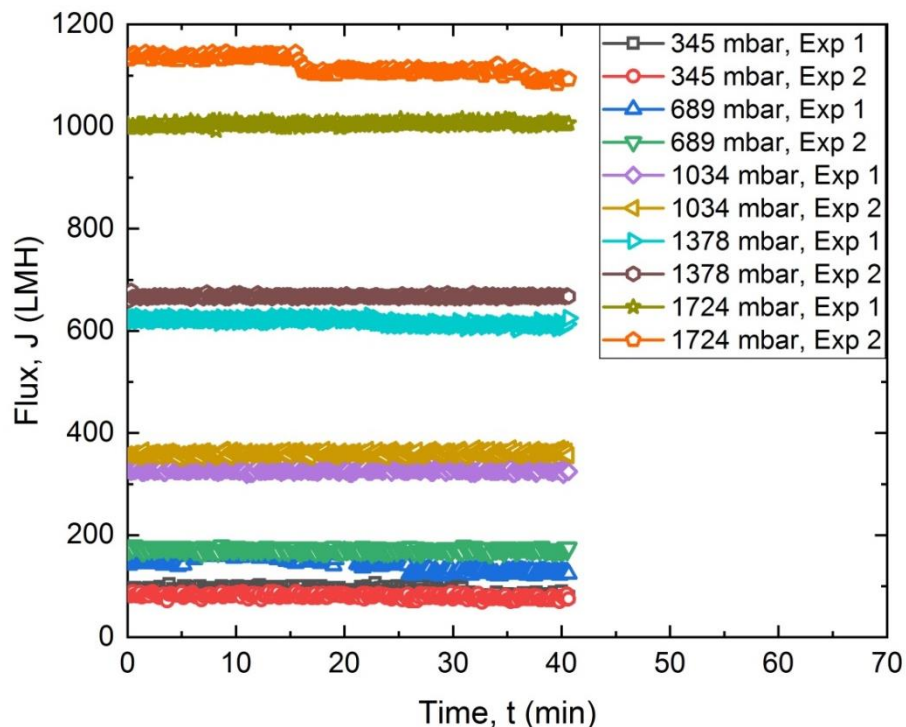


**Figure 3. 3:** Constant pressure repeatability experiments for water at different pressure.

It must be noted that control experiments were conducted before all filtration experiments and constant water flux was achieved each time prior to running the device with water containing foulant materials. Three types of synthetic wastewater solutions were prepared: polymer solution (PAM 0.2% w/w), particle solution (PS 0.2% w/w) and a combined solution (PAM+PS (0.2%)=1:4 v/v). Polymer solution (PAM 0.2% w/w) was prepared by dissolving 1g of anionic polyacrylamide (PAM: A-8354, 22 MDa, Kemira, AB, Canada) into 500mL of DI water. Details about the foulants material preparation are provided in the materials and methods section. In constant-pressure experiments the feed solution is forced through the pillar-array and the foulant

accumulates around the pillars over time. A total of 120 mins of filtration time was considered, unless otherwise stated. This fouling phenomenon caused a decrease in permeate flux for constant-pressure experiments with the three foulants.

Figure 3.4 summarizes the observed fouling under different constant-pressure experiments. At low flow rates or pressures (Figure 3.4(a) & (b)), the foulants started depositing on the surface or within the pores of the pillars. Cake filtration was generally observed for colloidal suspension (PS 0.2% w/w, amine-coated PS bead with 0.2  $\mu\text{m}$  diameter) and pore blocking was observed for the polymer solutions (PAM 0.2% w/w). However, in the case of higher flow rates or pressures (Figure 3.4(c) & (d)), downstream fouling was observed alongside fouling around the pores. The various microscopic observations are useful in elucidating four categories of membrane fouling (a) cake filtration (upstream), (b) pore blocking (inside the pores), (c) colloidal aggregation (downstream) and (d) colloidal streamer (downstream).

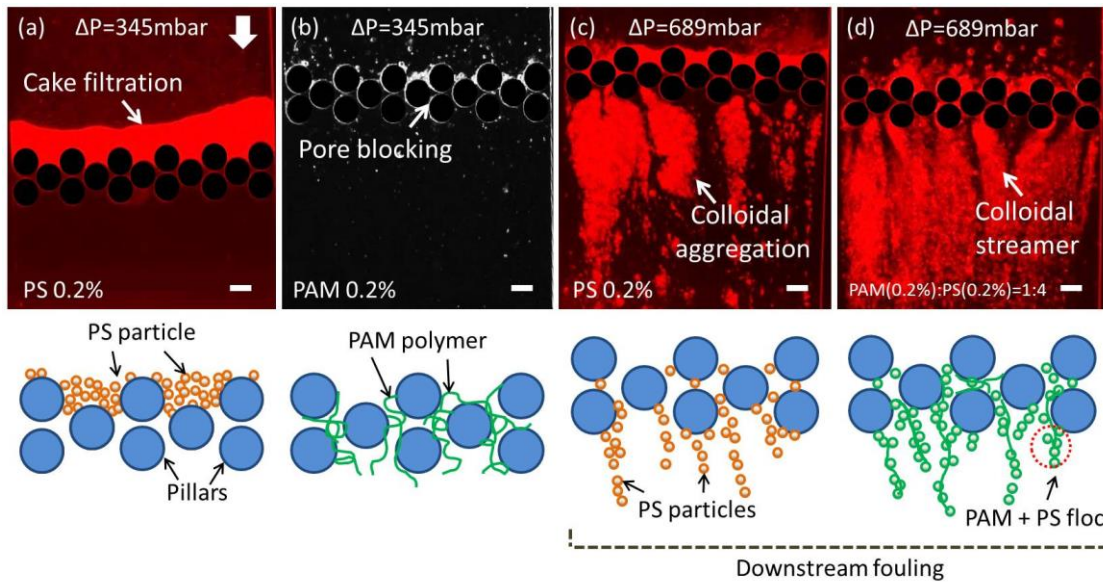


**Figure 3. 4:** Microscopic colloidal fouling phenomena at different locations with their corresponding schematics. (a) cake filtration for PS 0.2% at 345mbar at upstream, (b) pore blocking for PAM 0.2% at 345 mbar at the pillar pores, (c) colloidal aggregation for PS 0.2% at 689mbar and (d) colloidal streamer formation for the combined fouling

(PAM (0.2%):PS(0.2%)=1:4) at 689mbar at downstream. All images are taken at 120 min of filtration and the scale bars are 50 $\mu$ m. Schematics are not to scale.

Figure 3.4(a) depicts the typical low pressure cake filtration (upstream) scenario at 120 min of filtration, wherein the foulant materials accumulate on the upstream end of the membrane<sup>137,136,90,198</sup>. Although, cake filtration usually occurs due to the deposition of particles larger than the pore-scale, Figure 3.4(a) schematic shows that if the foulants are smaller than the pore-scale, then they can aggregate and be packed to form a barrier at the upstream end of the membrane.

Pore blocking is typically more significant under moderate pressures<sup>189,139,109</sup>; when the solutes are forced through the membranes and adsorb onto the membrane pore walls. Pore-blockage (inside the pores) is seen when PAM only solution is flown through the MMM device. The PAM molecules have a radius of gyration,  $R_g=191.9$  nm<sup>197</sup>, and their entanglement can completely block the pores during the course of filtration (Figure 3.4(b)). Fouling due to PAM was imaged under the same conditions, and although the PAM molecule is not red fluorescent, bright and dark areas can be seen under optical microscopy (Figure 3.4(b)). This might be due to higher light scattering from areas which have higher PAM aggregation. Figure 3.4(b) shows that PAM polymer plugged the pores after 120 mins of operation at 345 mbar.

Higher pressure can further force the foulant materials to flow through the membrane pores and reach at the downstream side of the pores. When PS particles reach at the downstream zone of the pillars, they start aggregating along the flow direction as shown in Figure 3.4(c). The colloidal aggregation phenomenon at downstream location<sup>89,110</sup> is observed to occur concurrently with cake filtration and pore blocking (Figure 3.4(c)). Figure 3.4(c) shows such a fouling process

which is accompanied by aggregation of colloidal particles just downstream of the pores which is discussed later.

The colloidal streamer mode of fouling is relatively newly discovered mode of membrane fouling. It was demonstrated recently that in the context of low Reynolds number flows, organic materials such as bacteria can lead to the formation of filamentous structures called ‘streamers’<sup>199</sup>. These filamentous structures can proliferate rapidly in microfluidic devices leading to pervasive colonization and clogging<sup>106, 196</sup> leading up to a catastrophic failure of the device<sup>172, 196</sup>. Due to its very nature these streamers can thrive into various sections of a microfluidic device including the downstream sections of filtration systems<sup>106, 127, 199</sup>. Debnath et al.<sup>197</sup> recently demonstrated that particle laden polymeric flows can also lead to morphologically similar structures as bacterial streamers leading to the generalization of the phenomenon to other colloidal systems. When a mixture like particle laden polymer (PAM(0.2%):PS(0.2%)=1:4) is filtered through our MMM system, a filamentous compliant structure was formed at downstream of the pillars. This structure is called the ‘colloidal streamer’<sup>200</sup>. Figure 3.4 (d) shows colloidal streamer fouling, which is the second kind of downstream fouling captured at 120 min of filtration at 689 mbar pressure. The formation of the colloidal streamer at downstream location is discussed in details later.

### **3.2.2 Constant-pressure filtration**

The effect of constant applied pressure difference on water flux through MMM was studied. The pressure difference across the microfluidic channel was varied from 138 to 1378 mbar. To investigate the effect of colloidal fouling, first only PS 0.2% bead solution was used as feed, and the results are shown in Figure 3.5(a). The flux,  $J$ , is calculated from the direct measurement of

the flow rate obtained by MFCS system using the relationship  $J = Q/(w \times h)$ , where  $Q$  is the flow rate ( $\text{m}^3/\text{s}$ ),  $w$  is the width of the channel ( $504\mu\text{m}$ ), and  $h$  is the height of the pillars ( $5\mu\text{m}$ ).

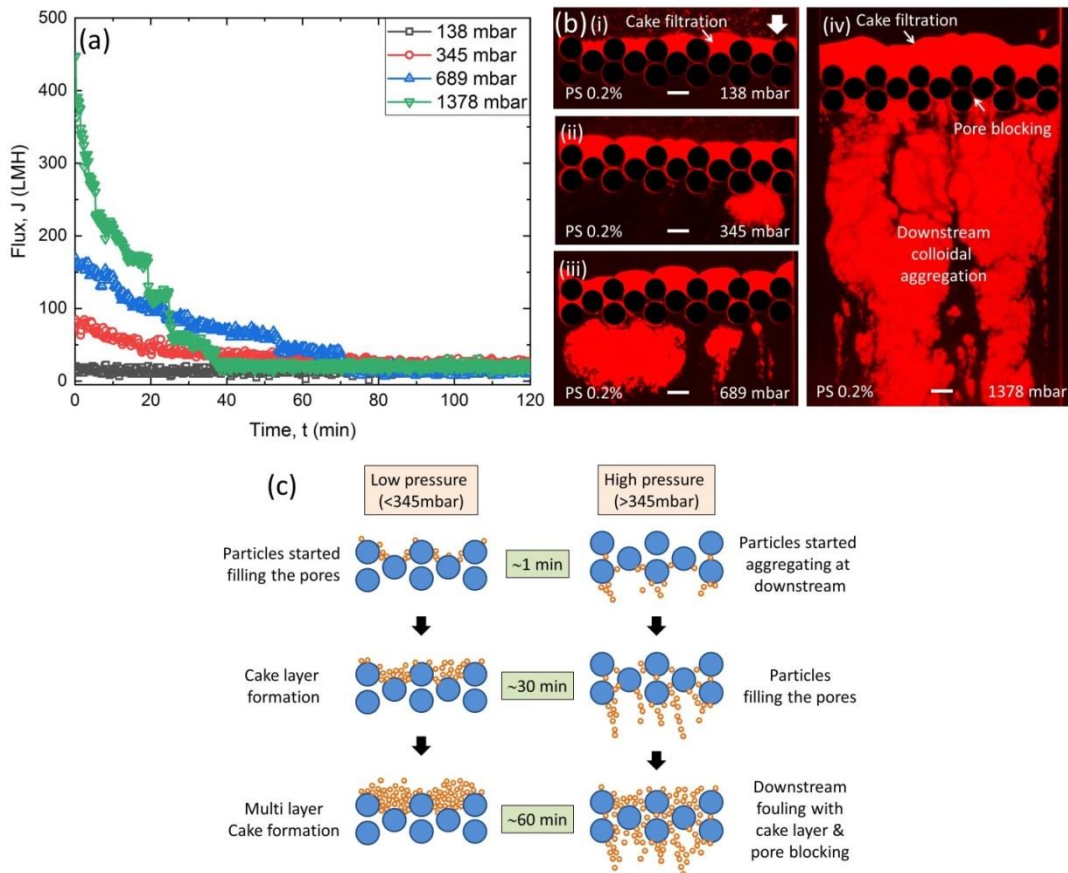


**Figure 3. 5:** (a) Filtration experiments at constant pressure shows decreasing flux for PS 0.2% as fouling progresses with filtration time. (b) Corresponding microfluidic images show end-result of fouling (120 min). At low pressures, fouling is more like cake filtration at upstream (i)-(ii). At higher pressures more colloidal aggregation are observed at downstream with simultaneous pore blocking and cake filtration (iii)-(iv). (c) Schematic of fouling at low pressure (<345mbar) and high pressure (>345mbar) showing the fouling evolution in 60 min.

Figure 3.5(a) shows that at 138 mbar the flux is almost constant. Hence, 138 mbar can be considered as a limiting pressure/critical pressure below which fouling does not occur for PS 0.2% solution. In membrane filtration, the critical flux is defined as the permeate flux above

which the irreversible membrane fouling occurs<sup>145, 201</sup>. The approximate critical flux for our MMM system is,  $J_{cr} \sim 24.62$  LMH, calculated as,  $J_{cr} = Q_{cr}/(w \times h)$ , where  $Q_{cr} = 1.72 \times 10^{-14}$  m<sup>3</sup>/s.

In general, larger particles than the pore size of membrane are blocked on the membrane surface during filtration and form a cake layer<sup>202</sup>. However, smaller particles than membrane pore size can also form a cake layer, when inception of fouling occurs inside the pores and grows to the filter cake on the membrane surface as the membrane pores become narrower over time<sup>202</sup>. From our direct microfluidic observations, low pressures ( $\leq 345$  mbar) caused pore blocking at the surface of the pores first and developed to a filter cake (Figure 3.5(b) (i) & (ii)) with time. Figure 3.5 (b) captures filtration fouling with PS 0.2% for filtering over 120 min. This kind of fouling is also in good agreement with *ex-situ* MF/UF filtration results in the literature<sup>139, 188</sup>. In contrast, higher pressures ( $\geq 689$  mbar) led to higher initial flux ( $\sim 160$  LMH at 689 mbar), but a sharp decline in flux over time, as shown in Figure 3.5(a).

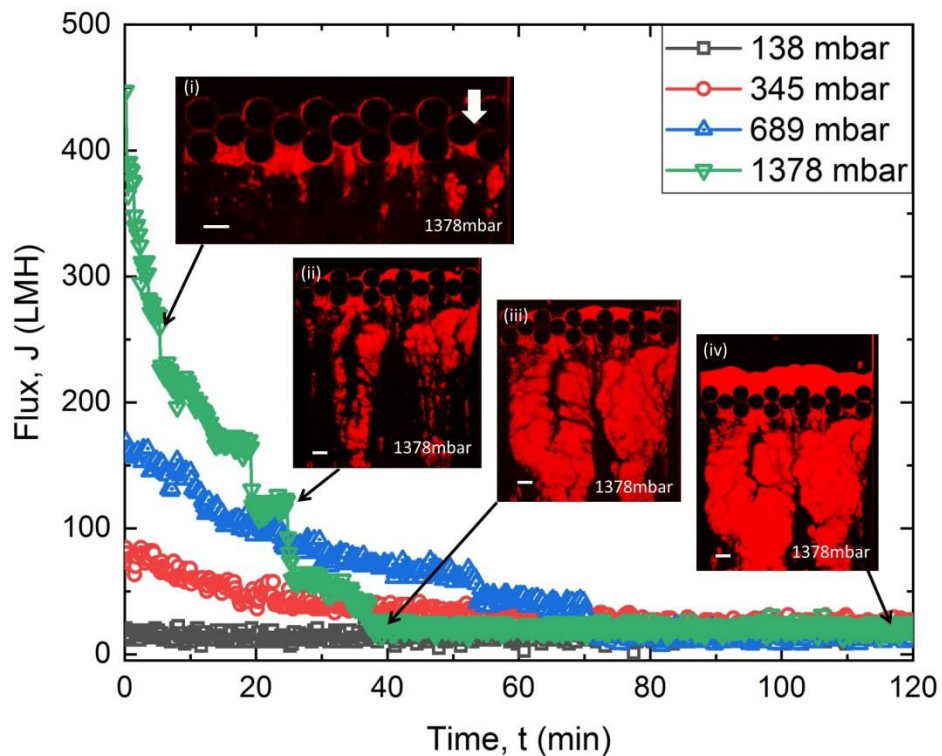


**Figure 3. 6:** Constant pressure experiments at 1378 mbar pressure for the PS 0.2% solution show sharp decline in flux compared to lower pressure. (i) Microfluidic fouling started with colloidal aggregation at downstream. (ii)-(iii) Downstream colloidal aggregation fouling continued with partial pore fouling and filter cake till 40 min of filtration. (iv) A significant increase in cake layer thickness is observed till 120min of filtration.

At higher pressures, the larger hydrodynamic drag force caused the particles to pass through the pores of pillars and aggregate at the downstream zone of pillars (Figure 3.5(b) (iii) & (iv)). This type of fouling may occur in the finger-like macrovoids of porous membranes, underneath the top skin layer, when filtered particles diameter is less than the pores of skin layer. It was observed from the online monitoring of the fouling at 1378mbar (Figure 3.6) that the fouling started with the colloidal aggregation at downstream zone. It continued for 40 min simultaneously with partial pore blocking and cake layer formation (Figure 3.6). After that, downstream colloidal aggregation reached a steady state with an increase in the cake layer thickness (Figure 3.6) for the rest of the filtration process. Figure 3.5(c) shows the schematic of the fouling process at low pressure (<345mbar) and high pressure (>345mbar) with time. It can be seen from the schematic that at low pressure pore blocking causes the cake layer formation while for higher pressure downstream fouling causes the pore blocking and pore blocking leading to cake layer formation eventually. The constant pressure filtration results were repeated in triplicate (Figure 3.7).

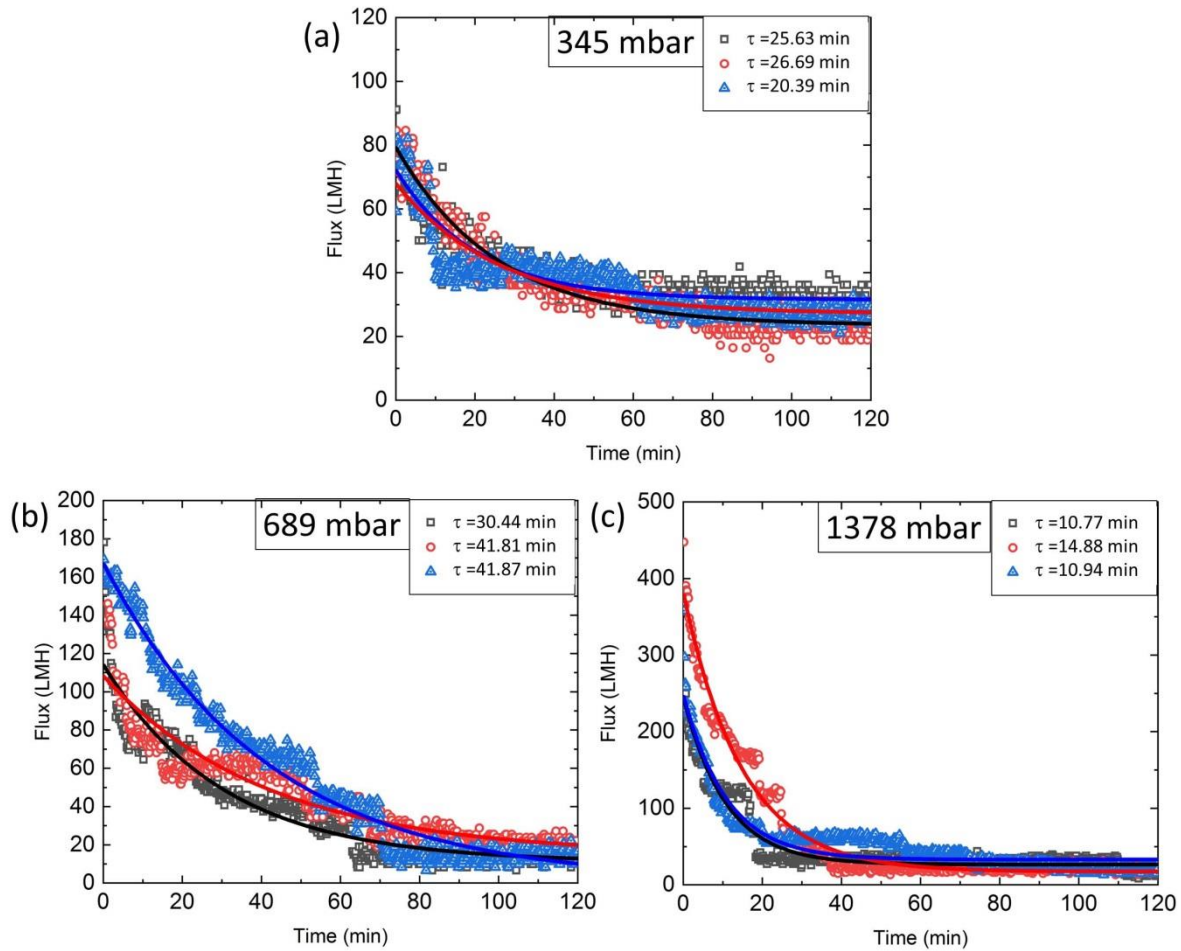


**Figure 3. 7:** Repeatability experiments at different constant pressure with PS 0.2% solution. The repeatability curves are fitted to the same exponential decay equation shown in table 3.1.

At low pressures, we hypothesise that the particles mostly attach to the upstream surface of the pillars as the hydrodynamic drag force could not overcome the attractive surface interaction between particle-PDMS wall (Figure 3.5(b) (i) & (ii)). The zeta potential measurement showed a strong attractive electrostatic force exists between positively charged PS particles ( $\zeta_{PS} \sim +30\text{mV}$  at pH 7) and negatively charged PDMS surface ( $\zeta_{PDMS} \sim -45\text{mV}$  at pH 7). As a result, cake filtration is generally exhibited at low pressures ( $\leq 345\text{mbar}$ ). However, at higher pressures ( $\geq 689\text{mbar}$ ), hydrodynamic drag force might overcome the interaction energy between particles

and particle-PDMS surface. Higher shear stresses and advection rates lead to particle aggregation downstream of the pillars (Figure 3.5(b) (iii)). At 1378mbar pressure, the inception of fouling occurred at downstream location (Figure 3.6). The downstream colloidal aggregation continued with partial filling of the pore space. When the particles started filling the pores, flow distribution was no longer uniform across the membrane width due to the constricted pore space. Hence, the local velocity of water increased for partially open pores to maintain a constant pressure difference. The increase in the local velocity caused primary and secondary water channel formation by continuous aggregation/sloughing of particles more towards the flow directions<sup>203</sup>. Hence, as filtration proceeded, the detachment of the particles occurred by sloughing and the higher pressure difference eventually resulted in the steady colloidal aggregation at downstream with pore blocking and cake layer after 120 min of filtration (Figure 3.5(b) (iii) & (iv)).

We have also conducted constant pressure (689 mbar) experiments to examine the effects of changing PS concentrations (PS 0.02%, 0.4% and PS 1%) on fouling propensity. As can be observed in Figure 3.8, all of these experiments had led to downstream fouling. Our experiments indicate that the qualitative nature of fouling does not change due to change in concentrations but the same fouling behaviour seems to occur faster at the higher concentrations.

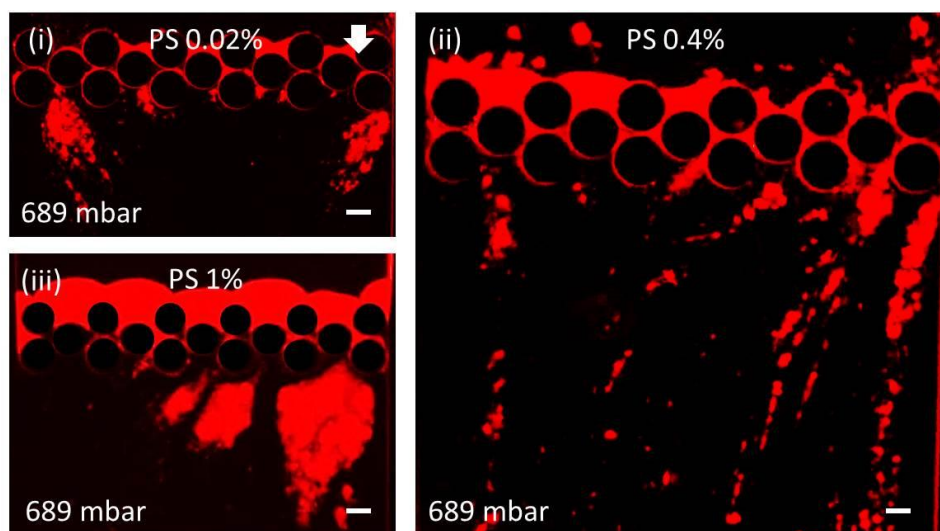


**Figure 3. 8:** Constant pressure fouling scenarios of PS at 689mbar pressure for different concentrations (i) PS 0.02% (ii) PS 0.4% and (iii) PS 1% after 60 min of filtration.

To further investigate the effects of physiochemical interactions on fouling, we have extended our experiments to three different types of foulants at the same constant pressure. The constant pressure experiments were conducted using particle solution (PS 0.2%), polymer solution (PAM 0.2%) and a mixture of PAM(0.2%):PS(0.2%)=1:4 (v/v) to investigate colloidal, organic and combined fouling, respectively. Microfluidic filtration at low pressures did not show significant difference in permeate flux for all types of fouling, whereas, at a pressure of 689 mbar, the decline was found to be more severe for the case of combined fouling than the individual organic and colloidal fouling (Figure 3.9(a)). Starting with same initial flux (~160 LMH), the approximate filtration time for the permeate flux to become steady were 20, 40, and 60 min for the combined fouling, organic fouling, and colloidal fouling, respectively (Figure 3.9(a)). Such a severe flux decline in the case of combined fouling was also observed in ex-situ membrane processes<sup>144,204</sup>. It was found that PS 0.2% resulted in colloidal aggregation at downstream with partial pore blocking and cake filtration (Figure 3.9b (i)) and PAM 0.2% mostly caused pore

blocking (Figure 3.9(b) (ii)). When a combination of PAM and PS were injected as feed (PAM(0.2%):PS(0.2%)=1:4), slender filamentous structures were formed around the pillars and at downstream of the pillars (Figure 3.9(b) (iii)). Debnath et. al<sup>185</sup> named this structure as ‘colloidal streamer’ and this occurs due to synergistic effect resulting from a bridging of PS beads by the polymeric molecules and subsequent adhesion and shearing due to hydrodynamic forces<sup>205</sup>. The attraction between positive PS ( $\zeta_{PS} \sim +30\text{mV}$  at pH 7) and negative PAM molecules ( $\zeta_{PAM} \sim -30\text{mV}$  at pH 7), and the negative PDMS surface ( $\zeta_{PDMS} \sim -45\text{mV}$  at pH 7) caused PAM+PS floc formation and attachment to the surface leading to the streamer fouling at downstream. The dynamics of colloidal streamers is discussed elsewhere<sup>185,203</sup> and here we focus only on the fouling characteristics of streamers. At 689mbar pressure, colloidal streamer formation was observed instantaneously. With time, the streamer accumulated more mass, became thicker and extended up to  $\sim 500\mu\text{m}$  from the pillar surface towards the flow direction. Interestingly, within 20 min the flux reached the steady state but the streamer fouling continued (Figure 3.9(a)).

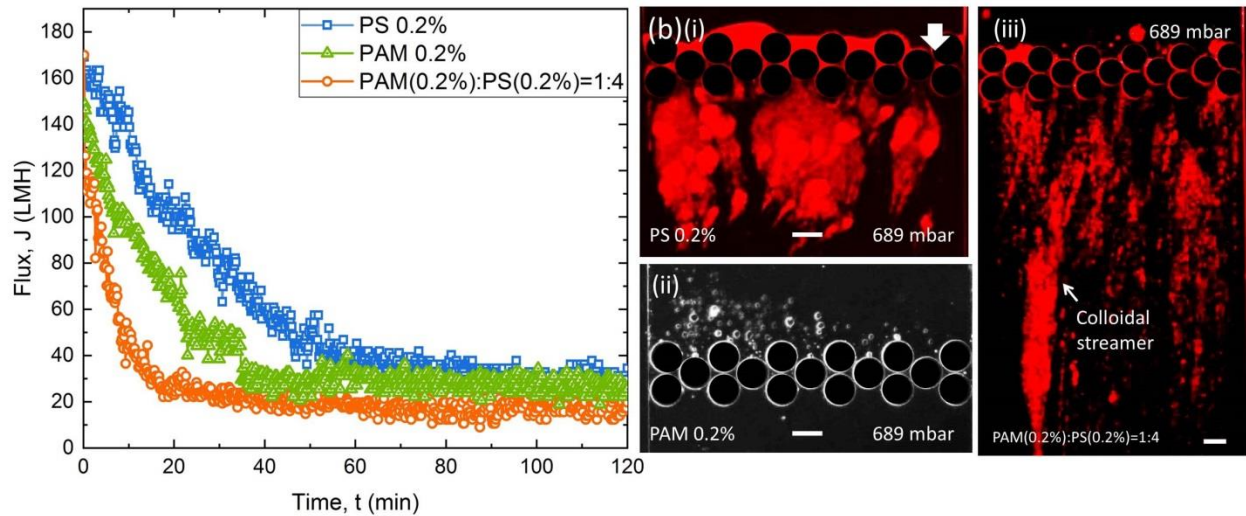


**Figure 3. 9:** Comparison of the constant-pressure fouling behaviour for three types of foulants at the same pressure (689 mbar). (a) Flux vs. time plot showing more severe flux decline for the case of combined fouling (PAM (0.2%):PS (0.2%) =1:4) than individual organic and colloidal fouling (PAM 0.2% & PS 0.2%), (b) corresponding microfluidic images at the end of the filtration process showing (i) Colloidal aggregation at downstream with partial pore blocking and cake filtration for PS filtration, (ii) pore blocking for PAM filtration, and (iii) streamer formation at downstream for the case of combined fouling.

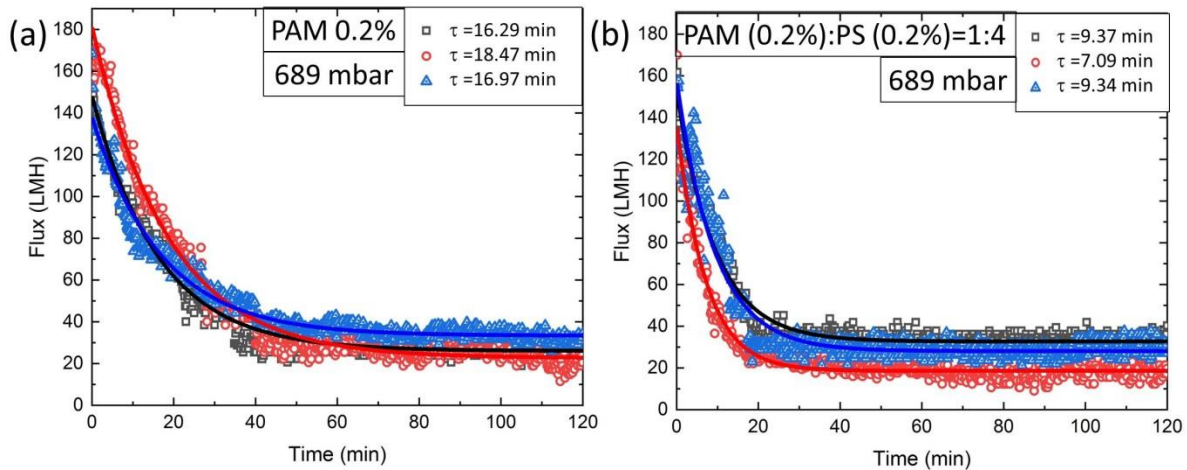


**Figure 3. 10:** Repeatability experiments at constant pressure (689 mbar) for (a) PAM 0.2% solution and (b) downstream colloidal streamer formation with PAM (0.2%):PS (0.2%)=1:4, combined solution filtration.

It was also observed that the process of downstream streamer formation and subsequent streamer breaking were observed continuously during the filtration period<sup>106</sup>. Here, PAM molecules were invisible under red fluorescence microscopy. The constant pressure filtration results were repeated in triplicate (Figure 3.7 and 3.10). When the repeatability data were fitted to the exponential decay equation (Figures 3.7, 3.10 and Table 3.1), the coefficient of determination ( $R^2$ ) values showed better agreement for the case of organic fouling (PAM 0.2%) and combined fouling (PAM 0.2% + PS 0.2%=1:4) than the colloidal fouling (PS 0.2%) for the same pressure (689 mbar) experiments. The analytical modelling of the downstream and streamer types of fouling is the topic of our ongoing research.

**Table 3. 1:** Repeatability data fitted to the exponential decay equation and the corresponding values of the parameters at variable constant pressure difference. The table corresponds to fits shown in Figure 3.7 and 3.10.

$J = A_0 + Ae^{-(t/\tau)}$						
$\Delta P$ (mbar)	Foulants	Legend	$\tau$ (min)	A	$A_0$	$R^2$ (Goodness of fit)
345	PS 0.2%	□	25.63	$5.59 \times 10^4$	$2.34 \times 10^4$	0.93
	PS 0.2%	○	26.69	$4.09 \times 10^4$	$2.70 \times 10^4$	0.80
	PS 0.2%	△	20.39	$4.07 \times 10^4$	$3.14 \times 10^4$	0.88
689	PS 0.2%	□	30.44	$1.03 \times 10^5$	$1.07 \times 10^4$	0.92
	PS 0.2%	○	41.81	$9.38 \times 10^4$	$1.45 \times 10^4$	0.87
	PS 0.2%	△	41.87	$1.67 \times 10^5$	$5.15 \times 10^2$	0.97
1378	PS 0.2%	□	10.77	$2.19 \times 10^5$	$2.63 \times 10^4$	0.89
	PS 0.2%	○	14.88	$3.65 \times 10^5$	$1.71 \times 10^4$	0.98
	PS 0.2%	△	10.94	$2.16 \times 10^5$	$3.27 \times 10^4$	0.88
689	PAM 0.2%	□	16.29	$1.22 \times 10^5$	$2.60 \times 10^4$	0.97
	PAM 0.2%	○	18.47	$1.59 \times 10^5$	$2.26 \times 10^4$	0.98
	PAM 0.2%	△	16.97	$1.04 \times 10^5$	$3.33 \times 10^4$	0.97
689	PAM 0.2%+PS 0.2%	□	9.37	$1.20 \times 10^5$	$3.26 \times 10^4$	0.96
	PAM 0.2%+PS 0.2%	○	7.09	$1.18 \times 10^5$	$1.85 \times 10^4$	0.96
	PAM 0.2%+PS 0.2%	△	9.34	$1.29 \times 10^5$	$2.80 \times 10^4$	0.92

Besides, the primary and secondary water channel formation was more prominent at the end (120min) of filtration (Figure 3.11). An interesting microfluidic phenomenon, water channel formation was observed for constant pressure filtration. When particles started accumulating inside the inner surface of the pillars, as filtration proceeded, floc propagated from blocking the pore space to a filter cake at low constant pressure ( $\leq 345$ mbar). However, at high pressure ( $\geq 689$ mbar), the flow distribution was no longer homogeneous due to the partial blocking of pores. To maintain the constant volume flow conditions or pressure, there remained some fragile flocs or open channels where the local flow velocity was increased. As a result, the increase in velocity prevented complete pore blocking and caused water channel formation. Water channel

formation was observed for the case of bacterial streamer formation earlier<sup>206</sup>. Similar behavior was observed by Lohaus et al. when they performed the numerical simulation with 5 $\mu\text{m}$  PS particles in a microchannel<sup>207</sup> (Figure 3.11 (a)(i) & (ii)). Interestingly, they found particles accumulating on the center-left channel where there was a prominent open channel with no fouling at the right channel (Figure 3.11 (a)(i) & (ii))<sup>207</sup>. However, their observation had no experimental evidence. Figure 3.11 (b) and (c) show water channel formation for colloidal aggregation and streamer formation, respectively. Based on our microfluidic observations, the formation of these water channels were consistent throughout all experiments, especially for the case of downstream fouling at high constant pressures (Figures 3.5(b) (iii) & (iv), 3.6, 3.8, 3.9(b)(i) & (iii)). From Figure 3.11 (b) & (c), primary water channels are in the same direction as flow while secondary water channels are generating from primary. Hence, the formation of primary and secondary water channels not only indicated the particles settling but also they were responsible for the fouling deposition at the downstream side.

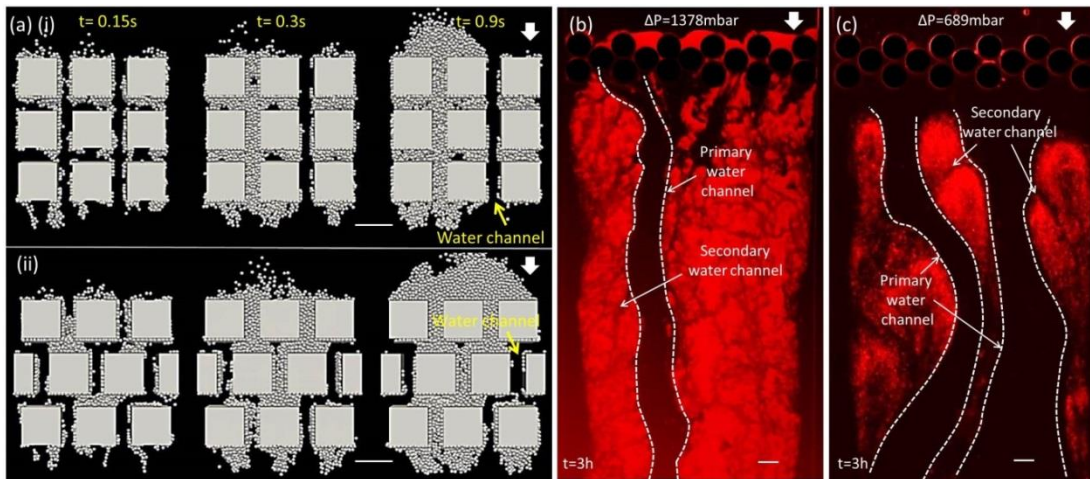


**Figure 3. 11:** (a) Water channel formation observed by Lohaus et al. in numerical simulation for the square connected (i) and staggered (ii) arrangement of pillars<sup>207</sup>. Scale bars are 50 $\mu\text{m}$ . (Copyright 2018, reproduced with permission from Journal of Membrane Science). Water channel formation for (b) colloidal aggregation (PS 0.2%) at

1378mbar pressure and (c) colloidal streamer (PAM (0.2%):PS (0.2%) =1:4) at 689mbar pressure after 180 min of filtration. Primary water channels (marked with white dash line) and secondary water channels are shown with arrows. Scale bars are 50 $\mu$ m.

Different membrane fouling mechanisms are discussed in the literature<sup>193,192</sup>. Ho et al. discussed the combined cake filtration and pore blocking model for protein fouling in a MF system<sup>147</sup>. But the cake filtration and pore blocking model cannot explain the flow/detachment behaviour of particles during fouling process. These can further be explained by comparing different fouling scenarios and examining the fouling percentage which are discussed next.

In order to reveal more information about the governing fouling mechanisms exhibited by different foulants, the experimental constant pressure flux results (689mbar) were fitted to the linear equations derived for constant pressure filtration by Hermia model<sup>192</sup>. Hermia categorised four kinds of fouling: cake filtration, standard pore blocking, intermediate pore blocking and complete pore blocking with the decline in flux<sup>192</sup>. Figure 3.12 shows that our results were more in agreement with the complete pore blocking (Figure 3.12 (d)) for the filtration results with the three foulants at 689 mbar pressure. The microfluidic observations are in consonance with the findings. For PS particles partial cake filtration and pore blocking were observed and hence Figure 3.12(a)-(c) show a less degree of match as compared to Figure 3.12(d). However, for the combined foulant of PAM and PS, we know from our observations that streamer formation occurred downstream of the pillar wall. Interestingly, the fouling due to streamers is also consistent with the time signature of complete pore blocking. This suggests that streamer formation occurs in such a manner that complete pore blocking is achieved simultaneously. However, from the pore-scale perspective, streamer led-clogging is a different kind of fouling as compared to complete pore blocking. This suggests that this is an entirely different fouling

mechanism and needs to be studied in more detail. While, some early work in the area of modelling of streamer-clogging has taken place<sup>172,171</sup>, more extensive modelling work is desirable.

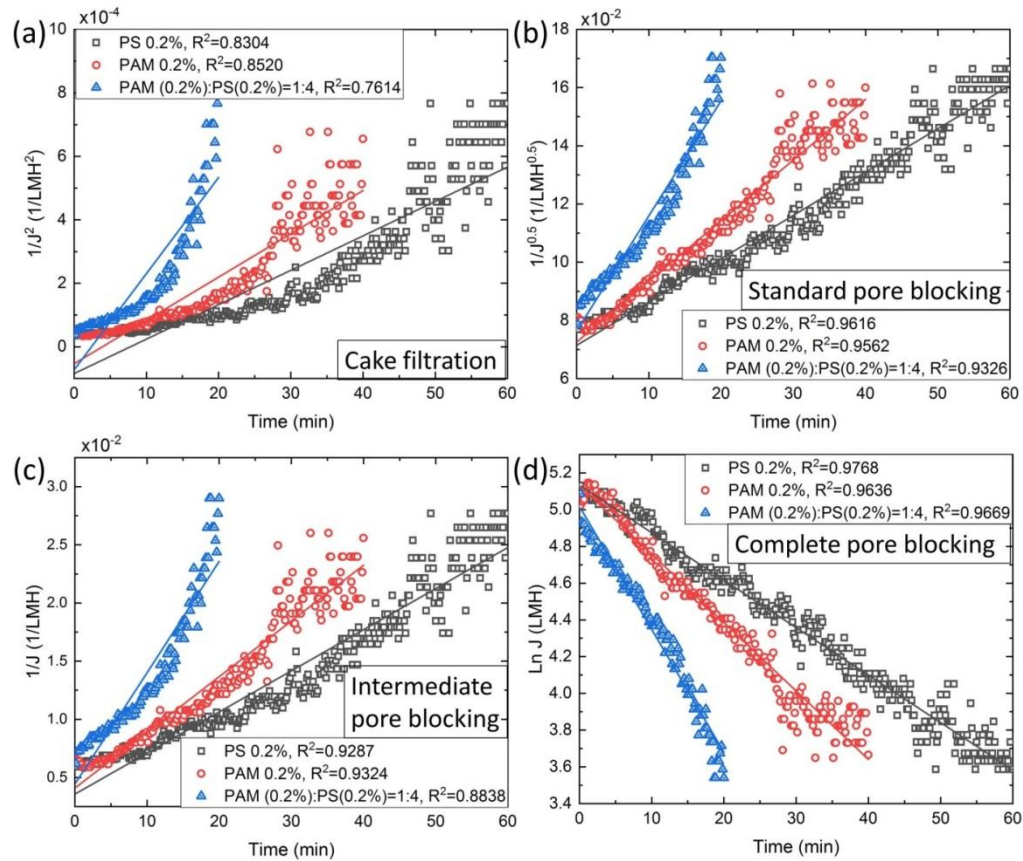


**Figure 3. 12:** Flux vs time plot for the three foulants using Hermia model at constant pressure (689mbar). Curves are fitted using regression analysis where  $R^2$  value represents regression coefficient. The flux trends are compared to Hermia's model for (a) cake filtration, (b) standard pore blocking, (c) intermediate pore blocking, (d) complete pore blocking. From the regression analysis, the maximum value of  $R^2$  indicates that the fouling is complete pore blocking for the three foulants.

To analyze the percentage contributions of the colloidal aggregation and colloidal streamer fouling, flux recovery tests were performed using PS 0.2% and the combined solution (PAM (0.2%) :PS (0.2%) =1:4) (Figure 3.13 (a) & (b)). First, pure water flux was ( $J_{wI}$ ) obtained at

689mbar pressure for 30 min. Next, fouling experiments were conducted at the same pressure for another 30min ( $J_{wf}$ ). A hydraulic washing was then performed for another 30 min to clean the system at a higher pressure (1378mbar) than filtration pressure (689 mbar). Finally, pure water flux ( $J_{w2}$ ) was obtained again at 689mbar (Figure 3.13(a) & (b)). The experimental results show more reversible fouling for colloidal aggregation; more irreversible fouling for colloidal streamer fouling (Figure 3.13(c)). Here, several evaluating parameters are defined as reversible flux decline ratio ( $DR_r$ ), irreversible flux decline ratio ( $DR_{ir}$ ), flux recovery ratio ( $FRR$ ) and total flux decline ratio ( $DR_t$ ). We have calculated  $DR_r$ ,  $DR_{ir}$ ,  $FRR$  and  $DR_t$  with the formulas:  $(J_{w2}-J_{wf})/J_{w1}$ ,  $1-J_{w2}/J_{w1}$ ,  $J_{w2}/J_{w1}$ ,  $1-J_{wf}/J_{w1}$ , respectively following the similar process in membrane filtration<sup>208, 209</sup>. From Figure 3.13(c), the reversible flux decline for the colloidal aggregation (PS 0.2%) was recovered more ( $FRR=72.98\%$ ) and the reversible deposition of PS 0.2% probably released from the membrane surface by hydraulic washing. The reversible fouling for PS 0.2% accounted for  $DR_r=51\%$  from  $DR_t=78\%$  overall fouling. However, streamer fouling was found to be mainly irreversible ( $DR_{ir}=76\%$  from  $DR_t=81\%$  overall fouling) and less recovery of the flux obtained ( $FRR= 23.21\%$ ) due to the direct attachment and blockage of the pores, which were difficult to recover.

The result can be explained by the fragility of the flocs<sup>110</sup>. The PS particles are spherical (diameter, 0.2 $\mu$ m) in shape. The PS aggregates are smaller, loosely packed and fragile compared to the PAM+PS flocs which are bigger, compact, cohesive, and highly deformable<sup>210,110</sup>. As a result, the higher background shear force led to the sloughing of the loosely packed PS aggregates through the pillar pores. However, some particles/aggregates remained attached to the pillar walls<sup>211</sup>. The remaining few attached particles contributed to the very less irreversible fouling for PS 0.2% (Figure 3.13(c)). In case of PAM+PS flocs, due to the compact, cohesive

and deformable nature of the flocs, higher background shear force could not break or wash away the pores completely, contributing mostly to the irreversible fouling (Figure 3.13(c)).

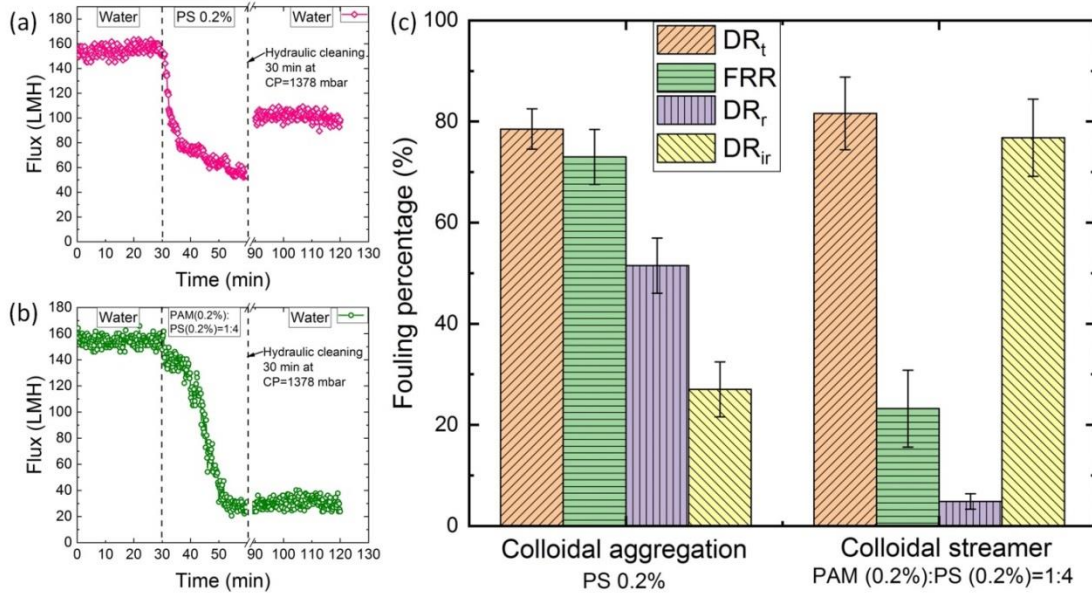


**Figure 3. 13:** Fouling percentage evaluation for colloidal aggregation and streamer fouling at the same pressure 689 mbar. At first, the dead-end filtration is performed for the clean system with pure water for 30 min, next the fouling experiments are performed for another 30 min. After that, a hydraulic cleaning is performed to clean the chip for another 30 min at higher pressure. Then, pure water filtration is performed again for 30 min. Figure (a) and (b) show the corresponding flux for PS 0.2% and PAM(0.2%):PS(0.2%)=1:4, respectively. (c) Represents the corresponding fouling percentage contributions for the same. Reversible flux decline ratio ( $DR_r$ ) is decreased by ~24% than irreversible flux decline ratio ( $DR_{ir}$ ) for colloidal aggregation and irreversible flux decline ratio ( $DR_{ir}$ ) is increased by ~72% than reversible flux decline ratio ( $DR_r$ ) for streamer fouling.

### 3.3 Conclusion

The dynamics of the fouling formation in a MMM device were presented by varying the hydrodynamic conditions and solution chemistry. Overall colloidal fouling scenarios were divided into four major categories: cake filtration, pore blocking, colloidal aggregation and

colloidal streamer. Different fouling scenarios were captured by microfluidic observations at pore scale in real-time analysis. Constant pressure experiments showed more decline in flux due to colloidal aggregation and colloidal streamer fouling at a higher pressure. Similar to the result obtained by commercial membrane fouling, the combined fouling like colloidal streamer caused more fouling in the MMM system than individual fouling. Colloidal streamer fouling is considered as a special kind of fouling which contributes more to irreversible fouling and it does not follow the Hermia model. In summary, our experimental technique models a dead-end membrane module for the microscopic fouling study and illustrates the importance of collective interplay of hydrodynamics and physiochemical interactions to establish different fouling scenarios at the pore scale. In conclusion, significant fouling may also occur due to the attachment of particles at the downstream end of membrane pores which cannot be ignored.

# Chapter 4

## Role of secondary energy minimum in microfluidic membrane fouling<sup>^</sup>

---

<sup>^</sup>The materials of this chapter has been submitted.

## 4.1 Introduction

Microfiltration (MF) and ultrafiltration (UF) have been extensively used and progressively applied in many industries like wastewater treatments<sup>212</sup>, pharmaceutical<sup>180</sup>, processing of food<sup>181</sup> and drinking water<sup>112, 184</sup>. However, fouling of membranes by suspended particles<sup>8</sup> and microbial pathogens<sup>213</sup> is one of the major challenges that decreases the life cycle of membranes and thus restricts the extensive use of membrane technology. Fouling occurs when foulants start accumulating on the surface of membrane or into the pores of membrane during filtration<sup>187</sup>. Recent investigations revealed that fouling is a result of the combined effects of hydrodynamics (permeation flux, transmembrane pressure, and flow velocity) which brings particles closer to the membrane surface and the intermolecular particle-membrane interactions (electrostatic, van der Waals, and acid-base) which cause attachment of particles to the membrane surface<sup>134, 214</sup>. At the initial stage of filtration, adhesive force between the foulants and the membrane surface plays an important role while for the later stage of filtration, foulant-foulant interactions become more significant.

Several studies used the concept of fluid flow in a porous media to study membrane fouling<sup>215, 216</sup>. Porous media like a microfluidic device can play a key role in investigating fouling at pore scale<sup>53, 134, 216, 217</sup>. This device is called microfluidic membrane mimic (MMM) as recent advancement in microfabrication technology allows using it as a membrane module mimicking the pore size of MF membranes (0.1-10 $\mu\text{m}$ )<sup>213, 216</sup>. The main advantage of using an MMM device is that it provides real time visualization as well as in-situ investigations of fouling at pore scale<sup>211, 218</sup>. Hence, an MMM device enables the analysis of fouling during filtration whereas in typical membrane filtration systems only end-point (feed and permeate side) visualization and

analysis is possible<sup>217</sup>. Also, MMM device enables investigating the interplay between hydrodynamics and chemical interactions on fouling<sup>134</sup>. Debnath and Sadrzadeh reviewed the use of MMM device in colloidal membrane fouling<sup>134</sup>. Recently, Debnath et al.<sup>216</sup> observed a new mechanism of membrane fouling called downstream fouling along with cake filtration and pore fouling using an MMM device<sup>216</sup>. Downstream fouling occurs when smaller particles compared to the membrane pore size pass through the membrane pores and accumulate at the downstream stagnation corners<sup>134, 216</sup>. They have noticed the inception of downstream fouling caused a major flux decline for the overall membrane fouling, which is not yet well established in the literature<sup>89, 110, 215, 218</sup>.

In order to fully understand the mechanism of colloidal fouling, here we investigated fouling phenomena in an MMM device, which simulates a dead-end MF process. Two colloidal foulants were used as the synthetic wastewater: PS 0.2% w/w and SiO<sub>2</sub> 0.2% w/w. Our MMM device is fabricated using polydimethylsiloxane (PDMS) consisting an array of pillars with 2 μm pillar gap and 5 μm pillar height, mimicking an MF membrane with ~3 μm hydraulic pore diameter. Hydrodynamic condition (transmembrane pressure) and the concentration of foulants were kept constant to examine the impact of intermolecular interactions on fouling for changing molar concentrations. Emphasis was given to the initial filtration condition responsible for foulant-membrane adhesion and final stage of filtration responsible for foulant-foulant cohesion. To validate our microfluidic experimental observations thermodynamic free energies (adhesion and cohesion) and XDLVO interaction energies were calculated based on contact angle method<sup>214, 219</sup>. Furthermore, microfluidic back-washing experiments were conducted to explore the role of secondary energy minimum in foulant deposition and further release of deposited particles from MMM pillars surfaces.

## 4.2 Background

### *Principles of contact angle analysis*

Surface energy parameters of the membrane (PDMS) and foulant (PS and SiO<sub>2</sub>) can be determined experimentally by contact angle approach using the extended Young's equation<sup>220</sup>.

$$(1 + \cos \theta)\gamma_L = 2 \left( \sqrt{\gamma_S^{LW} \gamma_L^{LW}} + \sqrt{\gamma_S^+ \gamma_L^-} + \sqrt{\gamma_S^- \gamma_L^+} \right) \quad (4.1)$$

$$\gamma^{AB} = 2\sqrt{\gamma^+ \gamma^-} \quad (4.2)$$

$$\gamma^{TOT} \gamma^{LW} + \gamma^{AB} \quad (4.3)$$

Where  $\theta$  is the contact angle,  $\gamma^{TOT}$  is the total surface tension,  $\gamma^{LW}$  is the Lifshitz–van der Waals component,  $\gamma^{AB}$  is the Lewis acid-base component and  $\gamma^+$  and  $\gamma^-$  are the electron acceptor and electron-donor components, respectively. The subscript  $S$  and  $L$  stands for the solid surface and the liquid, respectively. The surface tension components were converted to free energies following the model described by Childress et al.<sup>214</sup>. The free energy of adhesion ( $\Delta G_{123}^{Adh}$ ) between membrane (3) and foulants (1) in a medium like water (2) can be calculated as the sum of Lifshitz-van der Waals energy ( $\Delta G_{123}^{LW}$ ), acid-base ( $\Delta G_{123}^{AB}$ ) interaction energy and electrostatic free energy ( $\Delta G_{123}^{EL}$ ) by<sup>214, 221, 222</sup>:

$$\Delta G_{123}^{Adh} = \Delta G_{123}^{LW} + \Delta G_{123}^{AB} + \Delta G_{123}^{EL} \quad (4.4)$$

$$\Delta G_{123}^{LW} = 2 \left( \sqrt{\gamma_2^{LW}} - \sqrt{\gamma_1^{LW}} \right) \left( \sqrt{\gamma_3^{LW}} - \sqrt{\gamma_2^{LW}} \right) \quad (4.5)$$

$$\Delta G_{123}^{AB} = 2\sqrt{\gamma_2^+}(\sqrt{\gamma_1^-} + \sqrt{\gamma_3^-} - \sqrt{\gamma_2^-}) + 2\sqrt{\gamma_2^-}(\sqrt{\gamma_1^+} + \sqrt{\gamma_3^+} - \sqrt{\gamma_2^+}) - 2(\sqrt{\gamma_1^+}\sqrt{\gamma_3^-} + \sqrt{\gamma_1^-}\sqrt{\gamma_3^+}) \quad 4.6$$

$$\Delta G_{123}^{EL} = \frac{\varepsilon_0 \varepsilon_r \kappa}{2} (\zeta_3^2 + \zeta_1^2) \left( 1 - \coth(d_0 \kappa) + \frac{2\zeta_3 \zeta_1}{(\zeta_3^2 + \zeta_1^2)} \operatorname{csch}(d_0 \kappa) \right) \quad (4.7)$$

where  $\varepsilon_0 = 8.854 \times 10^{-12} CV^{-1}m^{-1}$  is the dielectric permittivity in free space,  $\varepsilon_r$  is the relative dielectric constant of the suspending fluid ( $\varepsilon_r = 78.5$  for water);  $\kappa$  is the reciprocal of the Debye screening length,  $d_0 = 0.158$  nm is the minimum equilibrium cut-off distance, and  $\zeta_3$  and  $\zeta_1$  are the surface potential of the membrane and foulants, respectively.  $\kappa$  is the reciprocal of the Debye screening length,  $\kappa = 3.29 \times 10^9 |z| \sqrt{M}$ , here  $M$  is the molar concentration of the electrolyte and  $z$  is the valence of ions.

### ***Interaction energies: Extended Derjaguin-Landau-Verwey-Overbeek (XDLVO) theory***

The total interaction energies between the membrane-foulant and foulant-foulant can be determined using extended Derjaguin-Landau-Verwey-Overbeek (XDLVO) theory. The XDLVO theory accounts for the AB interaction energy in addition to the LW and EL interaction energies to perform energy balances for aqueous system<sup>214</sup>. The total interaction energy ( $E_{123}^{XDLVO}$ ) can be written<sup>214, 220</sup>

$$E_{123}^{XDLVO} = E_{123}^{LW} + E_{123}^{EL} + E_{123}^{AB} \quad (4.8)$$

Now, the LW interaction energy as a function of separation distance ( $d$ ) per unit area decays with the inverse square of the distance between two planar geometry<sup>223</sup>. Applying Derjaguin's approximation we can convert LW interaction energy between two planar surfaces to the interaction of a flat sheet (membrane) and a sphere (foulant) by the equation<sup>214, 223</sup>

$$E_{123}^{LW}(d) = -\frac{A_H r_1}{6d} \quad (4.9)$$

Where  $A_H$  is the Hamaker constant, which can be calculated from the LW component of free energy of adhesion from equation (4.5) by

$$\begin{aligned} A_H \\ = -12\pi d_0^2 \Delta G_{123}^{LW} \end{aligned} \quad (4.10)$$

The expression for the AB interaction energy can be derived using equation (4.6) by

$$E_{123}^{AB}(d) = -2\pi r_1 \lambda \Delta G_{123}^{AB} \exp\left(\frac{d_0 - d}{\lambda}\right) \quad (4.11)$$

Where  $\lambda$  is the characteristic decay length for AB interactions in water.  $\lambda=0.6nm$  was used in the study<sup>220</sup>. The EL component of the interaction energy can be calculated by

$$E_{123}^{EL}(d) = \pi \varepsilon_r \varepsilon_0 r_1 \left( 2\zeta_3 \zeta_1 \ln\left(\frac{1 + \exp(-\kappa d)}{1 - \exp(-\kappa d)}\right) + (\zeta_3^2 + \zeta_1^2) \ln(1 - \exp(-2\kappa d)) \right) \quad (4.12)$$

where,  $r_1$  is the radius of the spherical foulant (PS and SiO<sub>2</sub>). Similarly, foulant-foulant interactions can be found by replacing 3 with 1 for equations (4.6)-(4.12) and replacing  $r_1$  with  $r_1/2$  in equation (4.12)<sup>219</sup>.

### 4.3 Material and methods

#### Microfabrication

The conventional photolithography technique was used to fabricate the microfluidic membrane mimic (MMM) device using polydimethylsiloxane (PDMS, Sylgard 184, Dow Corning, NY, USA). The details about the microfabrication process and design can be found in our previous studies<sup>215, 216</sup>. A MMM device is bonded to a cover glass by oxygen plasma to create a micro-channel after drilling inlet and outlet (Figure 4.1 (a)). Figure 4.1(a) also shows scanning electron microscopy (SEM) images of the MMM device with detailed dimensions. Each sample was carbon coated (Denton Vacuum, Desk II, Moorestown, New Jersey) before imaging by the field emission SEM (Zeiss, Oberkochen, Germany) at 20 kV with an in-lens secondary electron detector<sup>216</sup>. The pore size (hydraulic diameter  $d_h \sim 3\mu\text{m}$ ) and filtration performance of this MMM device is comparable to a MF membrane (pore size 0.1-10 $\mu\text{m}$ ), as described by Debnath et al.<sup>216</sup>.

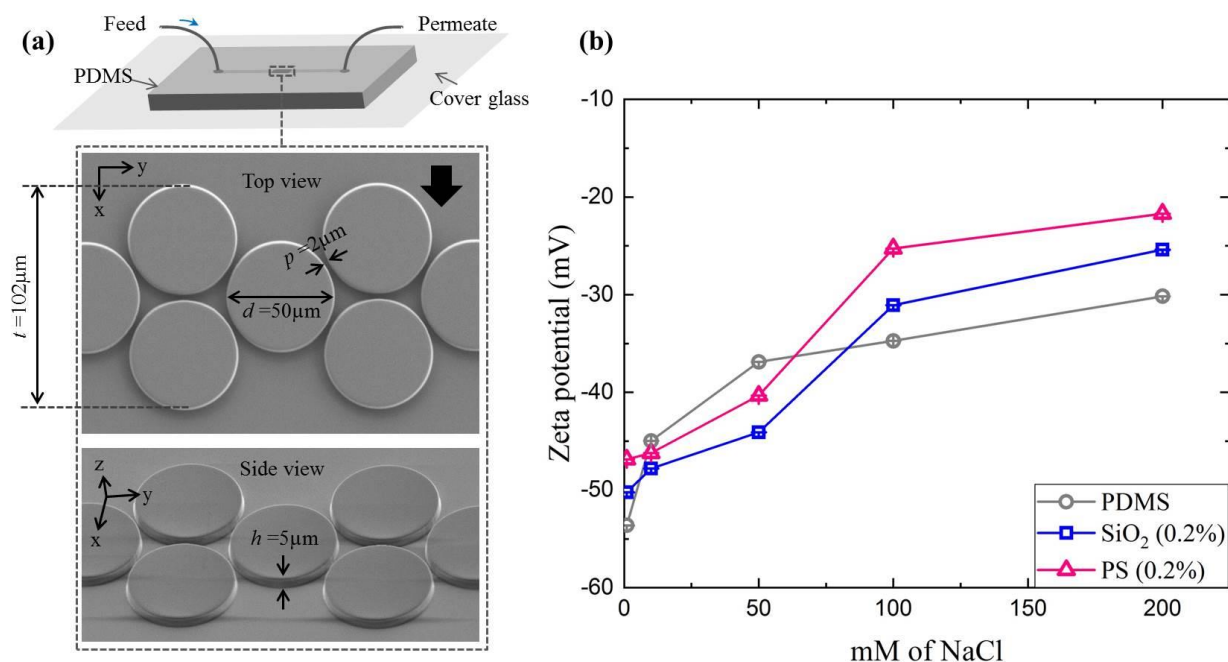


**Figure 4. 1:** (a) PDMS microfluidic chip bonded to cover glass with inlet for feed and outlet for permeate. SEM image shows the top view and side view of the microchip with dimensions (b) Zeta potential as a function of mM of NaCl for PDMS, SiO<sub>2</sub> (0.2% w/w) & PS (0.2% w/w) surfaces at room temperature.

#### ***Foulant solution preparation (PS and SiO<sub>2</sub>)***

0.2% w/w PS and SiO<sub>2</sub> synthetic wastewater solutions were prepared for the fouling study. 0.2% w/w PS particle solution was prepared by dissolving amine-modified polystyrene beads (Radius  $R_{PS} \sim 100\text{nm}$ , excitation at 580 nm, emission at 605nm, Life Technologies, ON, Canada) into Millipore water. PS particles were red fluorescent under fluorescent microscopy used for the ease of microfluidic fouling observation. To study the effect of molar concentration on the LW, EL and AB components of interaction energy, the NaCl molar concentrations varied from 1mM, to 200mM while the PS concentration was kept constant (0.2% w/w). Similarly, 0.2% w/w SiO<sub>2</sub> particle solution (Radius  $R_{SiO_2} \sim 42\text{nm}$ , Snowtex, Nissan Chemicals) was prepared at different molar concentrations. The pH of the colloidal solutions was adjusted at 8 using 0.1M NaOH solution. The particular pH=8 was selected to create unfavourable interactions so that the possibility of finding secondary energy minimum becomes most probable<sup>224–226</sup>. Both foulants were introduced into the inlet of the MMM device at constant transmembrane pressure of 689 mbar for all fouling experiments at room temperature.

#### ***PDMS surface modification and contact angle measurement***

First, PDMS sample was cut into 2in. × 2in. coupons. Then, oxygen plasma was used for 1min at 500mtor pressure with 100W power to render PDMS surface hydrophilic<sup>227</sup>. After that, prepared foulant solutions of 5 different molar concentration were immediately poured onto the plasma-

treated membrane coupons for 10 min at room temperature in 5 beakers<sup>228, 229</sup>. Next, the samples were finally blown dry with nitrogen and heated on a hotplate at 80°C for 15 min to ensure stability of the coating<sup>229</sup>. After that, the PS coated membrane chips were washed again to remove excess salt and finally blown dry with nitrogen before the contact angle measurement<sup>230</sup>. Similarly, 5 different SiO<sub>2</sub> coated membrane chips were prepared. Finally, the contact angle measurements were performed on fifteen dried coated PDMS surfaces: five for PS-coated samples at 5 different NaCl molar concentrations (1 mM, 10 mM, 50mM, 100 mM, 200 mM); five for SiO<sub>2</sub>-coated samples at the same NaCl concentrations; and five for foulant-free PDMS surfaces treated with only NaCl of the same concentrations which were referred to as the clean membranes. Yu et al.<sup>230</sup> studied the evaporative deposition of PS particles on PDMS surface and noticed that at lower concentration of PS a monolayer of PS was formed on the PDMS surface<sup>230</sup>. Toepke and Beebe<sup>231</sup> noticed retainment of hydrophobic small molecules on PDMS surface even after several wash in a microchannel. The coated surface SEM images are shown in the Figure 4.2.

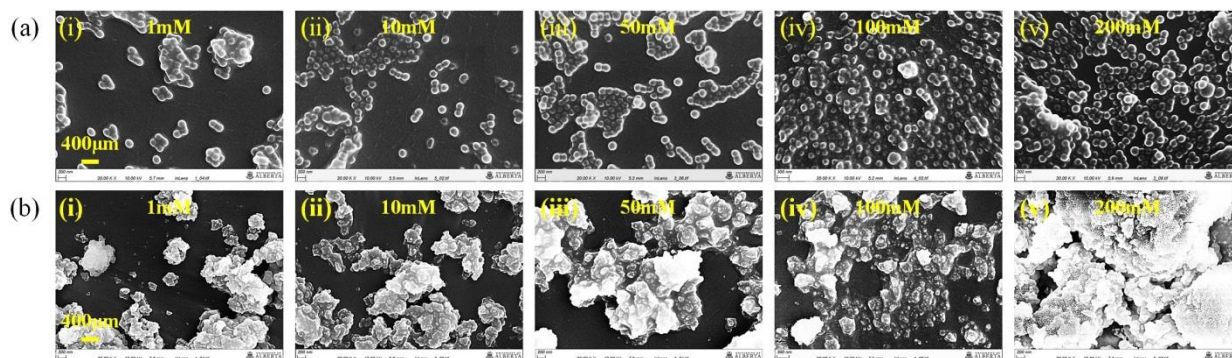


**Figure 4. 2:** SEM images of the coated PDMS surfaces with deposited foulants. Deposition of foulants on PDMS surface is increased with molar strength.

Figure 4.2 shows foulant deposition increased with increasing molar concentration on PDMS surface. In-air water contact angle measurements were conducted with three probe liquids (water,

diiodomethane and formamide) using a contact angle analyser (Kruss DSA 100E, Hamburg, Germany) at 7 different locations of the samples and the average values of the contact angle were reported (Figure 4.3). Figure 4.3 shows all contact angle results. The contact angle for polar liquids like water and formamide were decreased and apolar liquids like diiodomethane it was increased with ionic concentrations (Figure 4.3). The similar trend was also observed in several literature for polymeric membranes<sup>214, 219, 221</sup>. It might be because, as increasing ionic strength the deposition of foulants were increased (Figure 4.2), the interaction of polar liquids were decreased while apolar liquid like diiodomethane showed more interactions with the coated PDMS surface<sup>214, 219, 221</sup>.

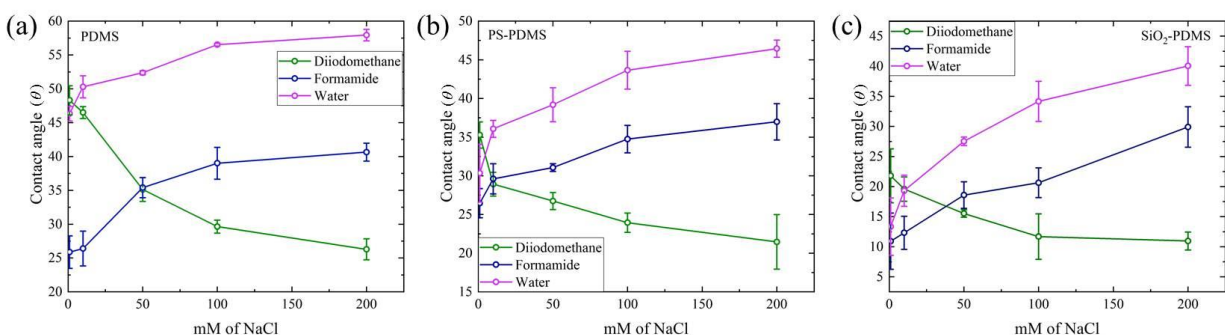


**Figure 4. 3:** Contact angle of diiodomethane, formamide and water with increasing NaCl molar concentrations for (a) PDMS, (b) PS-PDMS and (c) SiO<sub>2</sub>-PDMS.

### *Surface zeta potential*

The surface zeta potential of PDMS was measured using SurPASS<sup>TM</sup> 3 Electrokinetic Analyzer (Anton Paar, Graz, Austria) using 1mM KCl solution as the electrolyte at pH=8. The surface zeta potential of the foulants PS and SiO<sub>2</sub> were measured using a Zetasizer Nano ZS (Malvern, USA) which are shown in Figure 4.1(b). PS surfaces showed relatively less negative zeta potential for all molar concentrations than SiO<sub>2</sub> (Figure 4.1(b)).

### ***Experimental set up***

The MMM device was placed under an inverted optical microscope (Nikon Eclipse Ti) to observe the fouling directly. The details about the experimental set up is given in our previous study<sup>216</sup>. A pressure-driven flow was created in the MMM device by using microfluidic flow control system (MFCS) (Fluigent, MA, USA), mimicking a dead-end filtration setup. The feed solution was sent through the inlet via a flow unit (Fluigent, MA, USA) and permeate was stored from the outlet in a waste beaker (Figure 4.1(a)). A constant-pressure difference ( $\Delta P=689$  mbar) was maintained by the microfluidic pressure controller (MFCS-EZ) (Fluigent, MA, USA) for all experiments. The flow-rate-control-module software (Fluigent, MA, USA) measured the volumetric flow rate ( $Q$ ) directly. The MFCS (Flow unit) was never let to dry & cleaned three times with ethanol solution before changing any feed sample. It is important to note that all experiments were conducted at creeping flow condition ( $Re<1$ ) with maximum fluid velocity  $v_{max}\sim 6.84\times 10^{-4}$  m/s. All experiments were performed at room temperature and repeated three times.

## **4.4 Result and discussion**

### **4.4.1 Determination of free energies**

To determine the surface tension components contact angle measurements were performed using three probe liquids with known surface tension properties: apolar diiodomethane (Fisher Scientific, Pittsburgh, PA), polar formamide (Fisher Scientific, Pittsburgh, PA) and polar ultrapure water. The surface tension components as well as polar and free energy components for these three probe liquids are listed in Table 4.1<sup>232</sup>.

**Table 4. 1:** Surface tension parameters and energy components (mJ/m<sup>2</sup>) of probe liquids at 20°C. Data is taken from van Oss<sup>220</sup>.

Probe liquids	$\gamma_L$	$\gamma^+$	$\gamma^-$	$\gamma^{AB}$	$\gamma^{LW}$
Diiodomethane	50.8	0.01	0	0	50.8
Formamide	58	2.28	39.6	19	39
Water	72.8	25.5	25.5	51	21.8

Sessile drop contact angle measurements were performed by releasing 3 $\mu$ L droplets of the probe liquid using a 1mL syringe at a minimum distance from the surface. Seven contact angle measurements were taken at seven different locations and the average value (with <5% standard deviation) was used for further analysis. The contact angle results in Figure 4.3 suggested that the chemistry of the PDMS surfaces altered significantly by the increased deposition of PS (0.2% w/w) and SiO<sub>2</sub> (0.2% w/w) on PDMS surfaces (Figure 4.2). Based on the contact angle data the surface tension components and free energy components were calculated using equations (4.1)-(4.7) and listed in the Tables 4.2 and 4.3, respectively.

**Table 4. 2:** Surface energy parameters of membranes and colloids.

Surfaces	NaCl mM	$\gamma^+$	$\gamma^-$	$\gamma^{AB}$	$\gamma^{LW}$	$\gamma^{TOT}$
PDMS	1	2.74	25.42	16.70	35.21	51.91
PDMS	10	1.71	23.77	12.75	38.33	51.09
PDMS	50	0.59	23.48	7.44	41.97	49.42
PDMS	100	0.24	20.55	4.44	44.37	48.81
PDMS	200	0.11	19.87	2.93	45.68	48.61
PS-PDMS	1	0.47	45.62	9.26	41.90	51.16
PS-PDMS	10	0.20	41.09	5.70	44.66	50.37
PS-PDMS	50	0.14	38.19	4.62	45.51	50.14
PS-PDMS	100	0.04	34.91	2.36	46.52	48.88
PS-PDMS	200	0.01	32.78	1.01	47.34	48.35
SiO <sub>2</sub> -PDMS	1	0.31	53.41	8.14	47.23	55.37
SiO <sub>2</sub> -PDMS	10	0.30	49.91	7.73	47.90	55.64
SiO <sub>2</sub> -PDMS	50	0.17	45.00	5.53	48.96	54.49
SiO <sub>2</sub> -PDMS	100	0.18	38.73	5.28	49.75	55.03

SiO <sub>2</sub> -PDMS	200	0.02	36.66	1.71	49.88	51.59
------------------------	-----	------	-------	------	-------	-------

**Table 4. 3:** Surface free energy parameters of colloids.

Surfaces	NaCl mM	$\Delta G_{121}^{LW}$	$\Delta G_{121}^{AB}$	$\Delta G_{121}^{EL}$	$\Delta G_{121}^{Coh}$	$\Delta G_{123}^{LW}$	$\Delta G_{123}^{AB}$	$\Delta G_{123}^{EL}$	$\Delta G_{123}^{Adh}$
PS-PDMS	1	-6.51	48.28	0.0001	41.77027	-4.56	11.50	0.00008	6.93554
PS-PDMS	10	-8.11	36.47	0.0005	28.35508	-5.43	8.58	0.00045	3.15045
PS-PDMS	50	-8.63	30.38	0.0009	21.75573	-7.52	7.77	0.00069	0.25066
PS-PDMS	100	-9.26	17.35	0.0004	8.10006	-8.57	2.82	0.00042	-5.74984
PS-PDMS	200	-9.78	15.43	0.0004	5.65148	-9.24	0.50	0.00046	-8.73896
SiO <sub>2</sub> -PDMS	1	-9.71	56.87	0.0002	47.15254	-5.57	15.26	0.00016	9.6812
SiO <sub>2</sub> -PDMS	10	-10.14	51.75	0.0004	41.12826	-6.86	13.51	0.00047	7.43807
SiO <sub>2</sub> -PDMS	50	-10.84	41.83	0.0009	30.98665	-8.43	12.31	0.00067	3.88213
SiO <sub>2</sub> -PDMS	100	-11.37	32.28	0.0006	20.90365	-9.50	5.92	0.00068	-3.57423
SiO <sub>2</sub> -PDMS	200	-11.46	23.16	0.0005	11.69979	-10.00	3.68	0.00065	-6.32702

This result is in good agreement with previous studies as polymeric membranes like PDMS is typically high electron donor (Table 4.2). Also, the increase in the zeta potential (Figure 4.1(b)) and the decrease in electron donor ( $\gamma$ ) components (Table 4.2) with the addition of salt showed consistency in our both contact angle and zeta potential experimental results<sup>233</sup>. The interfacial free energy of cohesion ( $\Delta G_{123}^{Coh}$ ) represents the free energy when two surfaces of same material are immersed in water and the interfacial free energy of adhesion ( $\Delta G_{123}^{Adh}$ ) represents the free energy when two surfaces of different materials are immersed in water<sup>214</sup>. Figure 4.4 shows that the free energy of cohesion ( $\Delta G_{123}^{Coh}$ ) and adhesion ( $\Delta G_{123}^{Adh}$ ) both decreased with increasing ionic strength for PS and SiO<sub>2</sub>. Cohesive energy remained positive, indicating that hydrophilic interactions for PS-PS and SiO<sub>2</sub>-SiO<sub>2</sub> dominate while adhesive energy changed sign by increasing molar concentrations, implying that foulant-membrane interactions became hydrophobic<sup>214</sup>. Among these interactions the electrostatic free energy ( $\Delta G_{123}^{EL}$ ) was negligible and acid-base free energy ( $\Delta G_{123}^{AB}$ ) was predominant for all (Table 4.3). Based on the calculated

thermodynamic free energies from contact angle data the XDLVO interaction energies were calculated as discussed next.

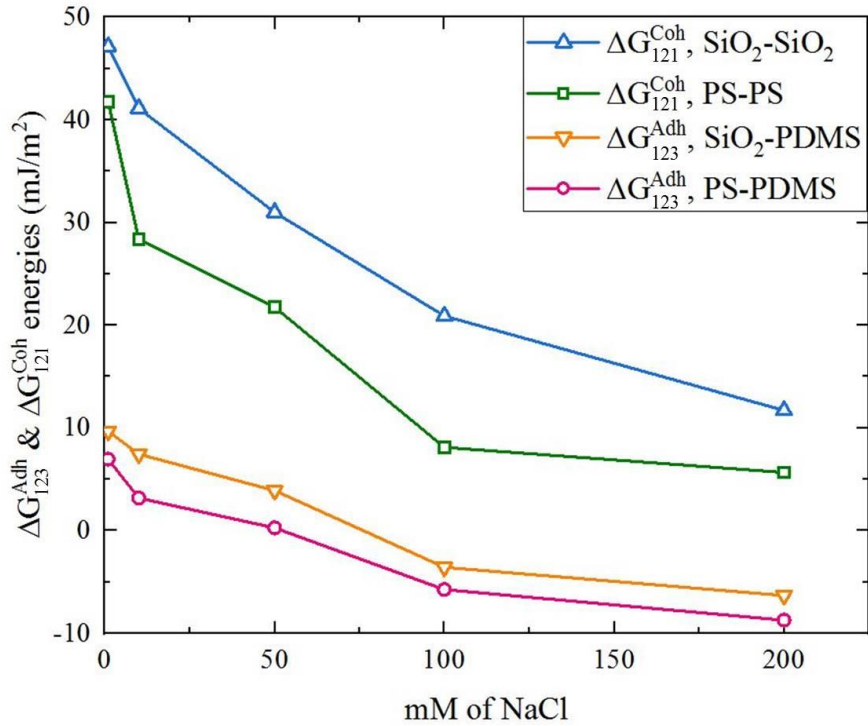


**Figure 4. 4:** Cohesion energy ( $\Delta G_{123}^{Coh}$ ) for SiO<sub>2</sub>-SiO<sub>2</sub> and PS-PS and adhesion energy ( $\Delta G_{123}^{Adh}$ ) for SiO<sub>2</sub>-PDMS and PS-PDMS as a function of NaCl molar concentrations.

#### 4.4.2 Determination of energy minimum

Although the hydrodynamic forces are responsible to forward the foulants close to the membrane surface, it is the thermodynamic adhesion forces that cause initial attachment of the particles to the membrane surface and cohesion force plays an important role for later stages of fouling<sup>225</sup>. In order to investigate the influence of free energies for changing molar concentrations and foulant properties such as particle size, surface charge and electrical properties on membrane fouling,

XDLVO theory was applied to predict the interaction behavior of the foulant-membrane and foulant–foulant separately<sup>214, 219, 221, 222, 234</sup>. XDLVO theory includes the polar AB interactions as well as LW, EL interactions over classical DLVO theory<sup>214</sup>. Many researchers found that AB interaction plays a major role in overall membrane fouling interactions<sup>9,221, 234</sup>.

In general, when colloids are flowing through a porous media, the deposition, release, and transport of colloidal particles occur simultaneously. Recently, many studies have been conducted on the role of secondary energy minimum in the release of particles<sup>211, 226, 235–238</sup>. When a colloid is deposited within the secondary energy minimum, it can either overcome the energy barrier to deposit at the primary energy minimum or release to the bulk fluid flow. The presence of a significant repulsive energy barrier would cause more particles to remain in the secondary energy minimum. In other words, the particles having lower energy to overcome the energy barrier could remain associated with the membrane surface within the secondary energy minimum or release to the bulk. Also, Brownian diffusion may lead to spontaneous detachment of the colloids even from primary energy minimum<sup>239</sup>.

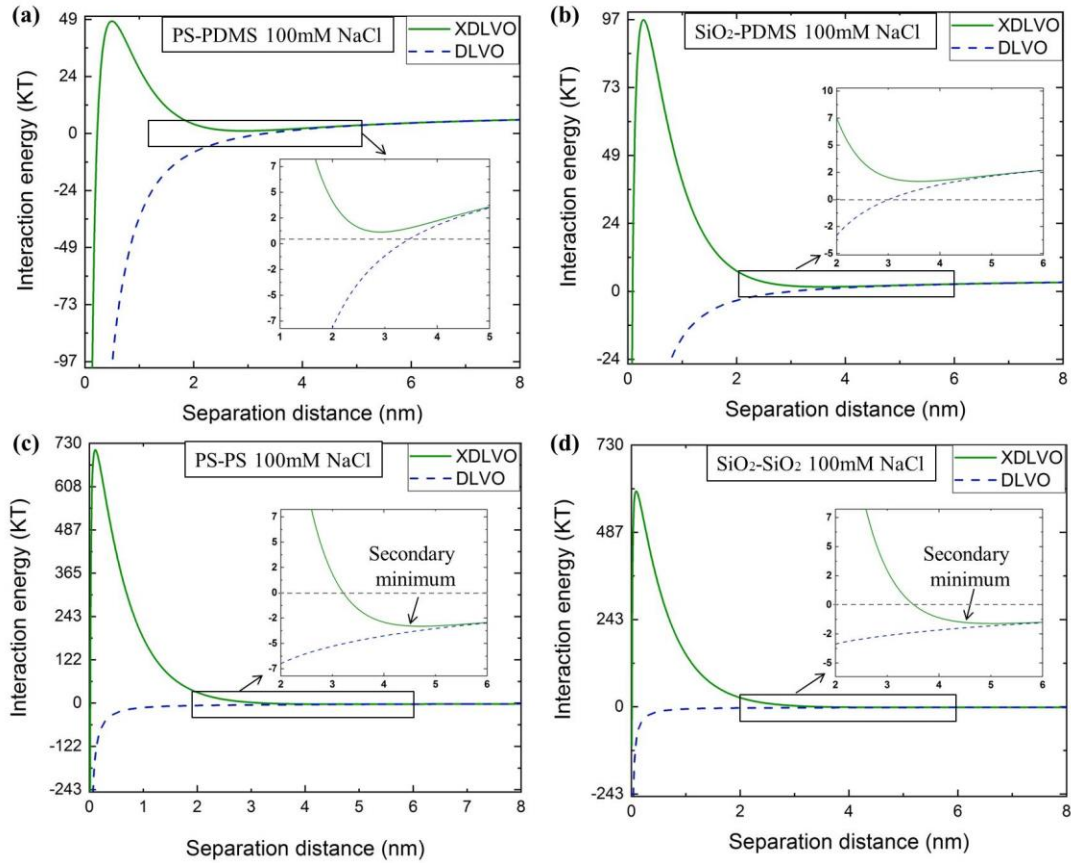
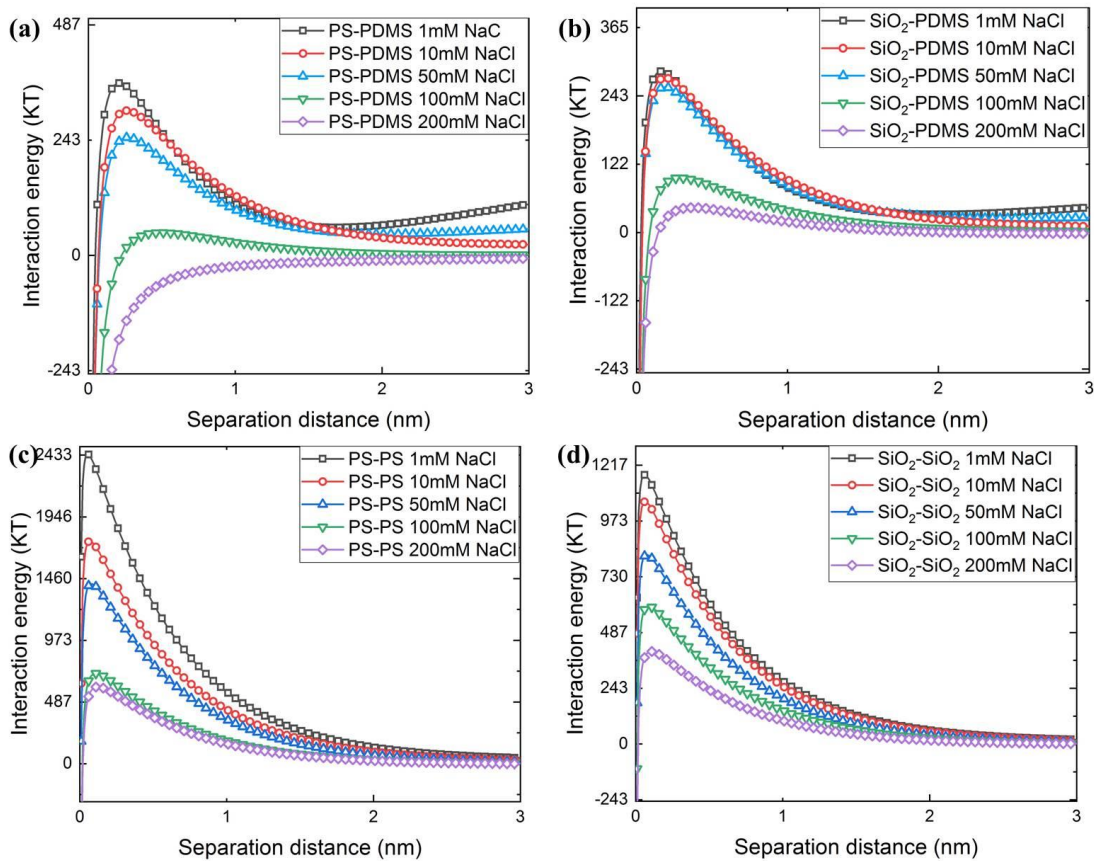


**Figure 4. 5:** DLVO and XDLVO interaction energy profile for foulant-membrane (a) PS-PDMS, (b) SiO<sub>2</sub>-PDMS and foulant-foulant (c) PS-PS, (d) SiO<sub>2</sub>-SiO<sub>2</sub> interactions at 100mM NaCl. The enlarge version shows the existence of the secondary energy minimum for (c) and (d).

In order to examine the presence of energy barrier and secondary energy minimum, we calculated the interactions energies using equations (4.8)-(4.12). Figure 4.5 shows the DLVO and XDLVO interaction energy profile for PS-PDMS, SiO<sub>2</sub>-PDMS, PS-PS, and SiO<sub>2</sub>-SiO<sub>2</sub> interactions at 100mM NaCl concentration. PS-PDMS interactions showed lowest energy barrier and PS-PS interactions showed highest energy barrier (Figure 4.5 ((a), (c))). At 100mM of NaCl SiO<sub>2</sub>-PDMS showed higher repulsive energy barrier (Figure 4.5(b)) than PS-PDMS (Figure 4.5(a)). This might be due to more SiO<sub>2</sub>-PDMS electrostatic repulsion than PS-PDMS, as SiO<sub>2</sub> is found to be more negatively charged than PS (Figure 4.1(b)). The secondary energy minimum

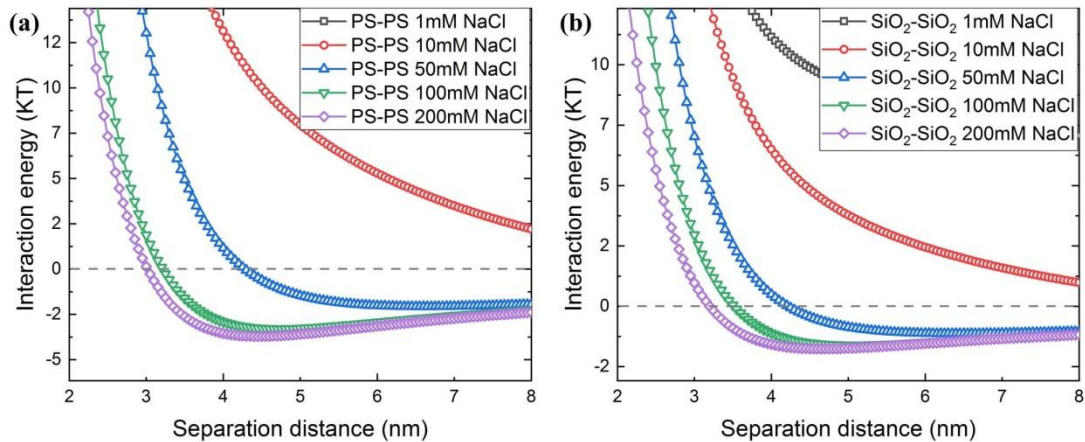
depth for PS-PS and SiO<sub>2</sub>-SiO<sub>2</sub> were about -3.5KT, -1.75KT, respectively. Here, increasing particle size might result in more particle deposition in the secondary energy minimum as PS ( $R_{PS} \sim 100\text{nm}$ ) is twice the size of SiO<sub>2</sub> ( $R_{SiO_2} \sim 42\text{nm}$ )<sup>238</sup>.

Figure 4.6 summarizes the XDLVO interaction energy profiles for foulant-membrane (Figure 4.6(a), (b)) and foulant-foulant (Figure 4.6(c),(d)) interactions at all ionic concentrations. The interaction energy was found to decrease with increasing ionic strength<sup>221, 234, 240</sup> (Figure 4.6). Energy barrier was much higher for the case of foulant-foulant (Figure 4.6(c), (d)) interactions as compared to that foulant-membrane (Figure 4.6(a), (b)).



**Figure 4. 6:** XDLVO interaction energy profile for (a) PS-PDMS, (b) SiO<sub>2</sub>-PDMS, (c) PS-PS and (d) SiO<sub>2</sub>-SiO<sub>2</sub> with varying molar concentrations as a function of separation distance.

The reversible attachment of colloids in the secondary energy minimum plays an important role in determining the extent of colloid transport in the subsurface<sup>236</sup>. Figure 4.7 shows the secondary energy minimum for all molar concentrations for PS and SiO<sub>2</sub> surfaces. Secondary energy minimum depth for PS-PS interaction was almost twice the depth for SiO<sub>2</sub>-SiO<sub>2</sub> at 50,100 and 200mM ionic concentrations (Figure 4.7). These results provides good supports with previous investigations as it was found that increasing ionic strength caused a growing secondary well and a smaller height of energy barrier<sup>214, 218, 219, 221, 222</sup>. Also, increasing colloid size influences deeper secondary well and a greater height of energy barrier<sup>214, 218, 219, 221, 222</sup>. As PS ( $R_{PS} \sim 100\text{nm}$ ) is almost twice the size of SiO<sub>2</sub> ( $R_{SiO_2} \sim 42\text{nm}$ ), it might cause higher interaction energies (LW, EL and AB) and greater secondary well (Figure 4.6 & 4.7). Increasing ionic strength more foulants tend to deposit on the membrane surface due to the shrinkage of the double layer thickness<sup>240</sup>. Another interesting point is that the distance to the secondary energy minimum became closer to the surface and the span of the secondary energy well became narrower<sup>239</sup> (Figure 4.7).



**Figure 4. 7:** Secondary energy minimum depth for (a) PS-PS interactions were twice the depth of secondary energy minimum for (b) SiO<sub>2</sub>-SiO<sub>2</sub> for 50mM, 100Mm and 200mM NaCl molar concentrations.

### 4.4.3 Microfluidic results

#### *Microfluidic constant pressure filtration*

Constant pressure dead-end filtration is performed in order to investigate the effect of molar concentration on colloidal fouling using an MMM device. The flux decline during the filtration of 0.2%w/w PS and SiO<sub>2</sub> is shown in Figure 4.8 for 1mM, 50mM and 100mM NaCl concentration. The flux for PS at 1mM ionic strength was found to drop by 62.5% after 10min, while at 50 and 100mM ionic strength 93.7% decrease was observed after 10min and 5 min of filtration, respectively (Figure 4.8(a)). In the case of SiO<sub>2</sub>, the initial flux decline was sharper and the steady state was reached in less than 2 min for all concentrations of NaCl (Figure 4.8(b)).

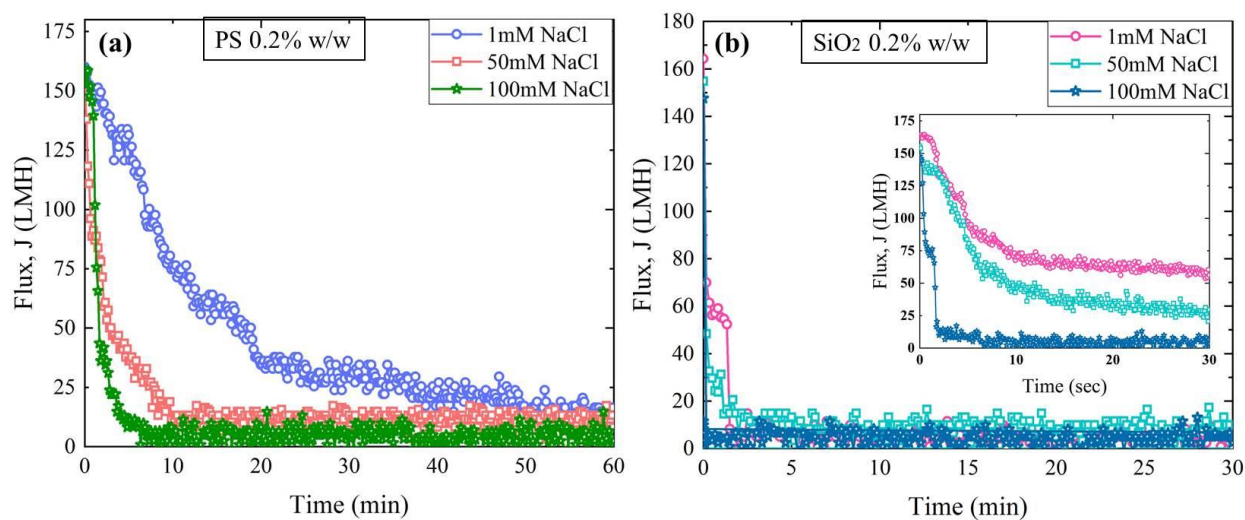


**Figure 4. 8:** Flux vs time plot for microfluidic constant pressure filtration (689mbar) showing severe flux decline with increasing molar concentrations for SiO<sub>2</sub> 0.2% w/w foulant compared to PS 0.2% w/w foulant.

This result suggests that the adhesion between foulant and membrane at the initial stage of filtration was more important than foulant-foulant interaction at the later stage. Our surface energy results showed more adhesion for SiO<sub>2</sub>-PDMS than PS-PDMS (Figure 4.4); therefore

more severe flux decline within few seconds of filtration is expected (Figure 4.8(b)). In addition, higher SiO<sub>2</sub>-SiO<sub>2</sub> cohesion energy resulted in more resistance against flow through the SiO<sub>2</sub> cake layer. Apparently, for both PS and SiO<sub>2</sub>, flux decline was sharper and steady flux reached sooner by increasing the ionic strength (Figure 4.8). All constant-pressure filtration experiments were repeated three times at room temperature (Figure 4.9).

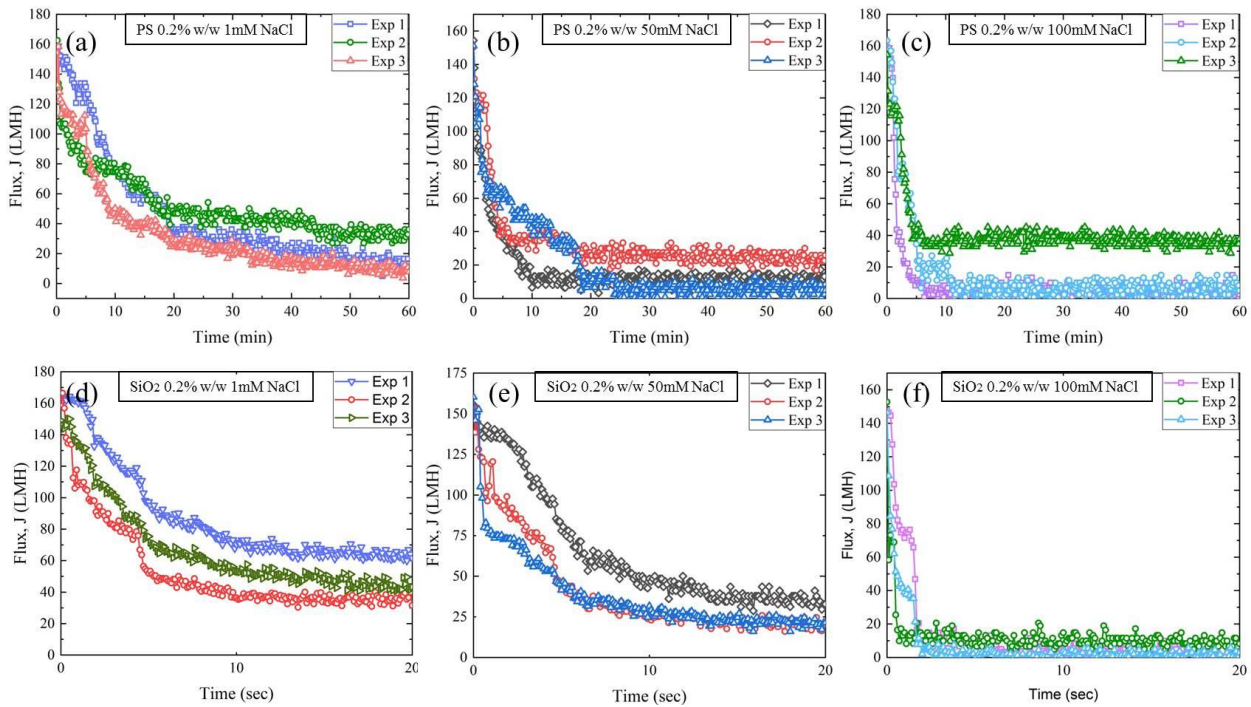


**Figure 4. 9:** Constant pressure repeatability experiments for 1mM (a) and (d), 50mM (b) and (e) and 100mM (c) and (f) of NaCl at 689mbar pressure.

The corresponding microfluidic fouling images in Figure 4.10 showed cake layer formation for SiO<sub>2</sub> fouling only and cake layer with downstream fouling for PS<sup>216</sup>. Also, downstream fouling intensified for PS and cake layer thickness increased for SiO<sub>2</sub> by increasing the ionic strength (Figure 4.10(b) and (c)). In case of PS, downstream fouling was noticed but for SiO<sub>2</sub>, most of the particles were re-suspended and washed away with the background flow. Less cohesion and

adhesion energies of PS as compared to SiO<sub>2</sub> (Figure 4.4) caused the PS particles to move to the downstream side. In fact, the combined effect of the higher energy barrier (Figure 4.6(a), (b)) and the presence of the secondary minimum (Figure 4.7(a)) caused more PS particles to move to the downstream side of the pillars.

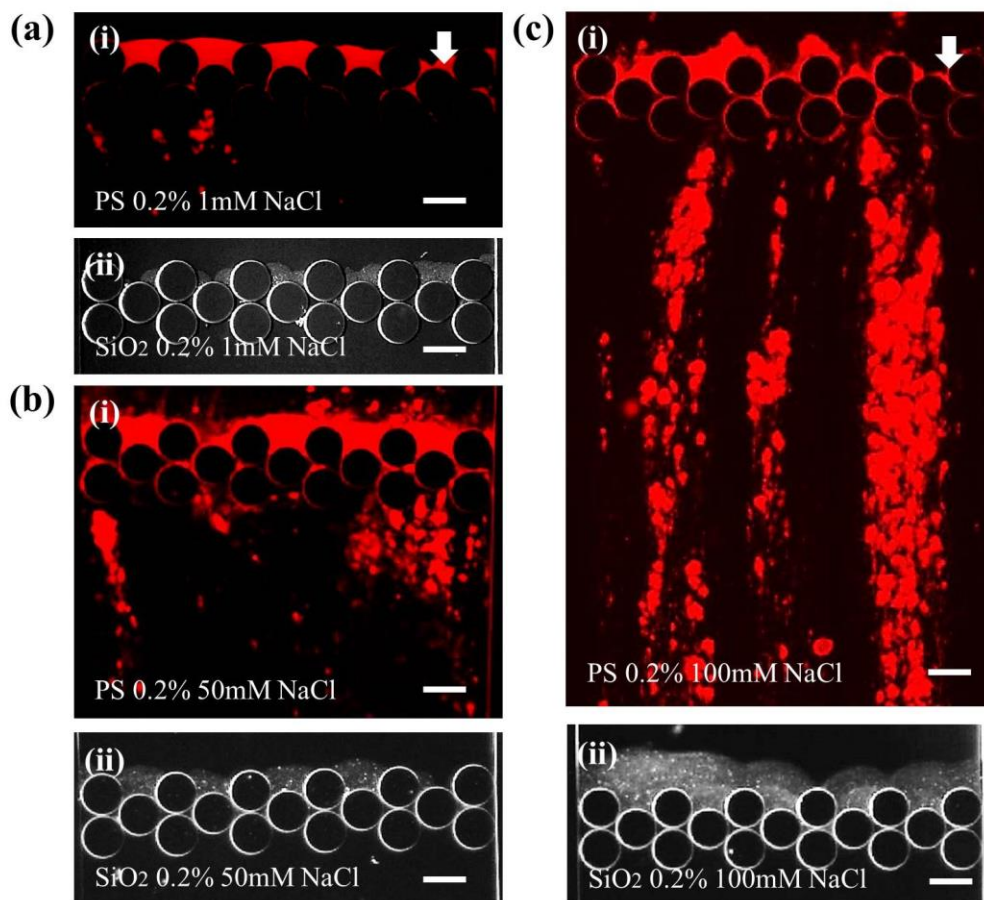


**Figure 4. 10:** Microfluidic fouling images showed cake layer fouling for SiO<sub>2</sub> and cake layer with downstream fouling for PS for different ionic concentrations of NaCl (a) 1mM, (b) 50mM, (c) 100mM at 689mbar pressure. All scale bars are 50 $\mu$ m.

Despite of many arguments of colloidal attachment in the secondary energy minimum, such as; this attachment only occur in case of a smooth collector surface at the stagnation point or even in case of parallel plate flow with no stagnation point<sup>241</sup>, from our microfluidic experiments we

noticed, fouling (cake layer and downstream fouling) was present in all around the pillar surfaces and only PS particles moved to downstream stagnation point at the same fluid shear and chemical conditions when compared to SiO<sub>2</sub>. Based on our microfluidic results we hypothesize that the initial phase of fouling is mostly influenced by the primary energy attachment and the downstream fouling can only occur after the initial phase of filtration when deposition at the primary energy minimum has already occurred. After the initial phase of fouling, deposition at the secondary energy minimum is favored under unfavorable chemical conditions<sup>241</sup>. When particles start depositing at the secondary energy minimum, fouling behavior might alter from a cake layer to downstream fouling. As the PS particles are twice in size than the SiO<sub>2</sub>, the larger gap among deposited PS particles or local higher surface roughness increased the possibility of additional PS particle attachment in the secondary energy minimum<sup>242</sup>. Also, the less cohesive force among PS particles caused more PS particles to move to the downstream side and attach again when fluid shear was reduced at the downstream stagnation corner. From XDLVO calculations and microfluidic experiments we have noticed increasing depth of secondary energy minimum and the height of energy barrier also favored the release of more PS particles to the bulk fluid. To explain more on the inception of the downstream fouling from initial cake layer fouling and PS particle release from secondary energy minimum we have conducted back-washing experiments as discussed in the next section.

### ***Back-washing: reversible deposition at the secondary energy minimum***

In our MMM device, we have conducted the back-washing experiments by switching the outlet and inlet of the device for both the foulants. By increasing the pressure up to 689 mbar, different particle release phenomena were observed. Interestingly, we have observed PS particles started

to release from the cake layer even at zero or lower pressure than 689mbar while very few particles were released for SiO<sub>2</sub> (Figure 4.12 & 4.13). The primary and secondary water channels were formed for PS release while in case of SiO<sub>2</sub> it was absent. At 689 mbar pressure, these water channel formation through the PS cake layer was found to be the primary reason for the easier release of PS (Figure 4.11(a))<sup>216</sup>. In our previous study we observed water channel formation for downstream fouling phenomenon<sup>216</sup>.

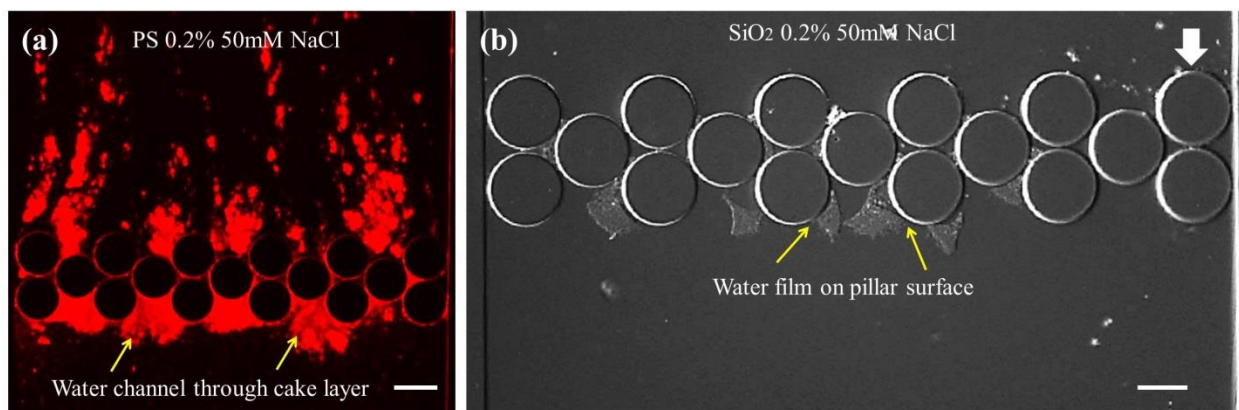


**Figure 4. 11:** Microfluidic back-flashing experiments for PS and SiO<sub>2</sub> fouling in MMM device showed (a) particle release by water channel formation from cake layer for PS at 689mbar and (b) cake layer release by water film formation around pillar surface for SiO<sub>2</sub> at >689mbar pressure.

On the other hand, very few particles were released from SiO<sub>2</sub> cake layer even until 689mbar for all salt concentrations. When we further increased the pressure higher than 689mbar for SiO<sub>2</sub>, a thin water film was formed around the pillars which segregated SiO<sub>2</sub> cake layer from the pillar surfaces by keeping their cake layer profile intact (Figure 4.11(b)). From Figure 4.11(b), we noticed that SiO<sub>2</sub> cake layer were separated from the pillars and started to rotate and glide along the flow (>689mbar). This is probably because SiO<sub>2</sub>-SiO<sub>2</sub> cohesion is almost 5 times larger than SiO<sub>2</sub>-PDMS adhesion (Figure 4.4), background fluid flow could not separate the SiO<sub>2</sub> particles from each other or initiate any water channel through SiO<sub>2</sub> cake layer. With more filtration, most

of the PS particles were separated and few particles were noticed to release even from the downstream fouling side (Figure 4.12). However, few PS particles remained attach to the PDMS surface in the primary energy minimum even after several back-washing (Figure 4.12). Our back-washing experiments showed release of SiO<sub>2</sub> cake layer form PDMS surface, indicating particle release form primary energy minimum is possible at higher pressure<sup>243</sup>.

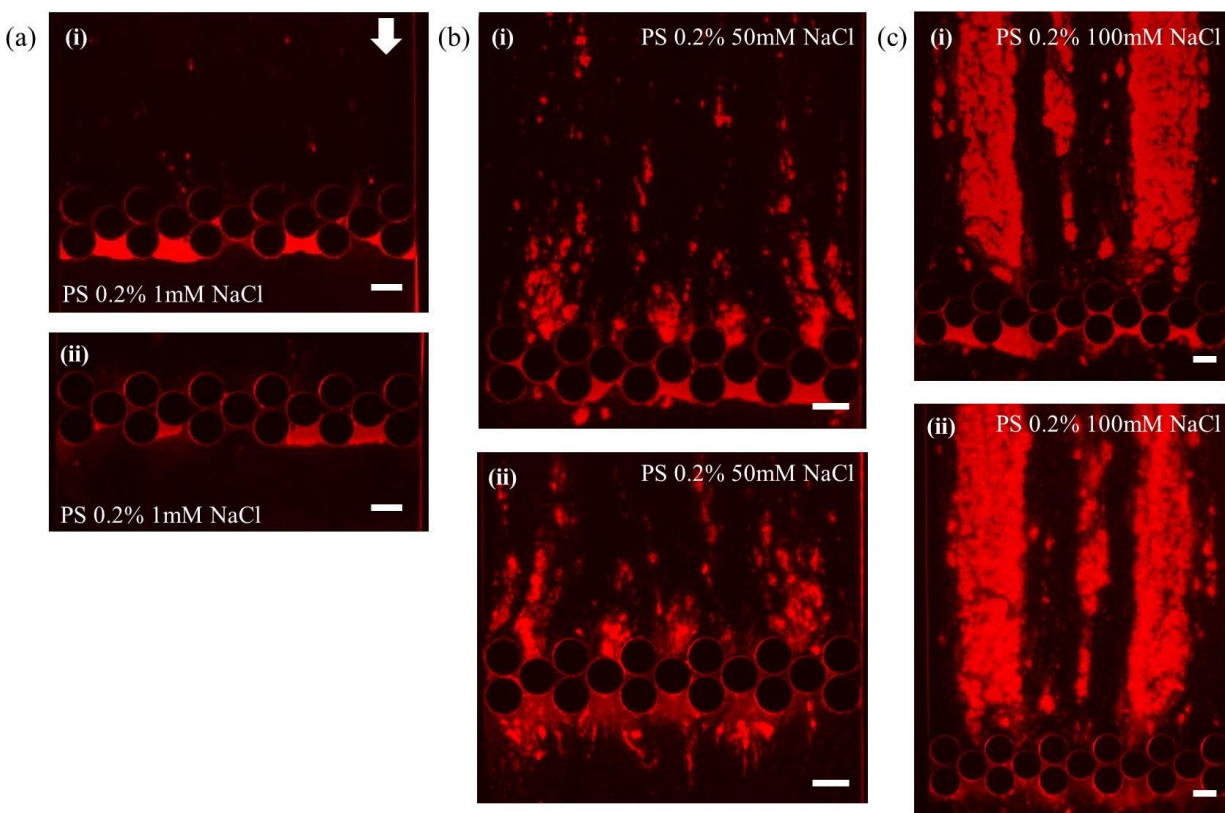


**Figure 4. 12:** Microfluidic back-flashing results at 689mbar pressure for PS before back-flashing (a)(i),(b)(i),(c)(i) and after back-flashing (a)(ii),(b)(ii),(c)(ii) showed particle release from secondary energy minimum.

If a particle is attached to the surface in its secondary energy minimum then because of the larger separation distance (4-5nm) from surface, a fluid layer can exist in between, especially for a hydrophilic surface which helps further gliding or sliding of the particle or aggregates and they can reach to primary energy minimum<sup>239</sup>, relocate to secondary energy minimum or release in

the bulk fluid<sup>211, 218, 225, 235–239</sup>. For example, back-washing experiment for SiO<sub>2</sub> in 50mM salt solution, showed removal of cake layer at higher pressures (>689mbar) altogether from PDMS surface. On the other hand, the PS particles started to separate from the outer cake layer even when the pressure was reduced to zero (zero flow rate condition) (Figure 4.12). PS particles were loosely packed due to lower cohesive force and mostly deposited to the secondary energy minimum which was reversible<sup>224</sup> (Figure 4.12). From these observations we hypothesize that release of deposited PS particles from cake layer (for pressure <689 mbar) might be the reason behind the inception of downstream fouling.

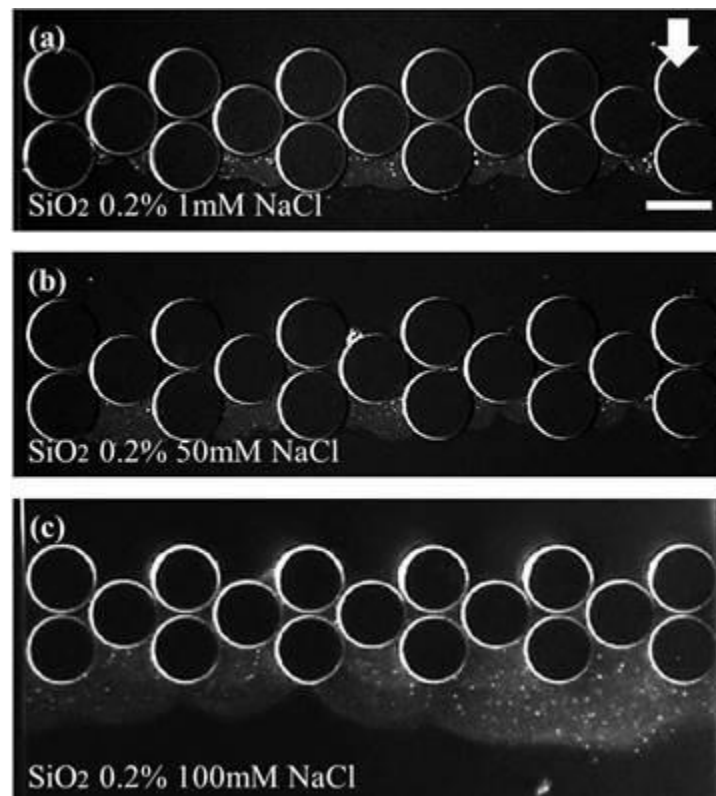


**Figure 4. 13:** Microfluidic back-flashing results at 689mbar pressure for SiO<sub>2</sub> showed very few particle release from the outer surface of the cake layer at (a) 1mM NaCl (b) 50mM NaCl and (c) 100mM NaCl.

In summary, our experimental results suggest that by changing particle size and surface charge, different fouling phenomena can be observed such as cake layer and downstream fouling for similar experimental conditions. SiO<sub>2</sub> being a smaller dimension (half the size of PS) was expected to result in more downstream fouling as compared to PS. Hence, the larger difference between the height of energy barrier and the depth of secondary energy minimum favors more particle deposition at the secondary energy minimum. This difference is more significant in case of PS compared to SiO<sub>2</sub> which resulted in substantial downstream fouling while SiO<sub>2</sub> showed cake layer fouling only (Figure 4.11, 4.12 & 4.13). Moreover, less energy barrier for SiO<sub>2</sub> allowed more particles to deposit at the primary energy minimum which caused severe flux decline for SiO<sub>2</sub> compared to PS (Figure 4.6 & 4.8 (b)). This scenario is also analogous to the complete pore blocking model as described by various membrane researchers<sup>91, 109, 192, 226, 244, 245</sup>. As the theoretical aspect for colloidal fouling at pore scale is beyond the scope of this study we restrict our discussion in experimental observation and empirical relations only. The quantitative analysis for the release of particles from cake layer to downstream fouling needs further investigations in the future. In conclusion, reversible attachment of particles in the secondary energy minimum can alter the fouling behavior in an MMM device significantly from a cake layer to a downstream fouling.

## 4.5 Conclusion

In this study we have observed different fouling behavior of two colloidal foulants (PS and SiO<sub>2</sub>) for similar chemical conditions in dead-end filtrations using an MMM device. Cake layer fouling was observed for SiO<sub>2</sub> and cake layer with downstream fouling was observed for PS particles. MF filtration flux was declined more with increasing ionic strength as a result of increased

fouling. The interaction energy between the membrane–foulant and foulant–foulant were calculated from contact angle measurement using XDLVO theory. Increasing molar concentration decreased the height of energy barrier and increased the depth of secondary energy minimum. Microfluidic fouling results agreed well with XDLVO calculations of energy. The back-washing experiments showed water channel formation alleviated the release of PS particle from the cake layer at lower pressure while no water channel formation was noticed through SiO<sub>2</sub> cake layer even at maximum pressure.

# Chapter 5

Conclusion & future work!

---

<sup>1</sup> A part of the materials of this chapter has been published in “N. Debnath and M. Sadrzadeh, “Microfluidic mimic for colloid membrane filtration: a review”, Journal of the Indian Institute of Science, Vol. 98, I. 2, p. 137-157, 2018.”

## 5.1 Conclusion

In this dissertation, at first, an overview of the connections between membrane technology and microfluidic filtration has been provided. A special focus is made on the application of microfluidic membrane filtration devices for investigating the colloidal fouling. Applying a massive variety of fabrication methods, microfluidic membrane filtration devices can be scalable and designed for specific applications, such as separation of colloids, organic matter, and biological substances from wastewaters. Furthermore, using a microfluidic membrane filtration device, the internal surface can be exploited for investigating the fouling dynamics and morphology, intermolecular interactions, and transport mechanisms at the pore scale.

In Chapter 2, a microfluidic filtration device (pillar gap  $25\mu\text{m}$ ) has been developed to observe and analyze the fouling formation for constant flow rate filtration. The fouling experiments resulted in a slender string-like structure formation as colloidal streamer when polystyrene and polyacrylamide were introduced together into the micro-chip. For neutral pH conditions, streamer formation was observed when the mass flow rate of PS solution was equal to or greater than 0.6 times that of the PAM solution. The detailed of the flow regime under which the streamer formation occurred was quantified in a state diagram. We also showed that the streamer formation was caused by floc formation, and the floc formation was the result of electrostatic effects. However, further investigation of the colloidal streamer is crucial for the future to reveal more information about particle-laden complex flows in a microfluidic device.

In Chapter 3, the colloidal fouling phenomena have been investigated using an MMM device with a reduced pillar gap to  $2\mu\text{m}$ . The developed MMM device could mimic the pore size of a microfiltration membrane and was used as a dead-end filtration membrane module to observe real-time fouling formation at pore scale. A systematic study has been performed by varying the

hydrodynamic conditions (flux, pressure, flow rate) and solution chemistry to investigate colloidal (with PS), organic (with PAM), and combined fouling (with PS+PAM), separately. Fouling formation is categorized into four major types: cake filtration at upstream (by PS), pore fouling at pores (by PAM), downstream colloidal aggregation (PS at high pressure) and colloidal streamer formation (PS+PAM at high pressure). Constant-pressure experiments showed severe flux decline due to downstream fouling at higher pressures. Similar to the ex-situ membrane filtration, combined fouling resulted in more severe flux decline than individual fouling.

In Chapter 4, interaction energies of all components contributing to fouling were calculated and used for rationalizing different types of fouling phenomena. Comparing the fouling scenarios by SiO<sub>2</sub> and PS at the same hydrodynamic condition, we found that SiO<sub>2</sub> resulted in primarily cake layer formation, while PS particles showed cake layer formation along with significant downstream fouling. Fouling was increased by increasing molar concentration of salt in the synthetic wastewater solution, which also aligns well with increasing depth of secondary energy minimum. Another interesting finding was the increased fouling rate for SiO<sub>2</sub> as compared to PS at the same filtration condition. The XDLVO energy calculation revealed the reason was the lower cohesive energy between PS-PS than SiO<sub>2</sub>-SiO<sub>2</sub>. Also, primary and secondary water channel formation during back-washing for PS alleviated particle release from cake layer, which might be the cause of downstream fouling. Interestingly, no water channel and downstream fouling were observed in case of SiO<sub>2</sub> cake layer for back-washing at higher pressures.

## **5.2 Strengths and limitations**

Several challenges in understanding the transport and fouling mechanisms in porous membranes can be overcome using a microfluidic membrane filtration system. The general advantages of a

microfluidic devices include saving time, space, material and cost, better control of flow, and high-throughput. Microfluidic membrane filtration devices, with the flexible design of the microchips, can be utilized for separation, purification, and concentration studies at micron-scale. Microfluidic membrane chips enable creating defect-free porous surfaces with homogeneous properties that can be operated in a continuous and uniform-flow filtration process. These devices are highly efficient as one can have more control over time, size, and experimental parameters, as well as the flow hydrodynamics. Given that, these devices have been used for many industrial applications to improve separation efficiency and material properties.

To fabricate a microfluidic membrane filtration system, the selection of proper material for the intended application is critical. Several studies have shown promising results using PDMS microfluidic membranes in colloid filtration and fouling investigations, as discussed earlier. The PDMS microchip has several advantages such as low toxicity, elasticity, chemical inertness, strong gas permeability, and low cost. The use of a PDMS microchip is, however, limited by the aging of material, poor chemical compatibility, the absorbance of small molecules and water vapor generation inside a microchip.

Several challenges and limitations can be encountered using microfluidic colloid membrane filtration. The first and foremost challenge is the fabrication of microchips with the scaling comparable with the pores of typical porous membranes. The conventional photolithography technique, as the most common microfabrication method, can be employed for the fabrication of the smallest feature sizes of  $0.5\mu\text{m}$ . This size range is highly comparable to an MF membrane pore size ( $0.1\mu\text{m}$ - $10\mu\text{m}$ ). E-beam photolithography techniques can go down to  $10\text{nm}$  as the smallest feature size, but it is more expensive than microfabrication. Therefore, new techniques are required to fill the gap between the properties of a microfluidic membrane and a real

membrane. Second challenge is that it is hard to observe fouling at the downstream side in a dead-end microfiltration for commercial membrane. In general, a membrane is consisting a top dense skin layer and a porous support layer beneath the skin layer with fingerlike macrovoids or microvoids. Our MMM device thickness (pillar area) is comparable to the top dense skin layer zone while the porous support layer can be comparable to the downstream zone. For many membrane literature<sup>246-248</sup>, the observation of fouling at this porous support layer downstream location is either unnoticed or ignored as this was not their primary focus of study. However, we can not completely neglect the downstream fouling phenomena for membrane filtration as it has significant contribution to the overall membrane fouling. We look forward to more detailed pore-scale and locational fouling (upstream, pore, downstream) analysis through entire membrane thickness in the future. Finally, microfluidic membrane mimic can be used to study biofouling; however, the dynamic nature and the viscoelastic behavior of the active components like bacteria, make the analysis more complicated. Hence, the efficiency of this system needs to be fully understood, primarily, in the case of soft, deformable and permeable colloids.

Another limitation can be the limited use of PDMS material in MF membrane filtration. Based on the outstanding advantages of PDMS, such as chemical inertness, gas permeability, mechanical properties, optical transparency, PDMS is mostly used in nanomembranes and micro/nanofluidic systems. Various methods as listed in the first chapter such as conventional photolithography, soft lithography, electron beam lithography, micromachining are extensively used for through-hole microfiltration studies. However, PDMS is not popular for microfiltration membrane fabrication<sup>249</sup>.

### 5.3 Future work

Microfluidic membrane filtration device opens up many future opportunities. This device can be used as a model system to investigate certain phenomena under physiologically significant conditions that are limited by traditional filtration techniques. For example, the microfluidic device has been used to mimic components of the liver<sup>250</sup>, lung<sup>251</sup>, and heart<sup>252, 253</sup>. Microfluidic membrane mimic may offer key micro-environmental conditions revealing more information about organ functions<sup>254</sup> and vascular circulations<sup>255</sup>. Thus, microfluidic membrane mimic can serve as an ideal model system for future biomedical research.

Another example would be to utilize the benefits of selectivity of a membrane on-chip. As compared to the conventional filtration processes, a microfluidic membrane mimic better protects the microchannel from particulate matter, reduces the unwanted hydrodynamic flow, and has more control over sample volume. This device may offer selective separation of liquids in pervaporation, selective removal of one component from a gas mixture, which further needs to be investigated.

The membrane-less MF can be explored in many aspects. For example, lipid bilayers production was limited to the fabrication in an array format, which can be further explored for pillar shape or different geometry. In addition, future work is clearly required to achieve a quantitative description of lipid bilayer formation process and the role of media compositions.

Lastly, the theoretical aspects for the complete understanding of cake layer, pore fouling, downstream colloidal aggregation and streamer fouling can be explored further. The theoretical part of surface interactions as discussed in the 1<sup>st</sup> chapter (Section 1.3.1) play an important role in understanding fouling layer formation and also on its control using the critical flux concepts<sup>185</sup>. But the major discrepancy between the theory/simulation and experimental results

arises due to the fact that the theoretical modelling and numerical simulation does not consider the concept of multi-body interactions for colloidal interactions. Also, the membrane surface is often represented as a homogeneous surface thus neglecting the phenomena occurring at the pore-scale. In this regard, microfluidic/MMM devices allow in-situ fouling observation and systematic experiments with well-defined geometry, controlled hydrodynamic and chemical conditions. The present work illustrates experimental observations and empirical relations of different hydrodynamic and chemical conditioning with various fouling formation (cake layer, pore fouling, downstream colloidal aggregation and streamer fouling) at pore-scale. Future progress in modelling and understanding these fouling mechanisms would be the essential first step in controlling fouling of real porous materials such as membrane<sup>91</sup>.

In conclusion, microfluidic membrane mimic provides an inexpensive and reliable platform that can add benefits to the microfluidic research from membrane perspective and vice-versa through making a bridge between microfluidics and membrane technology. Colloidal fouling studies in chapters 2, 3, and 4 can be extended to a new threshold by using a microfluidic membrane mimic device to mitigate membrane fouling, which is a hoped-for goal in membrane science and technology.

## **5.4 List of contributions**

The outcome of this research is published/ready for submission, and presented in the following journals and conference proceedings.

### **5.4.1 Journal papers**

1. N. Debnath, M. Hassanpourfard, R. Ghosh, J. Trivedi, T. Thundat, M. Sadrzadeh & A.

- Kumar, “Abiotic streamers in a microfluidic system”, *Soft Matter*, Vol. 13, I. 46, p. 8698-8705, 2017.
2. N. Debnath and M. Sadrzadeh, “Microfluidic mimic for colloid membrane filtration: a review”, *Journal of the Indian Institute of Science*, Vol. 98, I. 2, p. 137-157, 2018.
  3. N. Debnath, A. Kumar, T. Thundat and M. Sadrzadeh, “Investigating fouling at the pore-scale using a microfluidic membrane mimic filtration system”, *Scientific Reports*, Vol. 9, I. 1, p. 10587, 2019.
  4. N. Debnath, A. Kumar, T. Thundat and M. Sadrzadeh, “Role of secondary energy minimum in microfluidic membrane fouling”, *Journal of Colloids and Interface Science*, 2019 (Ready for submission).

#### **5.4.2 Conference presentation**

1. N. Debnath, M. Hassanpourfard, R. Ghosh, T. Thundat, A. Kumar, “Flow induced streamer formation in particle laden complex flows”, 69th Annual Meeting of American Physical Society Division of Fluid Dynamics (APS DFD), November 19-21, 2016, Portland, Oregon, USA.
2. N. Debnath, A. Kumar, T. Thundat, M. Sadrzadeh, “Microscopic membrane fouling characterization”, Annual conference of North American Membrane Society (NAMS), May 11-15, 2019, Pittsburgh, Pennsylvania, USA.

## References

1. M. A. Montgomery and M. Elimelech, Water and sanitation in developing countries: Including health in the equation - Millions suffer from preventable illnesses and die every year, *Environmental Science and Technology* **41**, 17–24 (2007).
2. M. A. Shannon, P. W. Bohn, M. Elimelech, J. G. Georgiadis, B. J. Marñas, and A. M. Mayes, Science and technology for water purification in the coming decades, *Nature* **452**, 301–310 (2008).
3. M. Sadrzadeh, J. Hajinasiri, S. Bhattacharjee, and D. Pernitsky, Nanofiltration of oil sands boiler feed water: Effect of pH on water flux and organic and dissolved solid rejection, *Separation and Purification Technology* **141**, 339–353 (2015).
4. N. L. Le and S. P. Nunes, Materials and membrane technologies for water and energy sustainability, *Sustainable Materials and Technologies* **7**, 1–28 (2016).
5. M. R. Wiesner, J. Hackney, S. Sethi, J. G. Jacangelo, J. G. Jacangelo, and J. Lafne, Cost estimates for membrane filtration and conventional treatment for membrane filtration and conventional treatment alternative for the removal of particles and organic material, *American Water Works Association* **86**, 33–41 (1994).
6. B. Van der Bruggen, *Membrane Technology and application*, (2017).
7. M. Mulder, *Basic Principles of Membrane Technology*, (1996).
8. W. Guo, H. H. Ngo, and J. Li, A mini-review on membrane fouling, *Bioresource Technology* **122**, 27–34 (2012).
9. M. A. Al Mamun, M. Sadrzadeh, R. Chatterjee, S. Bhattacharjee, and S. De, Colloidal fouling of nanofiltration membranes: A novel transient electrokinetic model and experimental study, *Chemical Engineering Science* **138**, 153–163 (2015).

10. V. Chen, A. G. Fane, S. Madaeni, and I. G. Wenten, Particle deposition during membrane filtration of colloids: Transition between concentration polarization and cake formation, *Journal of Membrane Science* **125**, 109–122 (1997).
11. D. Mark, S. Haeberle, G. Roth, F. Von Stetten, and R. Zengerle, Microfluidic lab-on-a-chip platforms: Requirements, characteristics and applications, *NATO Science for Peace and Security Series A: Chemistry and Biology* 305–376 (2010).doi:10.1007/978-90-481-9029-4-17
12. S. Haeberle, D. Mark, F. Von Stetten, and R. Zengerle, Microfluidic platforms for lab-on-a-chip applications, *Microsystems and Nanotechnology* **9783642182**, 853–895 (2012).
13. T. Salafi, K. K. Zeming, and Y. Zhang, Advancements in microfluidics for nanoparticle separation, *Lab Chip* **17**, 11–33 (2017).
14. J. Alvankarian and B. Y. Majlis, Tunable microfluidic devices for hydrodynamic fractionation of cells and beads: A review, *Sensors (Switzerland)* **15**, 29685–29701 (2015).
15. E. Ng, K. Chen, A. Hang, A. Syed, and J. X. J. Zhang, Multi-Dimensional Nanostructures for Microfluidic Screening of Biomarkers: From Molecular Separation to Cancer Cell Detection, *Annals of Biomedical Engineering* **44**, 847–862 (2016).
16. P. Gruber, M. P. C. Marques, N. Szita, and T. Mayr, Integration and application of optical chemical sensors in microbioreactors, *Lab Chip* **17**, 2693–2712 (2017).
17. Z. Hugh Fan, Chemical Sensors and Microfluidics, *Journal of Biosensors & Bioelectronics* **04**, 1–2 (2013).
18. S. G. Anema, The use of “lab-on-a-chip” microfluidic SDS electrophoresis technology for the separation and quantification of milk proteins, *International Dairy Journal* **19**, 198–

- 204 (2009).
19. K. D. Dorfman, S. B. King, D. W. Olson, J. D. P. Thomas, and D. R. Tree, Beyond gel electrophoresis: Microfluidic separations, fluorescence burst analysis, and DNA stretching, *Chemical Reviews* **113**, 2584–2667 (2013).
  20. J. H. Tsai and L. Lin, A thermal-bubble-actuated micronozzle-diffuser pump, *Journal of Microelectromechanical Systems* **11**, 665–671 (2002).
  21. C. Zhang, D. Xing, and Y. Li, Micropumps, microvalves, and micromixers within PCR microfluidic chips: Advances and trends, *Biotechnology Advances* **25**, 483–514 (2007).
  22. K. Ren, W. Dai, J. Zhou, J. Su, and H. Wu, Whole-Teflon microfluidic chips, *Proceedings of the National Academy of Sciences* **108**, 8162–8166 (2011).
  23. K. M. Horsman, J. M. Bienvenue, K. R. Blasier, and J. P. Landers, Forensic DNA analysis on microfluidic devices: A review, *Journal of Forensic Sciences* **52**, 784–799 (2007).
  24. J. Khandurina, T. E. McKnight, S. C. Jacobson, L. C. Waters, R. S. Foote, and J. M. Ramsey, Integrated system for rapid PCR-based DNA analysis in microfluidic devices, *Analytical Chemistry* **72**, 2995–3000 (2000).
  25. J. de Jong, R. G. H. Lammertink, and M. Wessling, Membranes and microfluidics: a review, *Lab on a Chip* **6**, 1125 (2006).
  26. X. Chen and J. Shen, Review of membranes in microfluidics, *Journal of Chemical Technology and Biotechnology* **92**, 271–282 (2017).
  27. X. Chen, J. Shen, Z. Hu, and X. Huo, Manufacturing methods and applications of membranes in microfluidics, *Biomedical Microdevices* **18** (2016).
  28. E. K. Sackmann, A. L. Fulton, and D. J. Beebe, The present and future role of microfluidics in biomedical research, *Nature* **507**, 181–189 (2014).

29. D. T. Chiu, A. J. deMello, D. Di Carlo, P. S. Doyle, C. Hansen, R. M. Maceiczky, and R. C. R. Wootton, Small but Perfectly Formed? Successes, Challenges, and Opportunities for Microfluidics in the Chemical and Biological Sciences, *Chem* **2**, 201–223 (2017).
30. J. Zhang, S. Yan, D. Yuan, G. Alici, N.-T. Nguyen, M. Ebrahimi Warkiani, and W. Li, Fundamentals and applications of inertial microfluidics: a review, *Lab Chip* **16**, 10–34 (2016).
31. J. M. K. Ng, I. Gitlin, A. D. Stroock, and G. M. Whitesides, Components for integrated poly(dimethylsiloxane) microfluidic systems, *Electrophoresis* **23**, 3461–3473 (2002).
32. A. D. Stroock and G. M. Whitesides, Components for integrated poly (dimethylsiloxane) microfluidic systems, *Electrophoresis* **23**, 3461–3473 (2002).
33. L. Mou and X. Jiang, Materials for Microfluidic Immunoassays: A Review, *Advanced Healthcare Materials* **6**, 1–20 (2017).
34. H. Bruus, Theoretical microfluidics, *Physics* **18**, 363 (2008).
35. C. Iliescu, H. Taylor, M. Avram, J. Miao, and S. Franssila, A practical guide for the fabrication of microfluidic devices using glass and silicon, *Biomicrofluidics* **6**, 16505–1650516 (2012).
36. D. Sticker, M. Rothbauer, S. Lechner, M.-T. Hehenberger, and P. Ertl, Multi-layered, membrane-integrated microfluidics based on replica molding of a thiol–ene epoxy thermoset for organ-on-a-chip applications, *Lab Chip* **15**, 4542–4554 (2015).
37. H. Wei, B. Chueh, H. Wu, E. W. Hall, C. Li, R. Schirhagl, J.-M. Lin, and R. N. Zare, Particle sorting using a porous membrane in a microfluidic device, *Lab Chip* **11**, 238–245 (2011).
38. Y. Cheng, Y. Wang, Z. Ma, W. Wang, and X. Ye, A bubble- and clogging-free

- microfluidic particle separation platform with multi-filtration, *Lab Chip* **16**, 4517–4526 (2016).
39. S.-I. Ohira and K. Toda, Micro gas analysis system for measurement of atmospheric hydrogen sulfide and sulfur dioxide., *Lab on a chip* **5**, 1374–1379 (2005).
  40. H. Di, G. J. O. Martin, and D. E. Dunstan, A microfluidic system for studying particle deposition during ultrafiltration, *Journal of Membrane Science* **532**, 68–75 (2017).
  41. L. G. Liang, M. Q. Kong, S. Zhou, Y. F. Sheng, P. Wang, T. Yu, F. Inci, W. P. Kuo, L. J. Li, U. Demirci, and S. Q. Wang, An integrated double-filtration microfluidic device for isolation, enrichment and quantification of urinary extracellular vesicles for detection of bladder cancer, *Scientific Reports* **7**, 1–10 (2017).
  42. L. Chen, M. E. Warkiani, H. B. Liu, and H. Q. Gong, Polymeric micro-filter manufactured by a dissolving mold technique, *Journal of Micromechanics and Microengineering* **20** (2010).
  43. J. R. Anderson, D. T. Chiu, R. J. Jackman, O. Chmiavskaya, J. C. McDonald, H. Wu, S. H. Whitesides, and G. M. Whitesides, Fabrication of topologically complex three-dimensional microfluidic systems in PDMS by rapid prototyping, *Analytical Chemistry* **72**, 3158–3164 (2000).
  44. J. Xu, R. Vaillant, and D. Attinger, Use of a porous membrane for gas bubble removal in microfluidic channels: Physical mechanisms and design criteria, *Microfluidics and Nanofluidics* **9**, 765–772 (2010).
  45. N. Sundararajan, Authors contributed equ, D. Kim, Current address: Department of B, and A. a. Berlin, Microfluidic operations using deformable polymer membranes fabricated by single layer soft lithography, *Lab on a Chip* **5**, 350 (2005).

46. A. P. Russo, S. T. Retterer, A. J. Spence, M. S. Isaacson, L. a. Lepak, M. G. Spencer, D. L. Martin, R. MacColl, and J. N. Turner, Direct casting of polymer membranes into microfluidic devices, *Separation Science and Technology* **39**, 2515–2530 (2004).
47. Z. X. Cai, Q. Fang, H. W. Chen, and Z. L. Fang, A microfluidic chip based liquid-liquid extraction system with microporous membrane, *Analytica Chimica Acta* **556**, 151–156 (2006).
48. P. C. Wang, J. Gao, and C. S. Lee, High-resolution chiral separation using microfluidics-based membrane chromatography, *Journal of Chromatography A* **942**, 115–122 (2002).
49. S. D. Noblitt, J. R. Kraly, J. M. VanBuren, S. V. Hering, J. L. Collett, and C. S. Henry, Integrated membrane filters for minimizing hydrodynamic flow and filtering in microfluidic devices, *Analytical Chemistry* **79**, 6249–6254 (2007).
50. S. Metz, C. Trautmann, a. Bertsch, and P. Renaud, Polyimide microfluidic devices with integrated nanoporous filtration areas manufactured by micromachining and ion track technology, *Journal of Micromechanics and Microengineering* **14**, 324–331 (2004).
51. J. S. Paustian, R. N. Azevedo, S. T. B. Lundin, M. J. Gilkey, and T. M. Squires, Microfluidic microdialysis: Spatiotemporal control over solution microenvironments using integrated hydrogel membrane microwindows, *Physical Review X* **3**, 1–13 (2014).
52. E. Choi and J. Park, in-Situ Formation of Hydrogel Membranes and Growth of Colloidal Crystals in Microchannels Using One Step Stamping, *Life Sciences* 236–238 (2011).
53. I. S. Ngene, R. G. H. Lammertink, M. Wessling, and W. van der Meer, A microfluidic membrane chip for in situ fouling characterization, *Journal of Membrane Science* **346**, 202–207 (2010).
54. P. Galambos, K. Zavadil, R. Shul, C. G. Willison, and S. Miller, Silicon nitride

- membranes for filtration and separation, *Microfluidic Devices and Systems II* **3877**, 273–283 (1999).
55. T. Leichlé and D. Bourrier, Integration of lateral porous silicon membranes into planar microfluidics, *Lab Chip* **15**, 833–838 (2015).
  56. Y. S. S. Wan, J. L. H. Chau, A. Gavriilidis, and K. L. Yeung, Design and fabrication of zeolite-based microreactors and membrane microseparators, *Microporous and Mesoporous Materials* **42**, 157–175 (2001).
  57. J. L. H. Chau, Y. S. S. Wan, A. Gavriilidis, and K. L. Yeung, Incorporating zeolites in microchemical systems, *Chemical Engineering Journal* **88**, 187–200 (2002).
  58. C. S. Toh, B. M. Kayes, E. J. Nemanick, and N. S. Lewis, Fabrication of free-standing nanoscale alumina membranes with controllable pore aspect ratios, *Nano Letters* **4**, 767–770 (2004).
  59. Z. Bin Liu, Y. Zhang, J. J. Yu, A. F. T. Mak, Y. Li, and M. Yang, A microfluidic chip with poly(ethylene glycol) hydrogel microarray on nanoporous alumina membrane for cell patterning and drug testing, *Sensors and Actuators, B: Chemical* **143**, 776–783 (2010).
  60. Y. Lu, W. Shi, J. Qin, and B. Lin, Fabrication and characterization of paper-based microfluidics prepared in nitrocellulose membrane by Wax printing, *Analytical Chemistry* **82**, 329–335 (2010).
  61. X. Fan, C. Jia, J. Yang, G. Li, H. Mao, Q. Jin, and J. Zhao, A microfluidic chip integrated with a high-density PDMS-based microfiltration membrane for rapid isolation and detection of circulating tumor cells, *Biosensors and Bioelectronics* **71**, 380–386 (2015).
  62. X. Li, W. Chen, G. Liu, W. Lu, and J. Fu, Continuous-flow microfluidic blood cell sorting for unprocessed whole blood using surface-micromachined microfiltration membranes,

- Lab Chip* **14**, 2565–2575 (2014).
63. M. E. Warkiani, F. Wicaksana, A. G. Fane, and H. Q. Gong, Investigation of membrane fouling at the microscale using isopore filters, *Microfluidics and Nanofluidics* **19**, 307–315 (2015).
  64. W. Chen, R. H. W. Lam, and J. Fu, Photolithographic surface micromachining of polydimethylsiloxane (PDMS), *Lab Chip* **12**, 391–395 (2012).
  65. Y. Yoon, S. Kim, J. Lee, J. Choi, R. K. Kim, S. J. Lee, O. Sul, and S. B. Lee, Clogging-free microfluidics for continuous size-based separation of microparticles, *Scientific Reports* **6**, 1–8 (2016).
  66. X. Chen, D. F. Cui, C. C. Liu, and H. Li, Microfluidic chip for blood cell separation and collection based on crossflow filtration, *Sensors and Actuators, B: Chemical* **130**, 216–221 (2008).
  67. A. Marty, C. Causserand, C. Roques, and P. Bacchin, Impact of tortuous flow on bacteria streamer development in microfluidic system during filtration, *Biomicrofluidics* **8**, 1–12 (2014).
  68. T. Robinson, P. Kuhn, K. Eyer, and P. S. Dittrich, Microfluidic trapping of giant unilamellar vesicles to study transport through a membrane pore, *Biomicrofluidics* **7** (2013).
  69. J. Seo, M. H. Lean, and A. Kole, Membrane-free microfiltration by asymmetric inertial migration, *Applied Physics Letters* **91** (2007).
  70. M. E. Warkiani, A. K. P. Tay, G. Guan, and J. Han, Membrane-less microfiltration using inertial microfluidics, *Scientific Reports* **5**, 1–10 (2015).
  71. S. Shin, O. Shardt, P. B. Warren, and H. a. Stone, Membraneless water filtration using

- CO<sub>2</sub>, *Nature Communications* **8**, 1–6 (2017).
72. T. Kwon, H. Prentice, J. De Oliveira, N. Madziva, M. E. Warkiani, J. F. P. Hamel, and J. Han, Microfluidic Cell Retention Device for Perfusion of Mammalian Suspension Culture, *Scientific Reports* **7**, 1–11 (2017).
  73. T. Maruyama, H. Matsushita, J. I. Uchida, F. Kubota, N. Kamiya, and M. Goto, Liquid membrane operations in a microfluidic device for separation of metal ions, *Analytical Chemistry* **76**, 4495–4500 (2004).
  74. J. R. SooHoo and G. M. Walker, Microfluidic aqueous two phase system for leukocyte concentration from whole blood, *Biomedical Microdevices* **11**, 323–329 (2009).
  75. M. Surmeian, M. N. Slyadnev, H. Hisamoto, A. Hibara, K. Uchiyama, and T. Kitamori, Three-layer flow membrane system on a microchip for investigation of molecular transport, *Analytical Chemistry* **74**, 2014–2020 (2002).
  76. K. Sato, A. Hibara, M. Tokeshi, H. Hisamoto, and T. Kitamori, Microchip-based chemical and biochemical analysis systems, *Advanced Drug Delivery Reviews* **55**, 379–391 (2003).
  77. M. Surmeian, M. N. Slyadnev, H. Hisamoto, A. Hibara, K. Uchiyama, and T. Kitamori, Three-layer flow membrane system on a microchip for investigation of molecular transport, *Analytical Chemistry* **74**, 2014–2020 (2002).
  78. I. Reviakine and A. Brisson, Formation of supported phospholipid bilayers from unilamellar vesicles investigated by atomic force microscopy, *Langmuir* **16**, 1806–1815 (2000).
  79. N. Malmstadt, M. A. Nash, R. F. Purnell, and J. J. Schmidt, Automated formation of lipid-bilayer membranes in a microfluidic device, *Nano Letters* **6**, 1961–1965 (2006).
  80. E. T. Castellana and P. S. Cremer, Solid supported lipid bilayers: From biophysical studies

- to sensor design, *Surface Science Reports* **61**, 429–444 (2006).
81. R. Watanabe, N. Soga, T. Yamanaka, and H. Noji, High-throughput formation of lipid bilayer membrane arrays with an asymmetric lipid composition, *Scientific Reports* **4**, 1–6 (2014).
  82. S. Ota, H. Suzuki, and S. Takeuchi, Microfluidic lipid membrane formation on microchamber arrays, *Lab on a Chip* **11**, 2485 (2011).
  83. M. E. Sandison and H. Morgan, Rapid fabrication of polymer microfluidic systems for the production of artificial lipid bilayers, *Journal of Micromechanics and Microengineering* **15**, 139–144 (2005).
  84. A. Hirano-Iwata, K. Aoto, A. Oshima, T. Taira, R. T. Yamaguchi, Y. Kimura, and M. Niwano, Free-standing lipid bilayers in silicon chips-membrane stabilization based on microfabricated apertures with a nanometer-scale smoothness, *Langmuir* **26**, 1949–1952 (2010).
  85. I. F. J. Vankelecom, D. Depre, S. De Beukelaer, and J. B. Uytterhoeven, Influence of zeolites in PDMS membranes. Pervaporation of water/alcohol mixtures, *Journal of physical chemistry* **99**, 13193–13197 (1995).
  86. K. B. Neeves and S. L. Diamond, A membrane-based microfluidic device for controlling the flux of platelet agonists into flowing blood, *Lab on a Chip* **8**, 701 (2008).
  87. S. Thorslund, O. Klett, F. Nikolajeff, K. Markides, and J. Bergquist, A hybrid poly(dimethylsiloxane) microsystem for on-chip whole blood filtration optimized for steroid screening, *Biomedical Microdevices* **8**, 73–79 (2006).
  88. R. T. Davies, J. Kim, S. C. Jang, E.-J. Choi, Y. S. Gho, and J. Park, Microfluidic filtration system to isolate extracellular vesicles from blood, *Lab on a Chip* **12**, 5202 (2012).

89. P. Bacchin, Q. Derekx, D. Veyret, K. Glucina, and P. Moulin, Clogging of microporous channels networks: Role of connectivity and tortuosity, *Microfluidics and Nanofluidics* **17**, 85–96 (2014).
90. J. Linkhorst, T. Beckmann, D. Go, A. J. C. Kuehne, and M. Wessling, Microfluidic colloid filtration, *Scientific Reports* **6**, 1–8 (2016).
91. P. Bacchin, a. Marty, P. Duru, M. Meireles, and P. Aimar, Colloidal surface interactions and membrane fouling: Investigations at pore scale, *Advances in Colloid and Interface Science* **164**, 2–11 (2011).
92. K. Hylton and S. Mitra, A microfluidic hollow fiber membrane extractor for arsenic(V) detection, *Analytica Chimica Acta* **607**, 45–49 (2008).
93. D. E. Angelescu, B. Mercier, D. Sless, and R. Schroetter, Microfluidic capillary separation and real-time spectroscopic analysis of specific components from multiphase mixtures, *Analytical Chemistry* **82**, 2412–2420 (2010).
94. S. Feng, M. N. Nguyen, and D. W. Inglis, Microfluidic droplet extraction by hydrophilic membrane, *Micromachines* **8**, 1–8 (2017).
95. D. R. Gossett, W. M. Weaver, A. J. MacH, S. C. Hur, H. T. K. Tse, W. Lee, H. Amini, and D. Di Carlo, Label-free cell separation and sorting in microfluidic systems, *Analytical and Bioanalytical Chemistry* **397**, 3249–3267 (2010).
96. J. Gao, J. Xu, L. E. Locascio, and C. S. Lee, Integrated microfluidic system enabling protein digestion, peptide separation, and protein identification, *Analytical Chemistry* **73**, 2648–2655 (2001).
97. Y. Jiang and C. S. Lee, On-line coupling of micro-enzyme reactor with micro-membrane chromatography for protein digestion, peptide separation, and protein identification using

- electrospray ionization mass spectrometry, *Journal of Chromatography A* **924**, 315–322 (2001).
98. J. Khandurina, T. E. McKnight, S. C. Jacobson, L. C. Waters, R. S. Foote, and J. M. Ramsey, Integrated system for rapid PCR-based DNA analysis in microfluidic devices, *Analytical Chemistry* **72**, 2995–3000 (2000).
  99. C. Liu, J. a. Thompson, and H. H. Bau, A membrane-based, high-efficiency, microfluidic debubbler, *Lab on a Chip* **11**, 1688 (2011).
  100. J. de Jong, B. Ankoné, R. G. H. Lammertink, and M. Wessling, New replication technique for the fabrication of thin polymeric microfluidic devices with tunable porosity, *Lab on a Chip* **5**, 1240 (2005).
  101. Y. Cheng, Y. Wang, Z. Ma, W. Wang, and X. Ye, A bubble- and clogging-free microfluidic particle separation platform with multi-filtration, *Lab on a Chip* **16**, 4517–4526 (2016).
  102. B. H. Chueh, D. Huh, C. R. Kyrtos, T. Houssin, N. Futai, and S. Takayama, Leakage-free bonding of porous membranes into layered microfluidic array systems, *Analytical Chemistry* **79**, 3504–3508 (2007).
  103. M. H. Pham and D. P. J. Barz, Bonding Nafion® with polydimethylsiloxane: A versatile approach towards ion-exchange membrane microfluidic devices, *Journal of Membrane Science* **537**, 310–314 (2017).
  104. D. S. Peterson, Solid supports for micro analytical systems., *Lab on a chip* **5**, 132–139 (2005).
  105. R. Devendra and G. Drazer, Deterministic fractionation of binary suspensions moving past a line of microposts, *Microfluidics and Nanofluidics* **17**, 519–526 (2014).

106. I. Biswas, R. Ghosh, M. Sadrzadeh, and A. Kumar, Nonlinear deformation and localized failure of bacterial streamers in creeping flows, *Scientific Reports* **6**, 2–11 (2016).
107. J. Alvankarian, A. Bahadorimehr, and B. Yeop Majlis, A pillar-based microfilter for isolation of white blood cells on elastomeric substrate, *Biomicrofluidics* **7**, 1–16 (2013).
108. C. Y. Tang, T. H. Chong, and A. G. Fane, Colloidal interactions and fouling of NF and RO membranes: A review, *Advances in Colloid and Interface Science* **164**, 126–143 (2011).
109. E. Iritani, A Review on Modeling of Pore-Blocking Behaviors of Membranes During Pressurized Membrane Filtration, *Drying Technology* **31**, 146–162 (2013).
110. Z. B. Sendekie and P. Bacchin, Colloidal Jamming Dynamics in Microchannel Bottlenecks, *Langmuir* **32**, 1478–1488 (2016).
111. I. S. Ngene, R. G. H. Lammertink, M. Wessling, and W. van der Meer, A microfluidic membrane chip for in situ fouling characterization, *Journal of Membrane Science* **346**, 202–207 (2010).
112. W. Gao, H. Liang, J. Ma, M. Han, Z. lin Chen, Z. shuang Han, and G. bai Li, Membrane fouling control in ultrafiltration technology for drinking water production: A review, *Desalination* **272**, 1–8 (2011).
113. C. Likos, *Effective interactions in soft condensed matter physics*, (2001).
114. K. M. Yao, M. T. Habibian, and C. R. O'Melia, Water and Waste Water Filtration: Concepts and Applications, *Environmental Science and Technology* **5**, 1105–1112 (1971).
115. N. Tufenkji and M. Elimelech, Breakdown of colloid filtration theory: Role of the secondary energy minimum and surface charge heterogeneities, *Langmuir* **21**, 841–852 (2005).

116. N. Tufenkji and M. Elimelech, Deviation from the classical colloid filtration theory in the presence of repulsive DLVO interactions, *Langmuir* **20**, 10818–10828 (2004).
117. E. M. V Hoek, S. Bhattacharjee, and M. Elimelech, Effect of membrane surface roughness on colloid-membrane DLVO interactions, *Langmuir* **19**, 4836–4847 (2003).
118. C. Van den Broeck, F. Lostak, and H. N. W. Lekkerkerker, The effect of direct interactions on Brownian diffusion, *The Journal of Chemical Physics* **74**, 2006–2010 (1981).
119. V. Ramachandran and H. S. Fogler, Multilayer Deposition of Stable Colloidal Particles during Flow within Cylindrical Pores, *Langmuir* **14**, 4435–4444 (1998).
120. K. V. Sharp and R. J. Adrian, On flow-blocking particle structures in microtubes, *Microfluidics and Nanofluidics* **1**, 376–380 (2005).
121. G. C. Agbangla, É. Climent, and P. Bacchin, Experimental investigation of pore clogging by microparticles: Evidence for a critical flux density of particle yielding arches and deposits, *Separation and Purification Technology* **101**, 42–48 (2012).
122. P. Bacchin, B. Espinasse, Y. Bessiere, D. F. Fletcher, and P. Aimar, Numerical simulation of colloidal dispersion filtration: description of critical flux and comparison with experimental results, *Desalination* **192**, 74–81 (2006).
123. Q. Derekx, P. Bacchin, D. Veyret, K. Glucina, and P. Moulin, Numerical and experimental study of fouling in microfluidic channels and microfiltration Membranes, *Procedia Engineering* **44**, 54–56 (2012).
124. W. P. Johnson and M. Hilpert, Upscaling colloid transport and retention under unfavorable conditions: Linking mass transfer to pore and grain topology, *Water Resources Research* **49**, 5328–5341 (2013).

125. V. V. Tarabara, I. Koyuncu, and M. R. Wiesner, Effect of hydrodynamics and solution ionic strength on permeate flux in cross-flow filtration: Direct experimental observation of filter cake cross-sections, *Journal of Membrane Science* **241**, 65–78 (2004).
126. H. Zhang, J. Gao, T. Jiang, D. Gao, S. Zhang, H. Li, and F. Yang, A novel approach to evaluate the permeability of cake layer during cross-flow filtration in the flocculants added membrane bioreactors, *Bioresource Technology* **102**, 11121–11131 (2011).
127. A. Marty, C. Roques, C. Causserand, and P. Bacchin, Formation of bacterial streamers during filtration in microfluidic systems, *Biofouling* **28**, 551–562 (2012).
128. N. Debnath, M. Hassanpourfard, R. Ghosh, J. Trivedi, T. Thundat, M. Sadrzadeh, and A. Kumar, Abiotic streamers in a microfluidic system, *Soft Matter* **13**, 8698–8705 (2017).
129. A. Karimi, D. Karig, A. Kumar, and A. M. Ardekani, Interplay of physical mechanisms and biofilm processes: review of microfluidic methods, *Lab Chip* **15**, 23–42 (2015).
130. A. Valiei, A. Kumar, P. P. Mukherjee, Y. Liu, and T. Thundat, A web of streamers: biofilm formation in a porous microfluidic device, *Lab on a Chip* **12**, 5133 (2012).
131. M. Hassanpourfard, Z. Nikakhtari, R. Ghosh, S. Das, T. Thundat, Y. Liu, and A. Kumar, Bacterial floc mediated rapid streamer formation in creeping flows, *Scientific Reports* **5**, 1–17 (2015).
132. M. Hassanpourfard, R. Ghosh, T. Thundat, and A. Kumar, Dynamics of bacterial streamers induced clogging in microfluidic devices, *Lab on a Chip* **16**, 4091–4096 (2016).
133. K. Drescher, Y. Shen, B. L. Bassler, and H. a Stone, Biofilm streamers cause catastrophic disruption of flow with consequences for environmental and medical systems., *Proceedings of the National Academy of Sciences of the United States of America* **110**, 4345–4350 (2013).

134. N. Debnath and M. Sadrzadeh, Microfluidic Mimic for Colloid Membrane Filtration: A Review, *Journal of the Indian Institute of Science* **98**, 137–157 (2018).
135. W. Guo, H. H. Ngo, and J. Li, A mini-review on membrane fouling, *Bioresource Technology* **122**, 27–34 (2012).
136. Y. S. Chen and S. S. Hsiau, Cake formation and growth in cake filtration, *Powder Technology* **192**, 217–224 (2009).
137. S. Hong, R. S. Faibish, and M. Elimelech, Kinetics of permeate flux decline in crossflow membrane filtration of colloidal suspensions, *Journal of Colloid and Interface Science* **196**, 267–277 (1997).
138. E. Matthiasson and B. Sivik, Concentration polarization and fouling, *Desalination* **35**, 59–103 (1980).
139. N. Lee, G. Amy, J. P. Croué, and H. Buisson, Identification and understanding of fouling in low-pressure membrane (MF/UF) filtration by natural organic matter (NOM), *Water Research* **38**, 4511–4523 (2004).
140. C. Visvanathan and R. Ben aim, Studies on colloidal membrane fouling mechanisms in crossflow microfiltration, *Journal of Membrane Science* **45**, 3–15 (1989).
141. H. Yamamura, K. Kimura, and Y. Watanabe, Mechanism involved in the evolution of physically irreversible fouling in microfiltration and ultrafiltration membranes used for drinking water treatment, *Environmental Science and Technology* **41**, 6789–6794 (2007).
142. C. M. C. Law, X. Y. Li, and Q. Li, The combined colloid-organic fouling on nanofiltration membrane for wastewater treatment and reuse, *Separation Science and Technology* **45**, 935–940 (2010).
143. Q. Li and M. Elimelech, Synergistic effects in combined fouling of a loose nanofiltration

- membrane by colloidal materials and natural organic matter, *Journal of Membrane Science* **278**, 72–82 (2006).
144. Y. Kim, M. Elimelech, H. K. Shon, and S. Hong, Combined organic and colloidal fouling in forward osmosis: Fouling reversibility and the role of applied pressure, *Journal of Membrane Science* **460**, 206–212 (2014).
  145. M. Xie, L. D. Nghiem, W. E. Price, and M. Elimelech, Impact of organic and colloidal fouling on trace organic contaminant rejection by forward osmosis: Role of initial permeate flux, *Desalination* **336**, 146–152 (2014).
  146. I. M. Griffiths, A. Kumar, and P. S. Stewart, A combined network model for membrane fouling, *Journal of Colloid and Interface Science* **432**, 10–18 (2014).
  147. C. C. Ho and A. L. Zydney, A combined pore blockage and cake filtration model for protein fouling during microfiltration, *Journal of Colloid and Interface Science* **232**, 389–399 (2000).
  148. A. N. Quay, T. Tong, S. M. Hashmi, Y. Zhou, S. Zhao, and M. Elimelech, Combined Organic Fouling and Inorganic Scaling in Reverse Osmosis: Role of Protein-Silica Interactions, *Environmental Science and Technology* **52**, 9145–9153 (2018).
  149. L. M. McDowell-boyer, J. R. Hunt, and N. Itar, Particle transport through porous media, *Water Resources Research* **22**, 1901–1921 (1986).
  150. S. K. Mohanty, J. E. Saiers, and J. N. Ryan, Colloid Mobilization in a Fractured Soil during Dry-Wet Cycles: Role of Drying Duration and Flow Path Permeability, *Environmental Science and Technology* **49**, 9100–9106 (2015).
  151. J. R. Lead and K. J. Wilkinson, 1. Environmental Colloids and Particlearticle: Current Knowledge and Future Developments, *Environmental Colloids and Particlearticle* (2007).

152. V. Kochkodan, D. J. Johnson, and N. Hilal, Polymeric membranes: Surface modification for minimizing (bio)colloidal fouling, *Advances in Colloid and Interface Science* **206**, 116–140 (2014).
153. M. Aghajani, M. Wang, L. M. Cox, J. P. Killgore, A. R. Greenberg, and Y. Ding, Influence of support-layer deformation on the intrinsic resistance of thin film composite membranes, *Journal of Membrane Science* **567**, 49–57 (2018).
154. M. Ranjbar, J. Rupp, G. Pusch, and R. Meyn, Quantification and optimization of viscoelastic effects of polymer solutions for enhanced oil recovery, *Eighth Symposium on Enhanced Oil Recovery* 521–531 (1992).doi:10.2523/24154-ms
155. T. R. Hoare and D. S. Kohane, Hydrogels in drug delivery: Progress and challenges, *Polymer* **49**, 1993–2007 (2008).
156. J. Hou, Z. Liu, S. Zhang, X. Yue, and J. Yang, The role of viscoelasticity of alkali/surfactant/polymer solutions in enhanced oil recovery, *Journal of Petroleum Science and Engineering* **47**, 219–235 (2005).
157. R. Tang, C. S. Kim, D. J. Solfiell, S. Rana, R. Mout, E. M. Velázquez-Delgado, A. Chompoosor, Y. Jeong, B. Yan, Z. J. Zhu, C. Kim, J. A. Hardy, and V. M. Rotello, Direct delivery of functional proteins and enzymes to the cytosol using nanoparticle-stabilized nanocapsules, *ACS Nano* **7**, 6667–6673 (2013).
158. A. Valiei, A. Kumar, P. P. Mukherjee, Y. Liu, and T. Thundat, A web of streamers: biofilm formation in a porous microfluidic device, *Lab on a Chip* **12**, 5133 (2012).
159. C. E. Stanley, G. Grossmann, X. Casadevall Solvas, and A. J. DeMello, Soil-on-a-Chip: Microfluidic platforms for environmental organismal studies, *Lab on a Chip* **16**, 228–241 (2016).

160. L. Campo-Deaño, F. J. Galindo-Rosales, F. T. Pinho, M. A. Alves, and M. S. N. Oliveira, Nanogel formation of polymer solutions flowing through porous media, *Soft Matter* **8**, 6445–6453 (2012).
161. J. Vermant and M. J. Solomon, Flow-induced structure in colloidal suspensions, *Journal of Physics: Condensed Matter* **17**, R187–R216 (2005).
162. T. Kume, T. Hattori, and T. Hashimoto, Time evolution of shear-induced structures in semidilute polystyrene solutions, *Macromolecules* **30**, 427–434 (1997).
163. B. Belzung, F. Lequeux, J. Vermant, and J. Mewis, Flow-Induced Anisotropy in Mixtures of Associative Polymers and Latex Particles., *Journal of colloid and interface science* **224**, 179–187 (2000).
164. R. Tóth, R. M. Walliser, N. S. Murray, D. K. Bora, A. Braun, G. Fortunato, C. E. Housecroft, and E. C. Constable, A self-assembled, multicomponent water oxidation device, *Chemical Communications* **52**, 2940–2943 (2016).
165. F. Babayekhorasani, D. E. Dunstan, R. Krishnamoorti, and J. C. Conrad, Nanoparticle dispersion in disordered porous media with and without polymer additives, *Soft Matter* **12**, 5676–5683 (2016).
166. A. Karimi, D. Karig, A. Kumar, and A. M. Ardekani, Interplay of physical mechanisms and biofilm processes: review of microfluidic methods, *Lab Chip* **15**, 23–42 (2015).
167. M. Hajnos, J. Lipiec, R. Świeboda, Z. Sokołowska, and B. Witkowska-Walczak, Complete characterization of pore size distribution of tilled and orchard soil using water retention curve, mercury porosimetry, nitrogen adsorption, and water desorption methods, *Geoderma* **135**, 307–314 (2006).
168. M. Hassanpourfard, A. Valiei, T. Thundat, Y. Liu, and A. Kumar, Biofilm streamer

- formation in a microfluidic porous media mimic, 1–5 (2015).
169. Y. Dalsania, A. Doda, and J. Trivedi, Characterization of ultrahigh-molecular-weight oilfield polyacrylamides under different pH environments by use of asymmetrical-flow field-flow fractionation and multiangle-light-scattering detector, *SPE Journal* **23**, 48–65 (2018).
  170. I. Biswas, R. Ghosh, M. Sadrzadeh, and A. Kumar, Nonlinear deformation and localized failure of bacterial streamers in creeping flows, *Scientific Reports* **6**, 1–6 (2016).
  171. S. Das and A. Kumar, Formation and post-formation dynamics of bacterial biofilm streamers as highly viscous liquid jets., *Scientific reports* **4**, 7126 (2014).
  172. K. Drescher, Y. Shen, B. L. Bassler, and H. a Stone, Biofilm streamers cause catastrophic disruption of flow with consequences for environmental and medical systems., *Proceedings of the National Academy of Sciences of the United States of America* **110**, 4345–50 (2013).
  173. R. Rusconi, S. Lecuyer, L. Guglielmini, and H. A. Stone, streamers Laminar flow around corners triggers the formation of biofilm Subject collections Laminar flow around corners triggers the formation of biofilm streamers, *J. R. Soc. Interface* 1293–1299 (1293).doi:10.1098/rsif.2010.0096
  174. K. Watanabe, 265 Rheological Flocculated, *Water* **24**, 265–278 (1987).
  175. J. Swenson, M. V. Smalley, and H. L. M. Hatharasinghe, Mechanism and strength of polymer bridging flocculation, *Physical Review Letters* **81**, 5840–5843 (1998).
  176. C. Clasen, J. P. Plog, W.-M. Kulicke, M. Owens, C. Macosko, L. E. Scriven, M. Verani, and G. H. McKinley, How dilute are dilute solutions in extensional flows?, *Journal of Rheology* **50**, 849–881 (2006).

177. T. M. Squires and S. R. Quake, Microfluidics: Fluid physics at the nanoliter scale, *Reviews of Modern Physics* **77**, 977–1026 (2005).
178. B. Van Der Bruggen, C. Vandecasteele, T. Van Gestel, W. Doyen, and R. Leysen, A review of pressure-driven membrane processes in wastewater treatment and drinking water production, *Environmental Progress* **22**, 46–56 (2003).
179. S. Khemakhem and R. Ben Amar, Treatment of Industrial Effluents by MF and UF Ceramic Membranes: Comparative Study using Commercial and Elaborated Tunisian Clay Membranes, *Journal of Membrane Science & Technology* **01**, 1–6 (2011).
180. D. Dolar and K. Košutić, Removal of pharmaceuticals by ultrafiltration (UF), nanofiltration (NF), and reverse osmosis (RO), *Comprehensive Analytical Chemistry* **62**, 319–344 (2013).
181. G. Daufin, J. P. Escudier, H. Carrère, S. Bérot, L. Fillaudeau, and M. Decloux, Recent and emerging applications of membrane processes in the food and dairy industry, *Food and Bioproducts Processing: Transactions of the Institution of Chemical Engineers, Part C* **79**, 89–102 (2001).
182. G. K. Pearce, UF/MF pre-treatment to RO in seawater and wastewater reuse applications: a comparison of energy costs, *Desalination* **222**, 66–73 (2008).
183. W. Gao, H. Liang, J. Ma, M. Han, Z. lin Chen, Z. shuang Han, and G. bai Li, Membrane fouling control in ultrafiltration technology for drinking water production: A review, *Desalination* **272**, 1–8 (2011).
184. B. Schlichter, V. Mavrov, and H. Chmiel, Study of a hybrid process combining ozonation and microfiltration / ultrafiltration for drinking water production from surface water, *Process Technology* **168**, 307–317 (2004).

185. N. Debnath and M. Sadrzadeh, Microfluidic Mimic for Colloid Membrane Filtration: A Review, *Journal of the Indian Institute of Science* **98**, 137–157 (2018).
186. B. Sadri, D. Pernitsky, and M. Sadrzadeh, Aggregation and deposition of colloidal particles: Effect of surface properties of collector beads, *Colloids and Surfaces A: Physicochemical and Engineering Aspects* **530**, 46–52 (2017).
187. M. A. Al Mamun, S. Bhattacharjee, D. Pernitsky, and M. Sadrzadeh, Colloidal fouling of nanofiltration membranes: Development of a standard operating procedure, *Membranes* **7** (2017).
188. K. J. Kim, V. Chen, and A. G. Fane, Ultrafiltration of colloidal silver particles: Flux, rejection, and fouling, (1993).
189. M. Taniguchi, J. E. Kilduff, and G. Belfort, Modes of natural organic matter fouling during ultrafiltration, *Environmental Science and Technology* **37**, 1676–1683 (2003).
190. K. Katsoufidou, S. G. Yiantsios, and A. J. Karabelas, A study of ultrafiltration membrane fouling by humic acids and flux recovery by backwashing: Experiments and modeling, *Journal of Membrane Science* **266**, 40–50 (2005).
191. H. Yamamura, K. Kimura, and Y. Watanabe, Mechanism involved in the evolution of physically irreversible fouling in microfiltration and ultrafiltration membranes used for drinking water treatment, *Environmental Science and Technology* **41**, 6789–6794 (2007).
192. E. Iritani and N. Katagiri, Developments of blocking filtration model in membrane filtration, *KONA Powder and Particle Journal* **2016**, 179–202 (2016).
193. S. Saha and C. Das, Analysis of Fouling Characteristics and Flux Decline during Humic Acids Batch Ultrafiltration, *Journal of Chemical Engineering & Process Technology* **06** (2015).

194. E. Dressaire and A. Sauret, Clogging of microfluidic systems, *Soft Matter* **13**, 37–48 (2017).
195. J. de Jong, R. G. H. Lammertink, and M. Wessling, Membranes and microfluidics: a review, *Lab on a Chip* **6**, 1125 (2006).
196. M. Hassanpourfard, Z. Nikakhtari, R. Ghosh, S. Das, T. Thundat, Y. Liu, and A. Kumar, Bacterial floc mediated rapid streamer formation in creeping flows, *Scientific Reports* **5**, 1–17 (2015).
197. N. Debnath, M. Hassanpourfard, R. Ghosh, J. Trivedi, T. Thundat, M. Sadrzadeh, and A. Kumar, Abiotic streamers in a microfluidic system, *Soft Matter* **13**, 8698–8705 (2017).
198. J. C. Chen, Q. Li, and M. Elimelech, In situ monitoring techniques for concentration polarization and fouling phenomena in membrane filtration, *Advances in Colloid and Interface Science* **107**, 83–108 (2004).
199. A Karimi, D. Karig, a Kumar, and a M. Ardekani, Interplay of physical mechanisms and biofilm processes: review of microfluidic methods., *Lab on a chip* **15**, 23–42 (2015).
200. I. Biswas, M. Sadrzadeh, and A. Kumar, Impact of bacterial streamers on biofouling of microfluidic filtration systems, *Biomicrofluidics* **12**, 044116 (2018).
201. R. W. Field, D. Wu, J. a. Howell, and B. B. Gupta, Critical flux concept for microfiltration fouling, *Journal of Membrane Science* **100**, 259–272 (1995).
202. J. N. Ryan and P. M. Gschwend, Effects of ionic strength and flow rate on colloid release: Relating kinetics to intersurface potential energy, (1994).
203. C. Picioreanu, M. C. M. Van Loosdrecht, and J. J. Heijnen, Picioreanu 2000 Two-Dimensional Model of Biofilm Detachment Caused by Internal Stress from Liquid Flow, *Biotechnology and Bioengineering* **72**, 205–218 (2001).

204. M. Zator, M. Ferrando, F. López, and C. Güell, Membrane fouling characterization by confocal microscopy during filtration of BSA/dextran mixtures, *Journal of Membrane Science* **301**, 57–66 (2007).
205. N. Debnath, M. Hassanpourfard, R. Ghosh, J. Trivedi, T. Thundat, M. Sadrzadeh, and A. Kumar, Abiotic streamers in a microfluidic system, *Soft Matter* **13**, 8698–8705 (2017).
206. M. Hassanpourfard, R. Ghosh, T. Thundat, and A. Kumar, Dynamics of bacterial streamers induced clogging in microfluidic devices, *Lab on a Chip* **16**, 4091–4096 (2016).
207. J. Lohaus, Y. M. Perez, and M. Wessling, What are the microscopic events of colloidal membrane fouling?, *Journal of Membrane Science* **553**, 90–98 (2018).
208. W. Chen, Y. Su, J. Peng, X. Zhao, Z. Jiang, Y. Dong, Y. Zhang, Y. Liang, and J. Liu, Efficient wastewater treatment by membranes through constructing tunable antifouling membrane surfaces, *Environmental Science and Technology* **45**, 6545–6552 (2011).
209. F. Gao, G. Zhang, Q. Zhang, X. Zhan, and F. Chen, Improved Antifouling Properties of Poly(Ether Sulfone) Membrane by Incorporating the Amphiphilic Comb Copolymer with Mixed Poly(Ethylene Glycol) and Poly(Dimethylsiloxane) Brushes, *Industrial and Engineering Chemistry Research* **54**, 8789–8800 (2015).
210. B. Mi and M. Elimelech, Organic fouling of forward osmosis membranes: Fouling reversibility and cleaning without chemical reagents, *Journal of Membrane Science* **348**, 337–345 (2010).
211. Z. A. Kuznar and M. Elimelech, Direct microscopic observation of particle deposition in porous media: Role of the secondary energy minimum, *Colloids and Surfaces A: Physicochemical and Engineering Aspects* **294**, 156–162 (2007).
212. B. Van Der Bruggen, C. Vandecasteele, T. Van Gestel, W. Doyenb, and R. Leysenb,

- Review of Pressure-Driven Membrane Processes, *Environmental Progress* **22**, 46–56 (2003).
213. I. Biswas, M. Sadrzadeh, and A. Kumar, Impact of bacterial streamers on biofouling of microfluidic filtration systems, *Biomicrofluidics* **12**, 1–11 (2018).
214. J. A. Brant and A. E. Childress, Assessing short-range membrane-colloid interactions using surface energetics, *Journal of Membrane Science* **203**, 257–273 (2002).
215. N. Debnath, M. Hassanpourfard, R. Ghosh, J. Trivedi, T. Thundat, M. Sadrzadeh, and A. Kumar, Abiotic streamers in a microfluidic system, *Soft Matter* **13**, 8698–8705 (2017).
216. N. Debnath, A. Kumar, T. Thundat, and M. Sadrzadeh, Investigating fouling at the pore-scale using a microfluidic membrane mimic filtration system, *Scientific Reports* **9**, 1–10 (2019).
217. J. De Jong, R. G. H. Lammertink, and M. Wessling, Membranes and microfluidics: A review, *Lab on a Chip* **6**, 1125–1139 (2006).
218. J. Lohaus, Y. M. Perez, and M. Wessling, What are the microscopic events of colloidal membrane fouling?
219. C. Sun, N. Zhang, F. Li, G. Ke, L. Song, X. Liu, and S. Liang, Quantitative analysis of membrane fouling mechanisms involved in microfiltration of humic acid-protein mixtures at different solution conditions, *Water (Switzerland)* **10** (2018).
220. Carel J. van Oss, *Interfacial forces in aqueous porous media*, (1989).
221. Y. Ding, Y. Tian, Z. Li, H. Wang, and L. Chen, Microfiltration (MF) membrane fouling potential evaluation of protein with different ion strengths and divalent cations based on extended DLVO theory, *Desalination* **331**, 62–68 (2013).
222. H. Wang and B. Z. Newby, Applicability of the extended Derjaguin–Landau–Verwey–

- Overbeek theory on the adsorption of bovine serum albumin on solid surfaces, *Biointerphases* **9**, 041006 (2014).
223. C. J. van Oss, M. K. Chaudhury, and R. J. Good, Interfacial Lifshitz—van der Waals and Polar Interactions in Macroscopic Systems, *Chemical Reviews* **88**, 927–941 (1988).
224. M. W. Hahn and C. R. O’Melia, Deposition and Reentrainment of Brownian Particles in Porous Media under Unfavorable Chemical Conditions: Some Concepts and Applications, *Environmental Science and Technology* **38**, 210–220 (2004).
225. C. Shen, B. Li, Y. Huang, and Y. Jin, Kinetics of coupled primary- and secondary-minimum deposition of colloids under unfavorable chemical conditions, *Environmental Science and Technology* **41**, 6976–6982 (2007).
226. C. Q. Qiu, J. Han, H. Gao, L.-P. Wang, and Y. Jin, Pore-Scale Numerical and Experimental Investigation of Colloid Retention at the Secondary Energy Minimum, *Vadose Zone Journal* **11**, 0 (2012).
227. B. Ruben, M. Elisa, L. Leandro, M. Victor, G. Gloria, S. Marina, S. K. Mian, R. Pandiyan, and L. Nadhira, Oxygen plasma treatments of polydimethylsiloxane surfaces: Effect of the atomic oxygen on capillary flow in the microchannels, *Micro and Nano Letters* **12**, 754–757 (2017).
228. H. Tavana, C. N. C. Lam, K. Grundke, P. Friedel, D. Y. Kwok, M. L. Hair, and A. W. Neumann, Contact angle measurements with liquids consisting of bulky molecules, *Journal of Colloid and Interface Science* **279**, 493–502 (2004).
229. T. Trantidou, Y. Elani, E. Parsons, and O. Ces, Hydrophilic surface modification of pdms for droplet microfluidics using a simple, quick, and robust method via pva deposition, *Microsystems and Nanoengineering* **3** (2017).

230. Y. S. Yu, M. C. Wang, and X. Huang, Evaporative deposition of polystyrene microparticles on PDMS surface, *Scientific Reports* **7**, 1–9 (2017).
231. M. W. Toepke and D. J. Beebe, PDMS absorption of small molecules and consequences in microfluidic applications, *Lab on a Chip* **6**, 1484–1486 (2006).
232. C.J. van Oss, Acid-base interfacial interactions in aqueous media, *Colloids and Surfaces A: Physicochemical and Engineering Aspects* **162–164**, 829–830 (1989).
233. C. J. Van Oss, *The Properties of Water and their Role in Colloidal and Biological Systems*, (2008).
234. L. Li, J. Zhang, Y. Tian, L. Sun, W. Zuo, H. Li, A. Li, and M. R. Wiesner, A novel approach for fouling mitigation in anaerobic-anoxic-oxic membrane bioreactor (A 2 O-MBR) by integrating worm predation, *Environment International* **127**, 615–624 (2019).
235. S. H. Behrens and M. Borkovec, Influence of the secondary interaction energy minimum on the early stages of colloidal aggregation, *Journal of Colloid and Interface Science* **225**, 460–465 (2000).
236. J. A. Redman, S. L. Walker, and M. Elimelech, Bacterial Adhesion and Transport in Porous Media: Role of the Secondary Energy Minimum, *Environmental Science and Technology* **38**, 1777–1785 (2004).
237. W. P. Johnson and X. Li, Comment on Breakdown of Colloid Filtration Theory: Role of the Secondary Energy Minimum and Surface Charge Heterogeneities, *Langmuir* **21**, 10895–10895 (2005).
238. M. W. Hahn, D. Abadzic, and C. R. O’Melia, Aquasols: On the role of secondary minima, *Environmental Science and Technology* **38**, 5915–5924 (2004).
239. Z. Wang, Y. Jin, C. Shen, T. Li, Y. Huang, and B. Li, Spontaneous detachment of colloids

- from primary energy minima by brownian diffusion, *PLoS ONE* **11**, 1–21 (2016).
240. G. Singh and L. Song, Quantifying the effect of ionic strength on colloidal fouling potential in membrane filtration, *Journal of Colloid and Interface Science* **284**, 630–638 (2005).
241. C. Shen, F. Wang, B. Li, Y. Jin, L. P. Wang, and Y. Huang, Application of DLVO energy map to evaluate interactions between spherical colloids and rough surfaces, *Langmuir* **28**, 14681–14692 (2012).
242. C. Wang, A. D. Bobba, R. Attinti, C. Shen, V. Lazouskaya, L. P. Wang, and Y. Jin, Retention and transport of silica nanoparticles in saturated porous media: Effect of concentration and particle size, *Environmental Science and Technology* **46**, 7151–7158 (2012).
243. Z. Wang, Y. Jin, C. Shen, T. Li, Y. Huang, and B. Li, Spontaneous detachment of colloids from primary energy minima by brownian diffusion, *PLoS ONE* **11**, 1–21 (2016).
244. S. B. Roy and D. A. Dzombak, Colloid release and transport processes in natural and model porous media, *Colloids and Surfaces A: Physicochemical and Engineering Aspects* **107**, 245–262 (1996).
245. P. Bacchin, P. Aimar, and V. Sanchez, Model for colloidal fouling of membranes, *AIChE Journal* **41**, 368–376 (1995).
246. G. P. S. Ibrahim, A. M. Isloor, Inamuddin, A. M. Asiri, A. F. Ismail, R. Kumar, and M. I. Ahamed, Performance intensification of the polysulfone ultrafiltration membrane by blending with copolymer encompassing novel derivative of poly(styrene-co-maleic anhydride) for heavy metal removal from wastewater, *Chemical Engineering Journal* **353**, 425–435 (2018).

247. R. Jamshidi Gohari, E. Halakoo, W. J. Lau, M. A. Kassim, T. Matsuura, and A. F. Ismail, Novel polyethersulfone (PES)/hydrous manganese dioxide (HMO) mixed matrix membranes with improved anti-fouling properties for oily wastewater treatment process, *RSC Advances* **4**, 17587–17596 (2014).
248. L. R. Firmán, C. Pagliero, N. A. Ochoa, and J. Marchese, PVDF/PMMA membranes for lemon juice clarification: fouling analysis, *Desalination and Water Treatment* **55**, 1167–1176 (2015).
249. X. M. Tan and D. Rodrigue, A review on porous polymeric membrane preparation. Part II: Production techniques with polyethylene, polydimethylsiloxane, polypropylene, polyimide, and polytetrafluoroethylene, *Polymers* **11** (2019).
250. M. Gori, M. C. Simonelli, S. M. Giannitelli, L. Businaro, M. Trombetta, and A. Rainer, Investigating nonalcoholic fatty liver disease in a liver-on-a-chip microfluidic device, *PLoS ONE* **11**, 1–15 (2016).
251. J. Jiang, H. Zhao, W. Shu, J. Tian, Y. Huang, Y. Song, R. Wang, E. Li, D. Slamon, D. Hou, X. Du, L. Zhang, Y. Chen, and Q. Wang, An integrated microfluidic device for rapid and high-sensitivity analysis of circulating tumor cells, *Scientific Reports* **7**, 1–11 (2017).
252. A. Aereas Aung, Ivneet Singh Bhullar, Jomkuan Theprungsirikul, Shruti Krishna Davey, Han Liang Lim, Yu-Jui Chiu, Xuanyi Ma, Sukriti Dewan, Yu-Hwa Lo and and S. V. McCulloch, 3D cardiac  $\mu$  tissues within a microfluidic device with real-time contractile stress readout, *Lab Chip* **16**, 153–162 (2016).
253. A. R. Perestrelo, A. C. P. Águas, A. Rainer, and G. Forte, Microfluidic organ/body-on-a-chip devices at the convergence of biology and microengineering, *Sensors (Switzerland)* **15**, 31142–31170 (2015).

254. S. N. Bhatia and D. E. Ingber, Microfluidic organs-on-chips, *Nature Biotechnology* **32**, 760–772 (2014).
255. S. Srigunapalan, C. Lam, A. R. Wheeler, and C. A. Simmons, A microfluidic membrane device to mimic critical components of the vascular microenvironment, *Biomicrofluidics* **5**, 1–9 (2011).